united nations
educational, scientific
and cultural
organization

international atomic
energy agency

the
abdus salam
international centre for theoretical physics

SMR 1302 - 5

WINTER SCHOOL ON LASER SPECTROSCOPY AND APPLICATIONS

19 February - 2 March 2001

MODERN SPECTROSCOPY AND INSTRUMENTATION

Part I

Wolfgang DEMTRÖDER
Univ. Kaiserslautern - Fachbereich Physik
67653 Kaiserslautern - Germany

These are preliminary lecture notes, intended only for distribution to participants.

W. Demtröder:
„Modern Spectroscopy and Instrumentation
Part I: Instruments.

Winter School ICTP
February 2001

This chapter is devoted to a discussion of instruments and techniques which are of fundamental importance for the measurements of wavelengths and line profiles, or for the sensitive detection of radiation. The optimum selection of proper equipment or the application of a new technique is often decisive for the success of an experimental investigation. Since the development of spectroscopic instrumentation has shown great progress in recent years it is most important for any spectroscopist to be informed about the state-of-the-art regarding sensitivity, spectral resolving power, and signal-to-noise ratios attainable with modern equipment.

At first we discuss the basic properties of *spectrographs* and *monochromators*. Although for many experiments in laser spectroscopy these instruments can be replaced by monochromatic tunable lasers (Chaps.5-6) they are still indispensible for the solution of quite a number of problems in spectroscopy.

Probably the most important instruments in laser spectroscopy are *interferometers*, applicable in various modifications to numerous problems. We therefore treat these devices in somewhat more detail. Recently new techniques of measuring laser wavelengths with high accuracy have been developed; they are mainly based on interferometric devices. Because of their relevance in laser spectroscopy they will be discussed in a separate section.

Great progress has also been achieved in the field of low-level signal detection. Apart from new photomultipliers with an extended spectral sensivity range and large quantum efficiencies, new detection instruments have been developed such as image intensifiers, infrared detectors, or optical multichannel analyzers, which could escape from classified military research into the open market. For many spectroscopic applications they prove to be extremely useful.

4.1 Spectrographs and Monochromators

Spectrographs were the first instruments for measuring wavelengths and they still hold their position in spectroscopic laboratories, particularly when equipped with modern accessories such as computerized microdensitometers or optical multichannel analyzers. Spectrographs are optical instruments

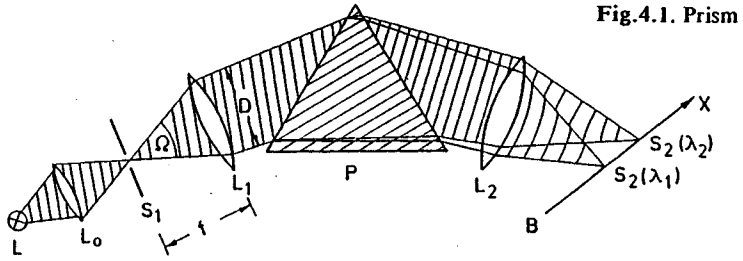

Fig.4.1. Prism spectrograph

which form images $S_2(\lambda)$ of the entrance slit S_1; the images are laterally separated for different wavelengths λ of the incident radiation (Fig.2.10). This lateral dispersion is due to either spectral dispersion in prisms or diffraction on plane or concave reflection gratings.

Figure 4.1 depicts the schematic arrangement of optical components in a *prism spectrograph.* The light source L illuminates the entrance slit S_1 which is placed in the focal plane of the collimator lens L_1. Behind L_1 the parallel light beam passes through the prism P where it is diffracted by an angle $\theta(\lambda)$ depending on the wavelength λ. The camera lens L_2 forms an image $S_2(\lambda)$ of the entrance slit S_1. The position $x(\lambda)$ of this image in the focal plane of L_2 is a function of the wavelength λ. The *linear dispersion* $dx/d\lambda$ of the spectrograph depends on the spectral dispersion $dn/d\lambda$ of the prism material and on the focal length of L_2.

When a reflecting diffraction grating is used to separate the spectral lines $S_2(\lambda)$, the two lenses L_1 and L_2 are commonly replaced by two spherical mirrors M_1 and M_2 which image the entrance slit onto the plane of observation (Fig.4.2). Both systems can use either photographic or photoelectric recording. According to the kind of detection we distinguish between *spectrographs* and *monochromators.*

In spectrographs a photoplate or a CCD diode array is placed in the focal plane of L_2 or M_2. The whole spectral range $\Delta\lambda = \lambda_1(x_1) - \lambda_2(x_2)$ covered by the lateral extension $\Delta x = x_1 - x_2$ of the photoplate can be simul-

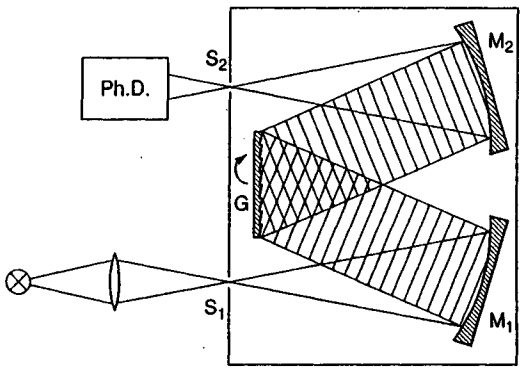

Fig.4.2. Grating monochromator

taneously recorded. If the exposure of the plate remains within the linear part of the photographic density range, the density $D_a(x)$ of the developed photoplate at the position $x(\lambda)$

$$D_a(x) = C(\lambda) \int_0^T I(\lambda) dt \tag{4.1}$$

is proportional to the spectral irradiance $I(\lambda)$, as received in the focal plane B, and integrated over the exposure time T. The sensitivity factor $C(\lambda)$ depends on the wavelength λ, furthermore on the developing procedure and the history of the photoplate (presensitizing). The photoplate can accumulate the incident radiant power over long periods (up to 50h). In astrophysics, for instance, presensitized photographic plates are still the often-used detectors for spectrally dispersed radiation from distant stars or galaxies. Photographic detection can be employed for both pulsed and CW light sources. The spectral range is limited by the spectral sensitivity of available photoplates and covers the region between about 200÷1000 nm. The development of sensitive CCD cameras and optical multichannel analysers which combine the advantages of fast photoelectric recording and signal integration (Sect.4.6) has displaced photoplates for many applications.

Monochromators, on the other hand, use photoelectric recording of a selected small spectral interval. An exit slit S_2, selecting an interval Δx_2 in the focal plane B, lets only the limited range $\Delta\lambda$ through to the photoelectric detector. Different spectral ranges can be detected by shifting S_2 in the x direction. A more convenient solution (which is also easier to construct) turns the prism or grating by a gear-box drive, which allows the different spectral regions to be tuned across the fixed exit slit S_2. Modern devices uses a direct drive of the grating axis by step motors and measure the turning angle by electronic angle decoders. This avoids backlush of the driving gear. Unlike the spectrograph, different spectral regions are detected not simultaneously but successively. The signal received by the detector is proportional to the product of the exit-slit area $h\Delta x_2$ with the spectral intensity $\int I(\lambda)\,d\lambda$, where the integration extends over the spectral range dispersed within the width Δx_2 of S_2.

Whereas the spectrograph allows the simultaneous measurement of a large region with moderate time resolution, photoelectric detection allows high time resolution but permits, for a given spectral resolution, only a small wavelength interval $\Delta\lambda$ to be measured at a time. With integration times below some minutes photoelectric recording shows a higher sensitivity, while for very long detection times of several hours, photoplates may still be more convenient, although nowadays cooled CCD-arrays allow integration times up to one hour.

In spectroscopic literature the name *spectrometer* is often used for both types of instruments.

We now discuss the basic properties of spectrometers, relevant for laser spectroscopy. For a more detailed treatment see for instance [4.1-8].

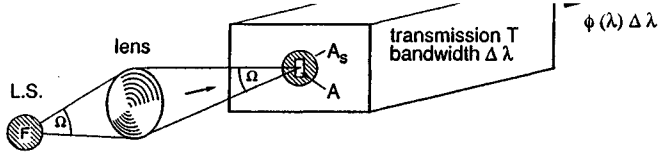

Fig.4.3. Light-gathering power of a spectrometer

4.1.1 Basic Properties

The selection of the optimum type of spectrometer for a particular experiment is guided by some basic characteristics of spectrometers and their relevance to the particular application. The basic properties which are important for all dispersive optical instruments may be listed as follows:

a) Speed of a Spectrometer

When the spectral intensity I_λ^* within the solid angle $d\Omega = 1$ sterad is incident on the entrance slit of area A, a spectrometer with an acceptance angle Ω transmits the radiant flux within the spectral interval $d\lambda$

$$\phi_\lambda d\lambda = I_\lambda^*(A/A_s)T(\lambda)\Omega d\lambda \qquad (4.2)$$

where $A_s \geq A$ is the area of the source image at the entrance slit (Fig.4.3) and $T(\lambda)$ the transmission of the spectrometer.

The product $U = A\Omega$ is often named *étendue*. For the prism spectrograph the maximum solid angle of acceptance, $\Omega = F/f_1^2$, is limited by the effective area $F = hD$ of the prism, which represents the limiting aperture with height h and width D for the light beam (Fig.4.1). For the grating spectrometer the sizes of the grating and mirrors limit the acceptance solid angle Ω.

Example 4.1

For a prism with height h = 6 cm, D = 6 cm, f_1 = 30 cm → D/f = 1:5 and Ω = 0.04 sterad. With an entrance slit of 5×0.1 mm^2 the étendue is $U = 5\cdot10^{-3}\cdot4\cdot10^{-2} = 2\cdot10^{-4}$ $cm^2\cdot$sterad.

In order to utilize the optimum speed, it is advantageous to image the light source onto the entrance slit in such a way that the acceptance angle Ω is fully used (Fig.4.4). Although more radiant power from an extended source can pass the entrance slit by using a converging lens to reduce the source image on the entrance slit, the divergence is increased. The radiation outside the acceptance angle Ω cannot be detected but may increase the background by scattering from lens holders and spectrometer walls.

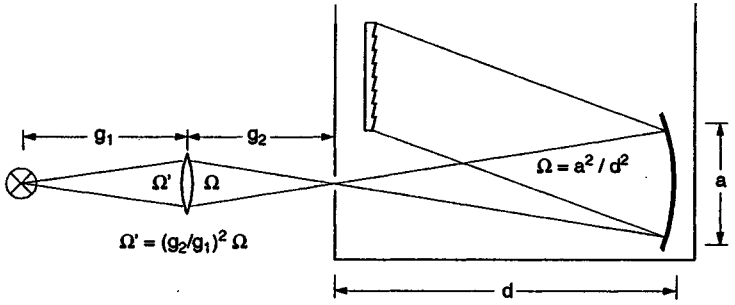

Fig.4.4. Optimized imaging of a light source onto the entrance slit of a spectrometer is achieved when the solid angle Ω' of the incoming light matches the acceptance angle $\Omega = (a/d)^2$ of the spectrometer

Often the wavelength of lasers is measured with a spectrometer. In this case it is not recommendable to direct the laser beam directly onto the entrance slit, because the prism or grating would be not uniformely illuminated. This decreases the spectral resolution. Furthermore, the symmetry of the optical path with respect to the spectrometer axis is not guaranteed with such an arrangement resulting in systematic errors of wavelengths measurements. It is better to illuminate a groundglass plate with the laser and to use the incoherently scattered laser light as a secondary source, which is imaged in the usual way (Fig.4.5).

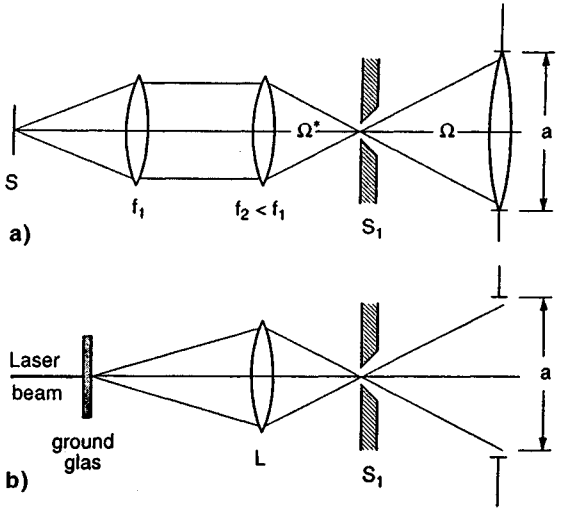

Fig.4.5. (a) Imaging of an extended light source onto the entrance slit of a spectrometer with $\Omega^* = \Omega$. (b) Correct imaging optics for laser wavelength measurements with a spectrometer. The laser light, scattered by the ground glass forms the source which is imaged onto the entrance slit

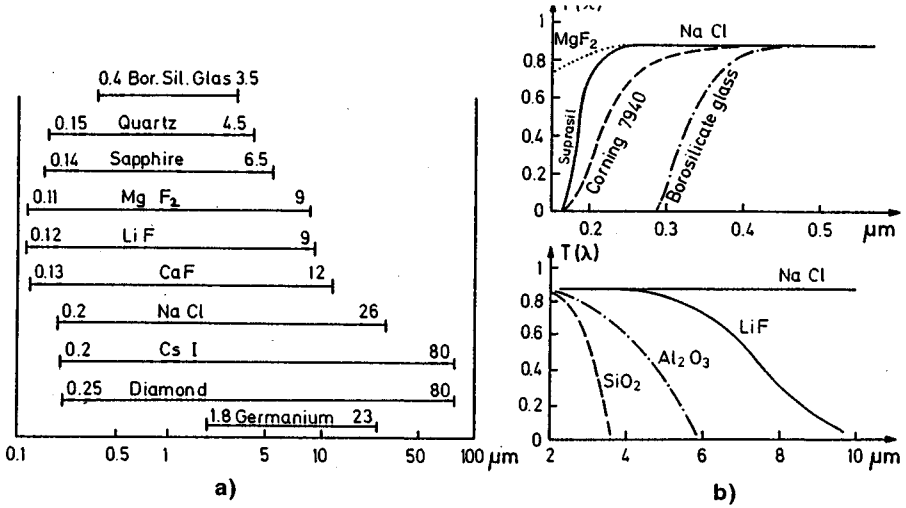

Fig.4.6. (a) Useful spectral ranges of different optical materials and (b) transmittance of different materials with thicknesses 1 cm [4.5b]

b) Spectral Transmission

For prism spectrometers, the spectral transmission depends on the material of the prism and the lenses. Using fused quartz the accessible spectral range spans from about 180 to 3000 nm. Below 180 nm (vacuum-ultraviolet region) the whole spectrograph has to be evacuated, and lithium fluoride or calcium fluoride has to be used for the prism and the lenses, although most VUV spectrometers are equipped with reflection gratings and mirrors.

In the infrared region, several materials (for example, CaF_2 NaCl, and KBr crystals) are transparent up to 30 μm (Fig.4.6). However, because of the high reflectivity of metallic, coated mirrors and gratings in the infrared region, grating spectrometers with mirrors are preferred rather than prism spectrographs.

Many vibrational-rotational transitions of molecules such as H_2O or CO_2 fall within the range $3 \div 10$ μm causing selective absorption of the transmitted radiation. Infrared spectrometers therefore have to be either evacuated or filled with dry nitrogen. Because dispersion and absorption are closely related, prism materials with low absorption losses also show low dispersion, resulting in a limited resolving power (see below).

Since the ruling or holographic production of high-quality gratings has nowadays reached a high technological standard, most spectrometers used today are equipped with diffraction gratings rather than prisms. The spectral transmission of grating spectrometers reaches from the VUV region into the far infrared. The design and the coatings of the optical components and the geometry of the optical arrangement are optimized according to the specified wavelength region.

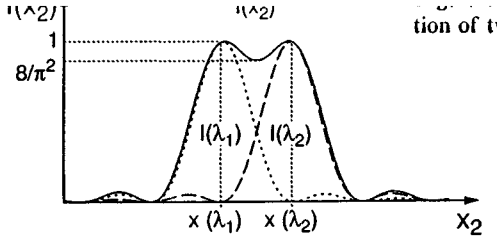

tion of two nearly overlapping lines

c) Spectral Resolving Power

The spectral resolving power of any dispersing instrument is defined by the expression

$$R = |\lambda/\Delta\lambda| = |\nu/\Delta\nu| \,, \tag{4.3}$$

where $\Delta\lambda = \lambda_1 - \lambda_2$ stands for the minimum separation of the central wavelengths λ_1 and λ_2 of two closely spaced lines which are considered to be just resolved. It is possible to recognize that an intensity distribution is composed of two lines with the intensity profiles $I_1(\lambda-\lambda_1)$ and $I_2(\lambda-\lambda_2)$ if the total intensity $I(\lambda) = I_1(\lambda-\lambda_1) + I_2(\lambda-\lambda_2)$ shows a pronounced dip between two maxima (Fig.4.7). The intensity distribution $I(\lambda)$ depends, of course, on the ratio I_1/I_2 and on the profiles of both components. Therefore, the minimum resolvable interval $\Delta\lambda$ will differ for different profiles.

Lord Rayleigh has introduced a criterion of resolution for diffraction limited line profiles, where two lines are considered to be just resolved if the central diffraction maximum of the profile $I_1(\lambda-\lambda_1)$ coincides with the first minimum of $I_2(\lambda-\lambda_2)$ [4.3].

Let us consider the attainable spectral resolving power of a spectrometer. When passing the dispersing element (prism or grating), a parallel beam composed of two monochromatic waves with wavelengths λ and $\lambda+\Delta\lambda$ is split into two partial beams with the angular deviations θ and $\theta+\Delta\theta$ from their initial direction (Fig.4.8). The angular separation is

$$\Delta\theta = (d\theta/d\lambda)\Delta\lambda \,, \tag{4.4}$$

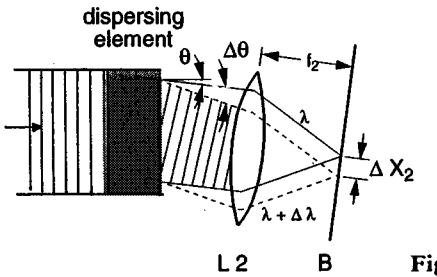

Fig.4.8. Angular dispersion of a parallel beam

with focal length f_2 images the entrance slit S_1 into the plane B (Fig.4.1) the distance Δx_2 between the two images $S_2(\lambda)$ and $S_2(\lambda+\Delta\lambda)$ is, according to Fig.4.8,

$$\Delta x_2 = f_2 \Delta\theta = f_2 \frac{d\theta}{d\lambda}\Delta\lambda = \frac{dx}{d\lambda}\Delta\lambda \,. \tag{4.5}$$

The factor $dx/d\lambda$ is called *linear dispersion* of the instrument. It is generally measured in mm/Å. In order to resolve two lines at λ and $\lambda+\Delta\lambda$, the separation Δx_2 in (4.5) has to be at least the sum $\delta x_2(\lambda) + \delta x_2(\lambda+\Delta\lambda)$ of the widths of the two slit images. Since the width δx_2 is related to the width δx_1 of the entrance slit according to geometrical optics by

$$\delta x_2 = (f_2/f_1)\delta x_1 \,, \tag{4.6}$$

the resolving power $\lambda/\Delta\lambda$ can be increased by decreasing δx_1. Unfortunately there is a theoretical limitation set by diffraction. Because of the fundamental importance of this resolution limit we discuss this point in more detail.

When a parallel light beam passes a limiting aperture with diameter a, a Fraunhofer diffraction pattern is produced in the plane of the focussing lens L_2 (Fig.4.9). The intensity distribution $I(\phi)$ as a function of the angle ϕ with the optical axis of the system is given by the well-known formula [4.3]

$$I(\phi) = I_0 \left[\frac{\sin(a\pi\sin\phi/\lambda)}{(a\pi\sin\phi)/\lambda}\right]^2 \simeq I_0 \left[\frac{\sin(a\pi\phi/\lambda)}{a\pi\phi/\lambda}\right]^2 \,. \tag{4.7}$$

The first two diffraction minima at $\phi = \pm\lambda/a << \pi$ are symmetrical to the central maximum (zeroth diffraction order) at $\phi = 0$. The central maximum contains about 90% of the total intensity.

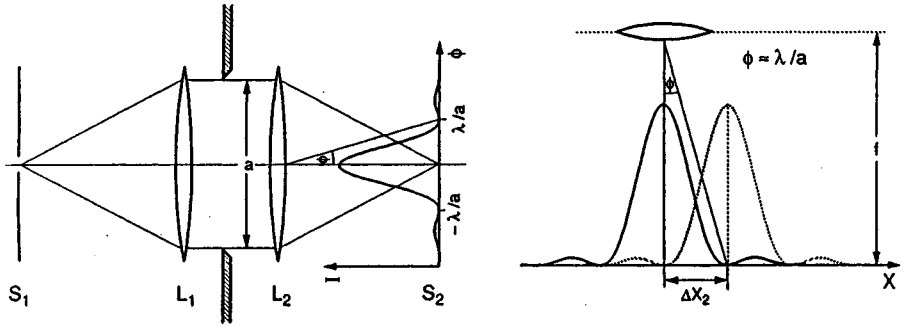

Fig.4.9. (a) Diffraction in a spectrometer by the limiting aperture with diameter a. (b) Limitation of spectral resolution by diffraction

age of width

$$\delta x_s^{diffr} = f_2(\lambda/a) \tag{4.8}$$

defined as the distance between the central diffraction maximum and the first minimum which is approximately equal to the FWHM of the central maximum.

According to the Rayleigh criterion two equally intense spectral lines with wavelengths λ and $\lambda+\Delta\lambda$ are just resolved if the central diffraction maximum of $S_2(\lambda)$ coincides with the first minimum of $S_2(\lambda+\Delta\lambda)$ (see above). From (4.7) one can compute that in this case both lines partly overlap with a dip of $(8/\pi^2)I_{max} \approx 0.8 I_{max}$ between the two maxima. The distance between the centers of the two slit images is from (4.8) (Fig.4.9b)

$$\Delta x_2 = f_2(\lambda/a) \,. \tag{4.9a}$$

With (4.5) one therefore obtains the fundamental limit on the resolving power,

$$|\lambda/\Delta\lambda| \le a(d\theta/d\lambda) \,, \tag{4.10}$$

which clearly depends only on the size a of the limiting aperture and on the angular dispersion of the instrument.

For a finite entrance slit with width b the separation Δx_2 between the central peaks of the two images $I(\lambda-\lambda_1)$ and $I(\lambda-\lambda_2)$ must be

$$\Delta x_2 \ge f_2 \frac{\lambda}{a} + b\frac{f_2}{f_1} \tag{4.9b}$$

in order to meet the Rayleigh criterion (Fig.4.10). With $\Delta x_2 = f_2(d\theta/d\lambda)\Delta\lambda$ the smallest resolvable wavelength intervall $\Delta\lambda$ is then

$$\Delta\lambda \ge \left(\frac{\lambda}{a} + \frac{b}{f_1}\right)\left(\frac{d\theta}{d\lambda}\right)^{-1} . \tag{4.11}$$

Note, that the spectral resolution is limited, *not* by the diffraction due to the entrance slit, but by the diffraction caused by the much larger aperture a, determined by the size of the prism or grating.

Although it does not influence the spectral resolution, the much larger diffraction by the entrance slit imposes a limitation on the transmitted intensity at small slit widths. This can be seen as follows. When illuminated with parallel light, the entrance slit with width b produces a Fraunhofer diffraction pattern analogous to (4.7) with a replaced by b. The central diffraction maximum extends between the angles $\delta\phi = \pm\lambda/b$ (Fig.4.11) and can completely pass the limiting aperture a only if $2\delta\phi$ is smaller than the ac-

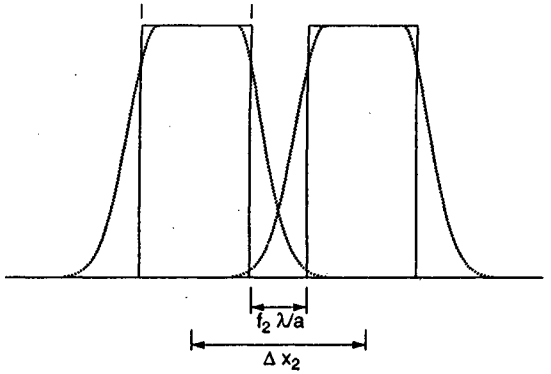

Fig.4.10. Intensity profiles of two monochromatic lines measured with an entrance slit width b and a magnification factor f_2/f_1. *Solid line*: without diffraction; *dashed line*: with diffraction. The minimum resolvable distance between the line centers is $\Delta x_2 = f_2(b/f_1+\lambda/a)$

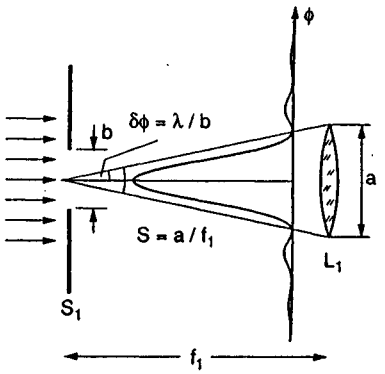

Fig.4.11. Diffraction by the entrance slit

ceptance angle a/f_1 of the spectrometer. This imposes a lower limit to the useful width b_{min} of the entrance slit,

$$b_{min} \geq 2\lambda f_1/a \, . \qquad (4.12)$$

In all practical cases, the incident light is divergent, which demands that the sum of divergence angle and diffraction angle has to be smaller than a/f and the minimum slit width b correspondingly larger.

Figure 4.12a illustrates the intensity distribution I(x) in the plane B for different slit widths b. Figure 4.12b shows the dependence of the width $\Delta x_2(b)$ of the slit image S_2 on the slit width b taking into account the diffraction caused by the aperture a. This demonstrates that the resolution cannot be increased much by decreasing b below b_{min}. The peak intensity $I(b)_{x=0}$ is plotted in Fig.4.12c as a function of the slit width. According to

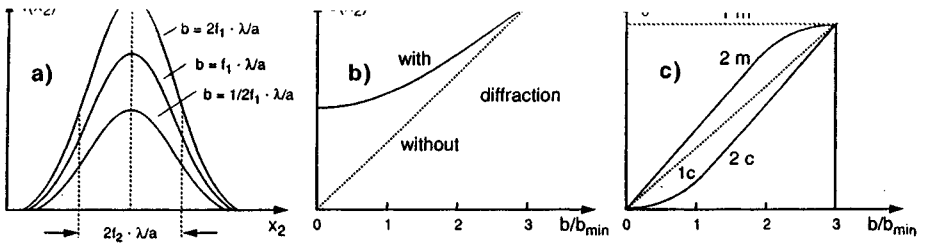

Fig.4.12. (a) Diffraction limited intensity distribution $I(x_2)$ in the plane B for different widths b of the entrance slit. (b) The width $\delta x_2(b)$ of the entrance slit image $S_2(x_2)$ including diffraction by the aperture a. (c) Intensity $I(x_2)$ as a function of entrance slit width for a spectral continuum and for a monochromatic spectral line (m) with diffraction (*solid curves*) and without diffraction (*dashed curves*)

(4.2) the transmitted radiation flux $\phi(\lambda)$ depends on the product $U = A\Omega$ of entrance slit area A and acceptance angle $\Omega = (a/f_1)^2$. The flux in B would therefore depend linearly on the slit width b, if diffraction were not present. This means that for monochromatic radiation the peak intensity [W/m^2] in the plane B should then be constant (curve 1m), while for a spectral continuum it should decrease linearly with decreasing slit width (curve 1c). Because of the diffraction by S_1 the intensity decreases with the slit width b both for monochromatic radiation (2m) and for a spectral continuum (2c). Note the steep decrease for $b < b_{min}$.

Substituting $b = b_{min} = 2f\lambda/a$ into (4.11) yields the practical limit for $\Delta\lambda$ imposed by diffraction by S_1 and by the limiting aperture with width a

$$\Delta\lambda = 3f(\lambda/a)d\lambda/dx \, . \qquad (4.13)$$

Instead of the theoretical limit (4.10) given by the diffraction through the aperture a, a smaller practically attainable resolving power is obtained from (4.13) which takes into account a finite minimum entrance slit width b_{min} imposed by intensity consideration and which yields:

$$\boxed{R = \lambda/\Delta\lambda = (a/3)d\theta/d\lambda \, .} \qquad (4.14)$$

Example 4.2

For a = 10 cm, $\lambda = 5\cdot10^{-5}$ cm, f = 100 cm, $d\lambda/dx$ = 10 Å/mm, with b = 10 μm, $\rightarrow \Delta\lambda$ = 0.15 Å, with b = 5 μm, $\rightarrow\Delta\lambda$ = 0.10 Å. However, from Fig.4.12, one can see that the transmitted intensity with b = 5 μm is only 25% of that with b = 10 μm.

Note: For photographic detection of line spectra, it is actually better to use the lower limit b_{min} for the width of the entrance slit, because the density

of the developed photographic layer depends only on the spectral irradiance [W/m^2] rather than on the radiation power [W]. Increasing the slit width beyond the diffraction limit b_{min}, in fact does not significantly increase the density contrast on the plate, but does decrease the spectral resolution.

Using photoelectric recording, the detected signal depends on the radiation power $\phi_\lambda d\lambda$ transmitted through the spectrometer and therefore increases with increasing slit width. In the case of completely resolved line spectra, this increase is proportional to the slit width b since $\phi_\lambda \propto b$. For continuous spectra it is even proportional to b^2 because the transmitted spectral interval $d\lambda$ also increases proportional to b and therefore $\phi_\lambda d\lambda \propto b^2$. Using diode arrays as detectors the image $\Delta x_2 = (f_2/f_1)b$ should have the same widths as one diode in order to obtain the optimum signal at maximum resolution.

The obvious idea of increasing the product of ΩA without loss of spectral resolution by keeping the width b constant but increasing the height h of the entrance slit is of limited value because imaging defects of the spectrometer cause a curvature of the slit image which again decreases the resolution. Rays from the rim of the entrance slit pass the prism at a small inclination to the principal axis. This causes a larger angle of incidence α_2 which exceeds that of miniumum deviation. These rays are therefore refracted by a larger angle θ, and the image of a straight slit becomes curved towards shorter wavelengths (Fig.4.13). Since the deviation in the plane B is equal to $f_2\theta$, the radius of curvature is of the same order of magnitude as the focal length of the camera lens and increases with increasing wavelength because of the decreasing spectral dispersion. In grating spectrometers curved images of straight slits are caused by astigmatism of the spherical mirrors. The astigmation can be partly compensated by using curved entrance slits [4.7]. Another solution is based on astigmatism-corrected imaging by using an asymmetric optical setup where the first mirror M_1 in Fig.4.2 is placed at a distance $d_1 < f_1$ from the entrance slit and the exit slit at a distance $d_2 > f_2$ from M_2. In this arrangement [4.9] the grating is illuminated with slightly divergent light.

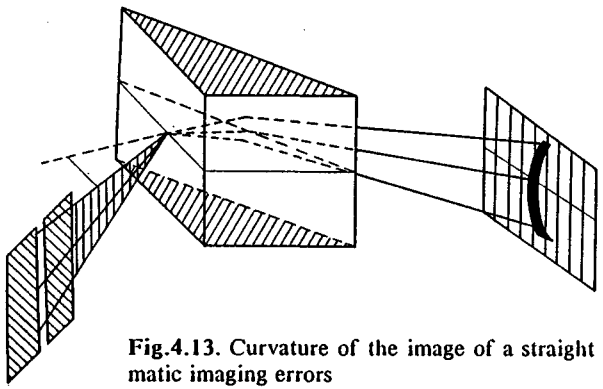

Fig.4.13. Curvature of the image of a straight entrance slit, due to astigmatic imaging errors

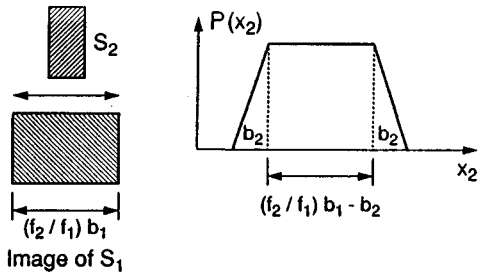

Fig.4.14. Signal profile $P(t) \propto P(x_2)$ at the exit slit of a monochromator with $b >> b_{min}$ and $b_2 < (f_2/f_1)b_1$ for monochromatic incident light with uniform turning of the grating

When the spectrometer is used as a monochromator with an entrance slit width b_1 and an exit slit width b_2, the power P(t) recorded as a function of time while the grating is uniformly turned, has a trapezoidal shape for $b_1 >> b_{min}$ (Fig.4.14a) with a base line $(f_2/f_1)b_1 + b_2$. Optimum resolution at maximum transmitted power is achieved for $b_2 = (f_2/f_1)b_1$. The line profile $P(t) = P(x_2)$ then becomes a triangle.

d) Free Spectral Range

The free spectral range of a spectrometer is the wavelength interval $\delta\lambda$ of the incident radiation for which a one-valued relation exists between λ and the position $x(\lambda)$ of the entrance-slit image. While for prism spectrometers the free spectral range covers the whole region of normal dispersion of the prism material, for grating spectrometers $\delta\lambda$ is determined by the diffraction order m and decreases with increasing m (Sect.4.1.3).

Interferometers, which are generally used in very high orders ($m = 10^4 - 10^8$), have a high spectral resolution but a small free spectral range. For unambiguous wavelength determination they need a preselector, which allows one to measure the wavelength within $\delta\lambda$ of the high-resolution instrument (Sect.4.2.3).

4.1.2 Prism Spectrometer

When passing through a prism, a light ray is refracted by an angle θ which depends on the prism angle ϵ, the angle of incidence α_1, and the refractive index n of the prism material (Fig.4.15). The minimum deviation θ is obtained when the ray passes the prism parallel to the base g (symmetrical arrangement with $\alpha_1 = \alpha_2 = \alpha$). In this case one can derive [4.5]

$$\frac{\sin(\theta + \epsilon)}{2} = n\sin(\epsilon/2)\,. \tag{4.15}$$

From (4.15) the derivation $d\theta/dn = (dn/d\theta)^{-1}$ is

$$\frac{d\theta}{dn} = \frac{2\sin(\epsilon/2)}{\cos[(\theta + \epsilon)/2]} = \frac{2\sin(\epsilon/2)}{\sqrt{1 - n^2\sin^2(\epsilon/2)}}\,. \tag{4.16}$$

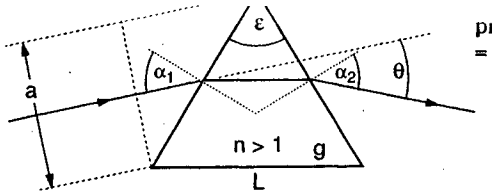

prism at minimum deviation where $\alpha_1 = \alpha_2 = \alpha$ and $\theta = 2\alpha - \epsilon$

The *angular dispersion* $d\theta/d\lambda = (d\theta/dn)(dn/d\lambda)$ is therefore

$$\frac{d\theta}{d\lambda} = \frac{2\sin(\epsilon/2)}{\sqrt{1 - n^2\sin^2(\epsilon/2)}} \frac{dn}{d\lambda} . \tag{4.17}$$

This shows that the angular dispersion increases with the prism angle ϵ *but does not depend on the size of the prism.*

For the deviation of laser beams with small beam diameters small prisms can therefore be used without losing angular dispersion. In a prism spectrometer, however, the size of the prism determines the limiting aperture a and therefore the diffraction; it has to be large in order to achieve a large spectral resolving power (see previous section). For a given angular dispersion, an equilateral prism with $\epsilon = 60°$ uses the smallest quantity of prism material (which might be quite expensive). Because $\sin 30° = 1/2$, (4.17) then reduces to

$$\frac{d\theta}{d\lambda} = \frac{dn/d\lambda}{\sqrt{1 - (n/2)^2}} . \tag{4.18}$$

The resolving power $\lambda/\Delta\lambda$ is according to (4.10)

$$\lambda/\Delta\lambda \leq a(d\theta/d\lambda) .$$

The diameter a of the limiting aperture in a prism spectrometer is (Fig. 4.16)

$$a = d\cos\alpha_1 = \frac{g\cos\alpha}{2\sin(\epsilon/2)} . \tag{4.19}$$

Substituting $d\theta/d\lambda$ from (4.17) gives

$$\lambda/\Delta\lambda = \frac{g\cos\alpha_1}{\sqrt{1 - n^2\sin^2(\epsilon/2)}} \frac{dn}{d\lambda} . \tag{4.20}$$

At minimum deviation, (4.15) gives $n\sin(\epsilon/2) = \sin(\theta+\epsilon)/2 = \sin\alpha_1$ and therefore (4.20) reduces to

$$\lambda/\Delta\lambda = g(dn/d\lambda) . \tag{4.21a}$$

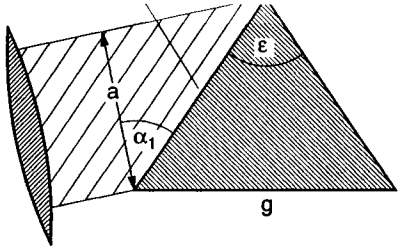

According to (4.21a), the theoretical maximum resolving power depends solely on the base length g and on the spectral dispersion of the prism material. Because of the finite slit width $b \geq b_{min}$ the resolution, reached in practice, is somewhat lower and the corresponding resolving power can be derived from (4.12) to be at most

$$\boxed{R = \frac{\lambda}{\Delta\lambda} \leq \frac{1}{3} g \left(\frac{dn}{d\lambda}\right)} . \tag{4.21b}$$

The spectral dispersion $dn/d\lambda$ is a function of prism material and wavelength λ. Figure 4.17 shows dispersion curves $n(\lambda)$ for some materials commonly used for prisms. Since the refractive index increases rapidly in the vicinity of absorption lines, glass has a larger disperison in the visible and near-ultraviolet regions than quartz which, on the other hand, can be used advantageously in the UV down to 180 nm. In the vacuum-ultraviolet range CaF, MgF, or LiF prisms are sufficiently transparent. Table 4.1 gives a summary of the optical characteristics and useful spectral ranges of some prism materials.

If achromatic lenses (which are expensive in the infrared and ultraviolet region) are not employed, the focal length of the two lenses decreases with the wavelength. This can be partly compensated by inclining the plane

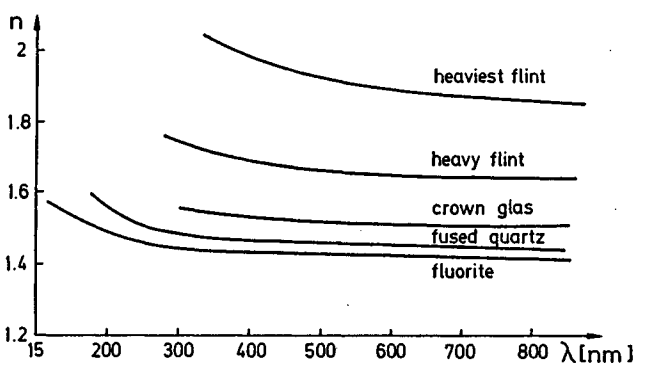

Fig.4.17. Refractive index $n(\lambda)$ for some prism materials

Table 4.1. Refractive index and dispersion of some materials used in prism spectrometers

Material	Useful spectral range [μm]	Refractive index n	Dispersion $-dn/d\lambda$ [nm^{-1}]
Glass (BK7)	0.35 - 3.5	1.516	$4.6 \cdot 10^{-5}$ at 589 nm
		1.53	$1.1 \cdot 10^{-4}$ at 400 nm
Heavy flint	0.4 - 2	1.755	$1.4 \cdot 10^{-4}$ at 589 nm
		1.81	$4.4 \cdot 10^{-4}$ at 400 nm
Fused quartz	0.15 4.5	1.458	$3.4 \cdot 10^{-5}$ at 589 nm
		1.470	$1.1 \cdot 10^{-4}$ at 400 nm
NaCl	0.2 - 26	1.79	$6.3 \cdot 10^{-3}$ at 200 nm
		1.38	$1.7 \cdot 10^{-5}$ at 20 μm
LiF	0.12 - 9	1.44	$6.6 \cdot 10^{-4}$ at 200 nm
		1.09	$8.6 \cdot 10^{-5}$ at 10 μm

B against the principal axis in order to bring it at least approximately into the focal plane of L_2 for a large wavelength range (Fig.4.1).

In Summary: The advantage of a prism spectrometer is the unambiguous assignment of wavelengths, since the position $S_2(\lambda)$ is a monotonic function of λ. Its drawback is the moderate spectral resolution. It is mostly used for survey scans of extended spectral regions.

Example 4.3

a) Suprasil (fused quartz) has a refractive index n = 1.47 at λ = 400 nm and $dn/d\lambda = 1100\ cm^{-1}$. This gives $d\theta/d\lambda = 1.6 \cdot 10^{-4}$ rad/nm.

b) For heavy flint glass at 400 nm n = 1.81 and $dn/d\lambda = 4400\ cm^{-1}$, giving $d\theta/d\lambda = 1.0 \cdot 10^{-3}$ rad/nm. This is about 6 times larger than that for quartz. With a focal length f = 100 cm for the camera lens one achieves a linear dispersion $dx/d\lambda$ = 0.1 mm/Å with a flint prism, but only 0.015 mm/Å with a quartz prism.

4.1.3 Grating Spectrometer

In a grating spectrometer (Fig.4.2) the collimating lens L_1 is replaced by a spherical mirror M_1 with the entrance slit S_1 in the focal plane of M_1. The collimated, parallel light is reflected by M_1 onto a reflection grating consisting of many straight grooves (about 10^5) parallel to the entrance slit. The grooves have been ruled onto an optically smooth glass substrate or have been produced by holographic techniques [4.10-15]. The whole grating surface is coated with a highly reflecting layer (metal or dielectric film). The light reflected from the grating is focussed by the spherical mirror M_2 onto the exit slit S_2 or onto a photographic plate in the focal plane of M_2.

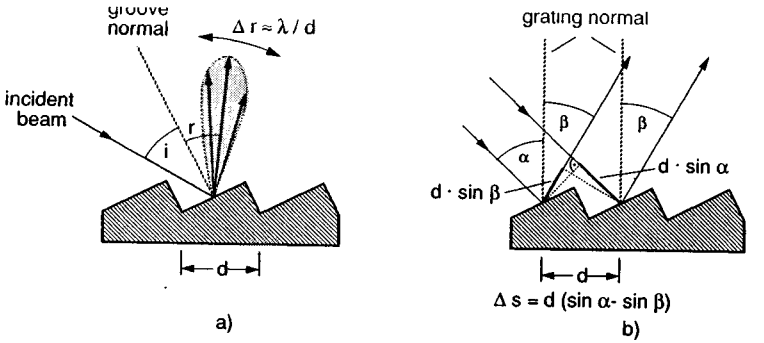

Fig.4.18. (a) Reflection of incident light from a single groove into the diffraction angle λ/d around the specular reflection angle r = i. (b) Illustration of the grating equation (4.22)

The many grooves, which are illuminated coherently, can be regarded as small radiation sources, each of them diffracting the light incident onto this small groove with a width of about one wavelength λ, into a large range of angles r around the direction of geometrical reflection (Fig.4.18a). The total reflected light consists of a coherent superposition of these many partial contributions. Only in those directions where all partial waves, emitted from the different grooves, are in phase will constructive interference result in a large total intensity, while in all other directions the different contributions cancel by destructive interference.

Figure 4.18b depicts a parallel light beam incident onto two adjacent grooves. At an angle of incidence α to the grating normal (which is normal to the grating surface, but not necessary to the grooves) one obtains constructive interference for those directions β of the reflected light for which

$$\boxed{d(\sin\alpha \pm \sin\beta) = m\lambda\ ,} \qquad (4.22)$$

the plus sign has to be taken if β and α are on the same side of the grating normal; otherwise the minus sign, which is the case shown in Fig.4.18b.

The reflectivity $R(\beta,\theta)$ of a ruled grating depends on the diffraction angle β and on the blaze θ of the grating, which is the angle between the groove normal and the grating normal (Fig.4.19). If the diffraction angle β coincides with the angle r of specular reflection from the groove surfaces, $R(\beta,\theta)$ reaches its optimum value R_0, which depends on the reflectivity of the groove coating. From Fig.4.19 one infers $i = \alpha - \theta$ and $r = \theta + \beta$ which yields for specular reflection i = r the condition for the optimum blaze angle θ

$$\theta = (\alpha - \beta)/2\ . \qquad (4.23)$$

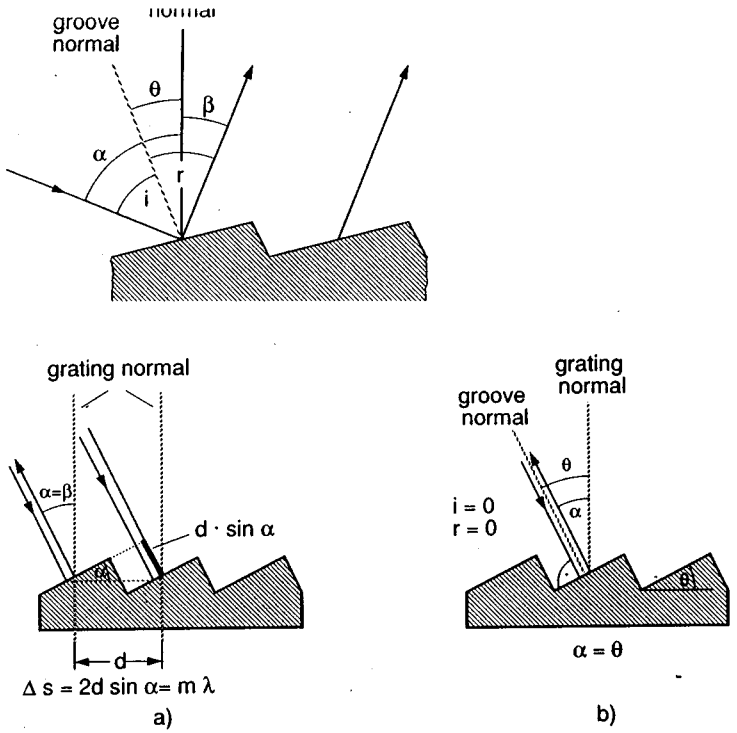

Fig.4.20. (a) Littrow mount of a grating with $\beta = \alpha$. (b) Illustration of blaze angle for a Littrow grating

Because of the diffraction of each partial wave into a large angular range the reflectivity $R(\beta)$ will not have a sharp maximum at $\beta = \alpha - 2\theta$ but will rather show a broad distribution around this optimum angle. The angle of incidence α is determined by the particular construction of the spectrometer and the angle β for which constructive interference occurs depends on the wavelength λ. Therefore the blaze angle θ has to be specified for the desired spectral range and the spectrometer type.

In laser-spectroscopic applications the case $\alpha = \beta$ often occurs, which means that the light is reflected back into the direction of the incident light. For such an arrangement, called a *Littrow-grating mount* (shown in Fig. 4.20), the grating equation (4.22) for constructive interference reduces to

$$2d\sin\alpha = m\lambda \,. \tag{4.22a}$$

Maximum reflectivity of the Littrow grating is achieved for $i = r = 0 \rightarrow \theta = \alpha$ (Fig.4.20b). The Littrow grating acts as a wavelength-selective reflector because light is only reflected if the incident wavelength satisfies the condition (4.22a).

when a monochromatic plane wave is incident onto an arbitrary grating.

The path difference between partial waves reflected by adjacent grooves is $\Delta s = d(\sin\alpha \pm \sin\beta)$ and the corresponding phase difference is

$$\phi = \frac{2\pi}{\lambda}\Delta s = \frac{2\pi}{\lambda} d(\sin\alpha \pm \sin\beta) \,. \tag{4.24}$$

The superposition of the amplitudes reflected from all N grooves in the direction β gives the total reflected amplitude

$$A_R = \sqrt{R} \sum_{m=0}^{N-1} A_g e^{im\phi} = \sqrt{R}\, A_g \frac{1 - e^{iN\phi}}{1 - e^{-i\phi}} \,, \tag{4.25}$$

where $R(\beta)$ is the reflectivity of the grating, which depends on the reflection angle β, and A_g is the amplitude of the partial wave incident onto each groove. Because the intensity of the reflected wave is related to its amplitude by $I_R = \epsilon_0 c A_R A_R^*$, see (2.30c), we find from (4.25)

$$I_R = R I_0 \frac{\sin^2(N\phi/2)}{\sin^2(\phi/2)} \quad \text{with} \quad I_0 = c\epsilon_0 A_g A_g^* \,. \tag{4.26}$$

This intensity distribution is plotted in Fig.4.21 for two different values of the total groove number N. The principal maxima occur for $\phi = 2m\pi$, which is, according to (4.24), equivalent to the grating equation (4.22) and means that at a fixed angle α the path difference between partial beams from adjacent grooves is for certain angles β_m an integer multiple of the wavelength, the integer m being called the *order of the interference*. The function (4.26) has (N-1) minima with $I_R = 0$ between to successive principal maxima. These minima occur at values of ϕ for which $N\phi/2 = \ell\pi$, $\ell = 1, 2..., N-1$, and mean that for each groove of the grating another one can be found which emits light into the direction β with a phase shift π, such that all pairs of partial waves just cancel.

The line profile $I(\beta)$ of the principal maximum of order m around the diffraction angle β_m can be derived from (4.26) by substituting $\beta = \beta_m + \epsilon$. Because for large N, $I(\beta)$ is very sharply centered around β_m, we can assume $\epsilon << \beta_m$. With the relation

$$\sin(\beta_m + \epsilon) = \sin\beta_m \cos\epsilon + \cos\beta_m \sin\epsilon \sim \sin\beta_m + \epsilon\cos\beta_m \,,$$

we obtain from (4.24) because of $(2\pi d/\lambda)(\sin\alpha + \sin\beta_m) = 2m\pi$

$$\phi(\beta) = 2m\pi + 2\pi(d/\lambda)\epsilon\cos\beta_m = 2m\pi + \delta_1 \quad \text{with} \quad \delta_1 << 1 \tag{4.27}$$

and (4.26) can be written as

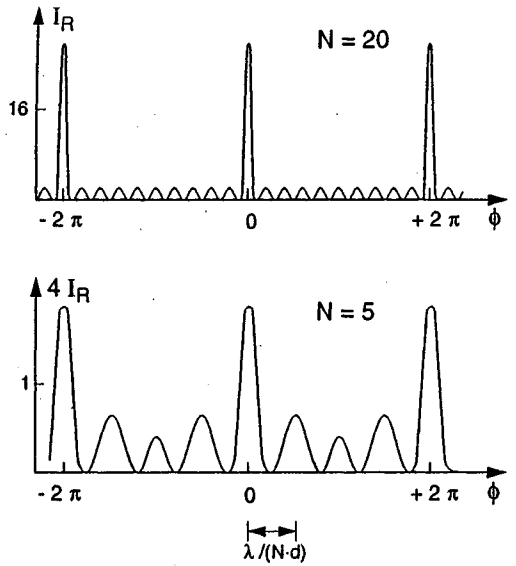

Fig.4.21. Intensity distribution $I(\beta)$ for two different numbers N of illuminated grooves. Note the different scale of the ordinate!

$$I_R = RI_0 \frac{\sin^2(N\delta_1/2)}{\sin^2(\delta_1/2)} \simeq RI_0N^2 \frac{\sin^2(N\delta_1/2)}{(N\delta_1/2)^2}, \tag{4.28}$$

with $\delta_1 = 2\pi(d/\lambda)\epsilon\cos\beta_m$.

The first two minima on both sides of the central maximum at β_m are at

$$N\delta_1 = \pm 2\pi \Rightarrow \epsilon_{1,2} = \frac{\pm\lambda}{Nd\cos\beta_m}. \tag{4.29}$$

The central maximum of m^{th} order therefore has a line profile (4.28) with a base halfwidth $\Delta\beta = \lambda/(Nd\cos\beta_m)$. This corresponds to a diffraction pattern produced by an aperture with width $b = Nd\cos\beta_m$, which is just the size of the whole grating projected onto a direction normal to β_m (Fig. 4.18).

Note that according to (4.28) the angular halfwidth $\Delta\beta = 2\epsilon$ of the interference maxima decreases as 1/N while the peak intensity increases $\propto N^2$ with an increasing number N of illuminated grooves. The area under the main maxima is therefore proportional to N which is due to the increasing concentration of light into the directions β_m.

The intensity of the N-2 small side maxima, which are caused by incomplete destructive interference, decreases proportional to 1/N with in-

creasing groove number. In Figure 4.21 illustrates that for N = 5 and N = 20. For gratings used in practical spectroscopy, with groove numbers of about 10^5, the reflected intensity $I_R(\lambda)$ at a given wavelength λ has very sharply defined maxima only in those directions β_m, as defined by (4.22). The small side maxima are completely negligible at such large values of N, provided the distance d between the grooves is exactly constant over the whole grating area.

Differentiating the grating equation (4.22) with respect to λ we obtain at a given angle α the angular dispersion

$$\frac{d\beta}{d\lambda} = \frac{m}{d\cos\beta}. \tag{4.30a}$$

Substituting from (4.22) $(m/d) = (\sin\alpha \pm \sin\beta)/\lambda$, we find

$$\frac{d\beta}{d\lambda} = \frac{\sin\alpha \pm \sin\beta}{\lambda\cos\beta}. \tag{4.30b}$$

This illustrates that the angular dispersion is determined solely by the angles α and β and *not by the number of grooves*! For the Littrow mount with $\alpha = \beta$, we obtain

$$d\beta/d\lambda = 2\tan\alpha/\lambda. \tag{4.30c}$$

The resolving power can be immediately derived from (4.30a) and the base width $\Delta\beta = 2\epsilon = 2\lambda/(Nd\cos\beta)$ of the principal diffraction maximum (4.29) if we apply the Rayleigh criterion (see above) that two lines λ and $\lambda+\Delta\lambda$ are just resolved when the maximum of $I(\lambda)$ falls into the adjacent minimum for $I(\lambda+\Delta\lambda)$. This is equivalent to the condition

$$(d\beta/d\lambda)\Delta\lambda = \lambda/(Nd\cos\beta),$$

or

$$\frac{\lambda}{\Delta\lambda} = \frac{Nd(\sin\alpha \pm \sin\beta)}{\lambda}, \tag{4.31}$$

which reduces with (4.22) to

$$\boxed{R = \frac{\lambda}{\Delta\lambda} = mN.} \tag{4.32}$$

The theoretical spectral resolving power is the product of the diffraction order m with the total number N of illuminated grooves. If the finite slit width b_1 and the diffraction at limiting aperatures are taken into account, the practically achievable resolving power is according to (4.14) about 3 times lower.

Often it is advantageous to use the spectrometer in second order (m=2) which increases the spectral resolution by a factor 2 without losing much intensity, if the blaze angle θ is correctly choosen to satisfy (4.22 and 23) with m = 2.

Example 4.4

A grating with a ruled area of 10×10 cm^2 and 10^3 grooves/mm allows in second order (m=2) a theoretical spectral resolution of $R = 2 \cdot 10^5$. This means that at λ = 500 nm two lines which are separated by $\Delta\lambda = 2.5 \cdot 10^{-3}$ nm = 0.025 Å should be resolvable. The dispersion is for $\alpha = \beta = 30°$ and a focal length f = 1 m: $dx/d\lambda = f d\beta/d\lambda = 0.2$ mm/Å. With a slit width $b_1 = b_2 = 50$ μm a spectral resolution of $\Delta\lambda = 0.25$ Å can be achieved. Lines around $\lambda = 1$ μm in the spectrum would appear in 1st order at the same angles β. They have to be suppressed by filters.

A special design is the so-called *echelle grating*, which has very widely spaced grooves forming right-angled steps (Fig.4.22). The light is incident normal to the small side of the grooves. The path difference between two reflected partial beams incident on two adjacent grooves with an angle of incidence $\alpha = 90° - \theta$ is $\Delta s = 2d\cos\theta$ and the grating equation (4.22) gives for the angle β of the mth diffraction order

$$d(\cos\theta + \sin\beta) = m\lambda \,, \qquad (4.33)$$

where β is close to $\alpha = 90° - \theta$.

With $d >> \lambda$ the grating is used in a very high order ($m \simeq 10 \div 100$) and the resolving power is very high according to (4.32). Because of the larger distance d between the grooves, the relative ruling accuracy is higher and large gratings (up to 30 cm) can be ruled. The disadvantage of the echelle is the small free spectral range $\delta\lambda = \lambda/m$ between successive diffraction orders.

Example 4.5

N = $3 \cdot 10^4$, d = 10 μm, $\theta = 30°$, λ = 500 nm, m = 34. The spectral resolving power is R = 10^6, but the free spectral range is only $\delta\lambda$ = 15 nm. This means that the wavelengths λ and $\lambda+\delta\lambda$ overlap in the same direction β.

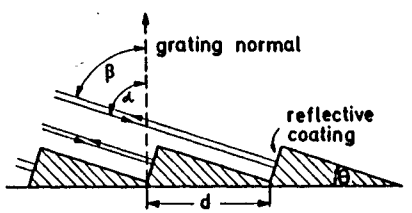

Fig.4.22. Echelle grating

Minute deviations of the distance d between adjacent grooves, caused by inaccuracies during the ruling process, may result in constructive interference from parts of the grating for "wrong" wavelengths. Such unwanted maxima, which occur for a given angle of incidence α into "wrong" directions β, are called *grating ghosts*. Although the intensity of these ghosts is generally very small, intense incident radiation at a wavelength λ_i may cause ghosts with intensities comparable to those of other weak lines in the spectrum. This problem is particularly serious in laser spectroscopy when the intense light at the laser wavelength, which is scattered by cell walls or windows, reaches the entrance slit of the monochromator.

In order to illustrate the problematics of achieving that ruling accuracy which is required to avoid these ghosts, let us assume that the carriage of the ruling engine expands by only 0.1 μm during the ruling of a 10×10 cm^2 grating, e.g., due to temperature drifts. The groove distance d in the second half of the grating differs then from that of the first half by 10^{-5}d. With N = 10^5 grooves the waves from the second half are then completely out of phase with those from the first half. The condition (4.22) is then fulfilled for different wavelengths in both parts of the grating, giving rise to unwanted wavelengths at the wrong positions β. Such ghosts are particularly troublesome in laser Raman spectroscopy (Chap.8) or low-level fluorescence spectroscopy, where very weak lines have to be detected in the presence of extremely strong excitation lines. The ghosts from these excitation lines may overlap with the fluorescence or Raman lines and complicate the assignment of the spectrum.

Although modern ruling techniques with interferometric length control have greatly improved the quality of ruled gratings [4.10-12] the most satisfactory way of producing completely ghost-free gratings is with holography. The production of holographic gratings proceeds as follows. A photosensitive layer on the grating's blank surface is illuminated by two coherent plane waves with the wave vectors $\mathbf{k}_1$ and $\mathbf{k}_2$ ($|\mathbf{k}_1| = |\mathbf{k}_2|$) which form the angles α and β against the surface normal (Fig.4.23). The intensity distribution of the superposition in the plane z = 0 of the photolayer consists of parallel dark and bright fringes imprinting an ideal grating into the layer which becomes visible after developing the photo-emulsion. The grating constant depends on the wavelength $\lambda = 2\pi/|\mathbf{k}|$ and on the angles α and β. Such holographic gratings are essentially free of ghosts. Their reflectivity R, however, is lower than that of ruled gratings and is furthermore strongly

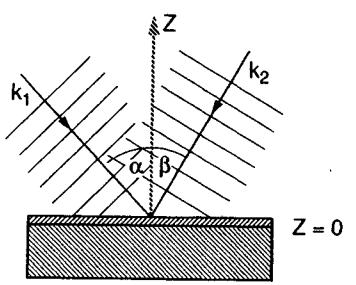

Fig.4.23. Photographic production of a holographic grating

dependent on the polarization of the incident wave. This is due to the fact that holographically produced grooves are no longer plane, but have a sinussodial surface and the "blaze-angle" θ varies across each groove [4.14].

For Littrow gratings, used as wavelength-selective reflectors, it is desirable to have a high reflectivity in a selected order m and low reflections for all other orders. This can be achieved by selecting the width of the grooves and the blaze angle correctly. Due to diffraction by each groove with a width d light can only reach angles β within the intervall $\beta_0 \pm \lambda/d$ (Fig.4.18a).

Example 4.6

With a blaze angle $\theta = \alpha = \beta = 30°$ and a step height $h = \lambda$ the grating can be used in 2nd order , while the 3. order appears at $\beta = \beta_0 + 37°$. With $d = \lambda/\tan\theta = 2\lambda$ the central diffraction lobe extends only to $\beta_0 \pm 30°$ and the intensity in the 3rd order is very small.

Summarizing the considerations above we find that the grating acts as a wavelength-selective mirror, reflecting light of a given wavelength only into definite directions β_m, called the m^{th} diffraction orders, which are defined by (4.22). The intensity profile of a diffraction order corresponds to the diffraction profile of a slit with width $b = Nd\cos\beta_m$ representing the size of the whole grating projection as seen in the direction β_m. *The spectral resolution* $\lambda/\Delta\lambda = mN = Nd(\sin\alpha+\sin\beta)/\lambda$ *is therefore limited by the effective size of the grating measured in units of the wavelength.*

For a more detailed discussion of special designs of grating monochromators such as the concave gratings used in VUV spectroscopy, the reader is referred to the special literature on this subject [4.10-15]. An excellent account of the production and design of ruled gratings can be found in [4.10].

4.2 Interferometers

For the investigation of the various line profiles discussed in Chap.3, interferometers are preferentially used because, with respect to the spectral resolving power, they are superior even to large spectrometers. In laser spectroscopy the different types of interferometers not only serve to measure emission - or absorption - line profiles, but they are also essential devices for narrowing the spectral width of lasers, monitoring the laser linewidth, and controlling and stabilizing the wavelength of single-mode lasers (Chap.5).

In this section we discuss some basic properties of interferometers with the aid of some illustrating examples. The characteristics of the different types of interferometer that are essential for spectroscopic applications are

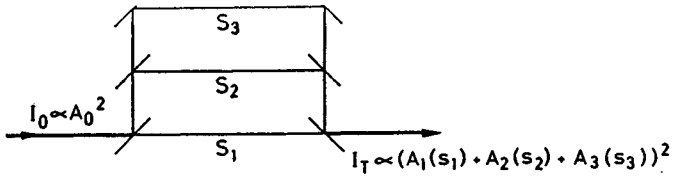

Fig.4.24. Schematic illustration of the basic principle for all interferometers

discussed in more detail. Since laser technology is inconceivable without dielectric coatings for mirrors, interferometers, and filters, an extra section deals with such dielectric multilayers. The extensive literature on interferometers [4.16-19] informs about special designs and applications.

4.2.1 Basic Concepts

The basic principle of all interferometers may be summarized as follows (Fig.4.24). The indicent lightwave with intensity I_0 is divided into two or more partial beams with amplitudes A_k, which pass different optical path lengths $s_k = nx_k$ (n: refractive index) before they are again superimposed at the exit of the interferometer. Since all partial beams come from the same source, they are coherent as long as the maximum path difference does not exceed the coherence length (Sect.2.7). The total amplitude of the transmitted wave, which is the superposition of all partial waves, depends on the amplitudes A_k and on the phases $\phi_k = \phi_0 + 2\pi s_k/\lambda$ of the partial waves. *It is therefore sensitively dependent on the wavelength* λ.

The maximum transmitted intensity is obtained when all partial waves interfere constructively. This gives the condition for the optical path difference $\Delta s_{ik} = s_i - s_k$, namely

$$\Delta s_{ik} = m\lambda \ , \quad m = 1,2,3 \ ..... \tag{4.34}$$

The condition (4.34) for maximum transmission of the interferometer applies not only to a single wavelength λ but to all λ_m for which

$$\lambda_m = \Delta s/m \quad (m = 1, 2, 3, ...) \ .$$

The wavelength interval

$$\delta\lambda = \lambda_m - \lambda_{m+1} = \frac{\Delta s}{m} - \frac{\Delta s}{m+1} = \frac{\Delta s}{m^2 + m} = \frac{2\lambda}{2m+1} \tag{4.35a}$$

where $\lambda = \frac{1}{2}(\lambda_m + \lambda_{m+1})$, is called the *free spectral range* of the interferometer. It is more conveniently expressed in terms of frequency. With $\nu = c/\lambda$, (4.34) yields $\Delta s = mc/\nu_m$ and the free spectral frequency range

$$\boxed{\delta\nu = \nu_{m+1} - \nu_m = c/\Delta s} \qquad (4.35b)$$

becomes independent of the order m.

It is important to realize that from one interferometric measurement alone one can only determine λ modulo $m\cdot\delta\lambda$ because all wavelengths $\lambda = \lambda_0 + m\delta\lambda$ are equivalent with respect to the transmission of the interferometer. One therefore has at first to measure λ within one free spectral range using other techniques, before the absolute wavelength can be obtained with an interferometer.

Examples of devices in which only *two* partial beams interfere, are the Michelson interferometer and the Mach-Zehnder interferometer. *Multiple*-beam interference is used, for instance, in the grating spectrometer, the Fabry-Perot interferometer and in multilayer dielectric coatings of highly reflecting mirrors.

Some interferometers utilize the optical birefringence of specific crystals to produce two partial waves with mutually orthogonal polarization. The phase difference between the two waves is generated by the different refractive index for the two polarizations. An example of such a "polarization interferometer" is the *Lyot filter* [4.20] used in dye lasers to narrow the spectral linewidth (Sect.4.2.9).

4.2.2 Michelson Interferometer

The basic principle of the Michelson interferometer (M.I.) is illustrated in Fig.4.25. The incident plane wave

$$E = A_0 e^{i(\omega t - kx)}$$

is split by the beam splitter S (with reflectivity R and transmittance T) into two waves

$$E_1 = A_1 \exp[i(\omega t - kx + \phi_1)] \quad \text{and} \quad E_2 = A_2 \exp[i(\omega t - ky + \phi_2)] .$$

If the beam splitter has negligible absorption (R+T = 1), the amplitudes A_1 and A_2 are determined by $A_1 = \sqrt{R}A_0$ with $A_0^2 = A_1^2 + A_2^2$.

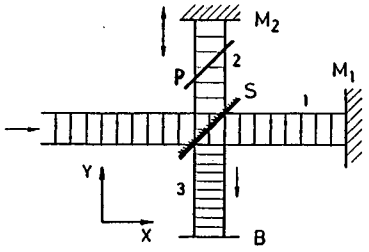

Fig.4.25. Two-beam interference in a Michelson-interferometer

After being reflected at the plane mirrors M_1 and M_2 the two waves are superposed in the plane of observation B. In order to compensate for the dispersion which beam 1 suffers by passing twice through the glass plate of beam splitter S, often an appropriate compensation plate P is placed in one side arm of the interferometer. The amplitudes of the two waves in the plane B are $\sqrt{TR}\,A_0$, because each wave has been transmitted and reflected once at the beam-splitter surface S. The phase difference ϕ between the two waves is

$$\phi = \frac{2\pi}{\lambda} 2(SM_1 - SM_2) + \Delta\phi \ , \qquad (4.36)$$

where $\Delta\phi$ accounts for additional phase shifts which may be caused by reflection. The total complex field amplitude in the plane B is then

$$E = \sqrt{RT}\,A_0 e^{i(\omega t + \phi_0)}(1 + e^{i\phi}) . \qquad (4.37)$$

The detector in B cannot follow the rapid oscillations with frequency ω but measures the time-averaged intensity $\bar{I}$, which is according to (2.30c)

$$\bar{I} = \frac{1}{2} c\epsilon_0 A_0^2 RT(1 + e^{i\phi})(1 + e^{-i\phi}) = c\epsilon_0 A_0^2 RT(1 + \cos\phi)$$

$$= \frac{1}{2} I_0 (1 + \cos\phi) \quad \text{for} \quad R = T = \frac{1}{2} \text{ and } I_0 = \frac{1}{2} c\epsilon_0 A_0^2 . \qquad (4.38)$$

If mirror M_2 (which is mounted on a carriage) moves along a distance Δy, the optical path difference changes by $\Delta s = 2n\Delta y$ (n is the refractive index between S and M_2) and the phase difference ϕ changes by $2\pi\Delta s/\lambda$. Figure 4.26 shows the intensity $I_T(\phi)$ in the plane B as a function of ϕ for a monochromatic incident plane wave. For the maxima at $\phi = 2m\pi$ (m = 0,1,2,...) the transmitted intensity I_T becomes equal to the incident intensity I_0, which means that the transmission of the interferometer is $T_I = 1$ for $\phi = 2m\pi$. In the minima for $\phi = (2m+1)\pi$ the transmitted intensity I_T is zero! The incident plane wave is being reflected back into the source.

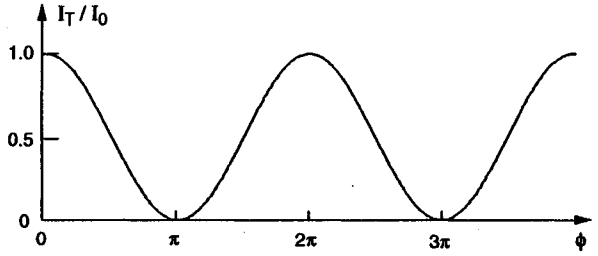

Fig.4.26. Intensity transmitted through the Michelson interferometer in dependence on the phase difference ϕ between the two interfering beams for R = T = 0.5

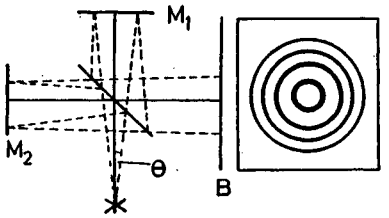

Fig.4.27. Circular fringe pattern produced by the MI with divergent incident light

This illustrates that the M.I. can be regarded either as a wavelength-dependent filter for the transmitted light, or as a wavelength-selective reflector. In the latter function it is often used for mode selection in lasers (Fox-Smith selector, Sect.5.4.3).

For divergent incident light the path difference between the two waves depends on the inclination angle (Fig.4.27). In the plane B an interference pattern of circular fringes, concentric to the symmetry axis of the system, is produced. Moving the mirror M_2 causes the ring diameter to change. The intensity behind a small aperture still follows approximately the function $I(\phi)$ in Fig.4.26. With parallel incident light, but slightly tilted mirrors M_1 or M_2, the interference pattern consists of parallel fringes which move into a direction perpendicular to the fringes when Δs is changed.

The M.I. can be used for absolute wavelength measurements by counting the number N of maxima in B when the mirror M_2 is moved along a known distance Δy. The wavelength λ is then obtained from

$$\lambda = 2n\Delta y/N \, .$$

This technique has been applied to very precise determinations of laser wavelengths (Sect.4.4).

The M.I. may be described in another, equivalent way, which is quite instructive. Assume that the mirror M_2 in Fig.4.25 moves with a constant velocity $v = \Delta y/\Delta t$. A wave with frequency ω and wave vector $\mathbf{k}$ incident perpendicularly on the moving mirror suffers a Doppler shift

$$\Delta\omega = \omega - \omega' = 2\mathbf{k}\cdot\mathbf{v} = (4\pi/\lambda)v \qquad (4.39)$$

on reflection.

Inserting the path difference $\Delta s = \Delta s_0 + 2vt$ and the corresponding phase difference $\phi = (2\pi/\lambda)\Delta s$ into (4.38) gives, with (4.39) and $\Delta s_0 = 0$,

$$\bar{I} = \frac{1}{2}\bar{I}_0(1 + \cos\Delta\omega t) \quad \text{with} \quad \Delta\omega = 2\omega v/c \, . \qquad (4.40)$$

We recognize (4.40) as the time-averaged beat signal, obtained from the superposition of two waves with frequencies ω and $\omega' = \omega - \Delta\omega$, giving the averaged intensity of

$$\bar{I} = I_0(1 + \cos\Delta\omega t)\overline{\cos^2[(\omega' + \omega)t/2]}x = \frac{1}{2}\bar{I}_0(1 + \cos\Delta\omega t) \, .$$

Note that the frequency $\omega = (c/v)\Delta\omega/2$ of the incoming wave can be measured from the beat frequency $\Delta\omega$, provided the velocity v of the moving mirror is known. The M.I. with uniformly moving mirror M_2 can be therefore regarded as a device which transforms the high frequency ω (10^{14} - 10^{15} s^{-1}) into an easily accessible audio range $(v/c)\omega$.

Example 4.6

$v = 3$ cm/s $\rightarrow$ $(v/c) = 10^{-10}$. The frequency $\omega = 3\cdot10^{15}$ Hz ($\lambda = 0.6\mu$m) is transformed to $\Delta\omega = 6\cdot10^5$ Hz $\simeq \Delta\nu \sim 100$ kHz.

The maximum path difference Δs which still gives interference fringes in the plane B is limited by the coherence length of the incident radiation (Sect.2.7). Using spectral lamps the coherence length is limited by the Doppler width of the spectral lines and is typically a few cm. With stabilized single-mode lasers, however, coherence lengths of several kilometers can be achieved. In this case the maximum path difference in the M.I. is, in general, not restricted by the source but by technical limits imposed by laboratory facilities.

The attainable path difference Δs can be considerably increased by an *optical delay line*, placed in one arm of the interferometer (Fig.4.28). It consists of a pair of mirrors, M_3, M_4, which reflect the light back and forth many times. In order to keep diffraction losses small, spherical mirrors are preferable which compensate by collimation the divergence of the beam caused by diffraction. With a stable mounting of the whole interferometer, optical path differences up to 350 m could be realized [4.21], allowing a spectral resolution of $\nu/\Delta\nu \simeq 10^{11}$. This was demonstrated by measuring the linewidth of a HeNe laser oscillating at $\nu = 5\cdot10^{14}$ Hz as a function of discharge current. The accuracy obtained was better than 5 kHz.

For gravitational-wave detection [4.22] a M.I. with side arms of about 1 km length is being built where the optical path difference can be in-

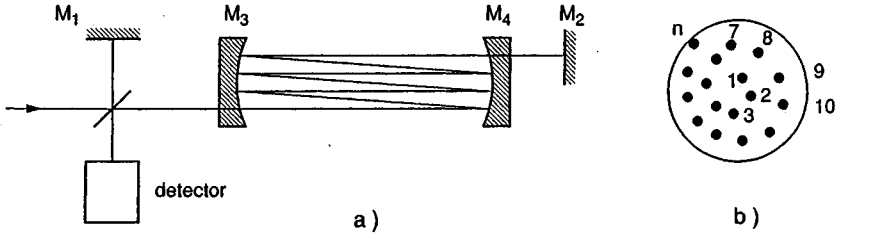

Fig.4.28. Michelson interferometer with optical delay line allowing a large path difference between the two interfering beams (a) schematic arrangement (b) spot sizes of the reflected beams on mirror M_3

creased to $\Delta s > 100$ km by using highly reflective spherical mirrors and an ultrastable argon laser with a coherence length of $\Delta s_c >> \Delta s$ [4.23,24].

When the incoming radiation is composed of several components with frequencies ω_k, the total amplitude in the plane B of the detector is the sum of all interference amplitudes (4.37),

$$E = \sum_k A_k e^{i(\omega_k t + \phi_{0k})}(1 + e^{i\phi_k}) . \tag{4.41}$$

A detector with a time constant large compared with the maximum period $1/(\omega_i - \omega_k)$ does not follow the rapid oscillations of the amplitude at frequencies ω_k or at the difference frequencies $(\omega_i - \omega_k)$ but gives a signal proportional to the sum of the intensities I_k in (4.38). We therefore obtain for the time-dependent total intensity

$$\bar{I}(t) = \sum_k \frac{1}{2}\bar{I}_{k0}(1 + \cos\phi_k) = \sum_k \frac{1}{2}\bar{I}_{k0}(1 + \cos\Delta\omega_k t) , \tag{4.42}$$

where the audio frequencies $\Delta\omega_k = 2\omega_k v/c$ are determined by the frequencies ω_k of the components and by the velocity v of the moving mirror. Measurements of these frequencies $\Delta\omega_k$ allows one to reconstruct the spectral components of the incoming wave with frequencies ω_k (Fourier-transform spectroscopy [4.25]).

For example, when the incoming wave consists of two components with frequencies ω_1 and ω_2, the interference pattern will vary with time according to

$$\bar{I}(t) = \frac{1}{2}\bar{I}_{10}[1 + \cos 2\omega_1(v/c)t] + \frac{1}{2}I_{20}[1 + \cos(2\omega_2(v/c)t]$$

$$= I_0\{1 + \cos[(\omega_1 - \omega_2)vt/c]\cos[(\omega_1 + \omega_2)vt/c]\} ,$$

where we have assumed $I_{10} = I_{20} = I_0$. This is a beat signal, where the amplitude of the interference signal at $(\omega_1+\omega_2)(v/c)$ is modulated at the difference frequency $(\omega_1-\omega_2)v/c$ (Fig.4.29).

The spectral resolution can roughly be estimated as follows: If Δy is the path difference travelled by the moving mirror, the number of interference maxima which are counted by the detector is $N_1 = 2\Delta y/\lambda_1$ for an incident wave with the wavelength λ_1, and $N_2 = 2\Delta y/\lambda_2$ for $\lambda_2 < \lambda_1$. The two wavelengths can be clearly distinguished when $N_2 \geq N_1+1$. This yields with $\lambda_1 = \lambda_2+\Delta\lambda$ and $\Delta\lambda << \lambda$ for the spectral resolving power

$$\frac{\lambda}{\Delta\lambda} = \frac{2\Delta y}{\lambda} = N \quad \text{with} \quad \lambda = (\lambda_1+\lambda_2)/2 \quad \text{and} \quad N = \frac{1}{2}(N_1+N_2) . \tag{4.43a}$$

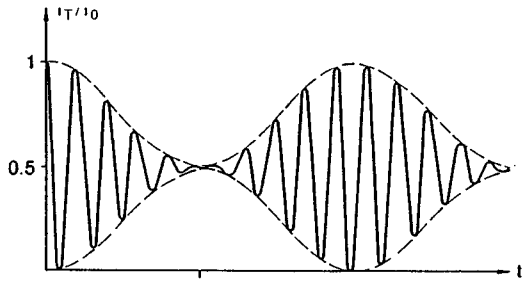

Fig.4.29. Interference signal behind the MI with uniformly moving mirror M_2 when the incident wave consists of two components with frequencies ω_1 and ω_2

The equivalent consideration in the frequency domain is as follows:

In order to determine the two frequencies ω_1 and ω_2, one has to measure at least over one modulation period

$$T = \frac{c}{v}\frac{2\pi}{\omega_1-\omega_2} = \frac{c}{v}\frac{1}{\nu_1-\nu_2} .$$

The frequency difference which can be resolved is then

$$\Delta\nu = \frac{c}{vT} = \frac{c}{\Delta s} = \frac{c}{N\lambda} \Rightarrow \frac{\Delta\nu}{c/\lambda} = \frac{1}{N} \quad \text{or} \quad \frac{\nu}{\Delta\nu} = N . \tag{4.43b}$$

Example 4.7

a) $\Delta y = 5$ cm, $\lambda = 10$ μm $\rightarrow N = 10^4$,

b) $\Delta y = 100$ cm, $\lambda = 0.5$ μm $\rightarrow N = 4\cdot10^6$

where the latter example can be realized only with lasers which have a sufficiently large coherence length (Sect.4.4).

c) $\lambda_1 = 10$ μm, $\lambda_2 = 9.8$ μm $\rightarrow (\nu_2-\nu_1) = 6\cdot10^{11}$ Hz; with $v = 1$ cm/s $\rightarrow T =$ 50 ms.

4.2.3 Mach-Zehnder Interferometer

Analogous to the Michelson interferometer, the Mach-Zehnder interferometer is based on the two-beam interference by amplitude splitting of the incoming wave. The two waves travel along different paths (Fig.4.30a). Inserting a transparent object into one arm of the interferometer alters the optical path difference between the two beams. This results in a change of the interference pattern, which allows a very accurate determination of the refractive index of the sample and its local variation. The Mach-Zehnder interferometer may be regarded therefore as a sensitive refractometer.

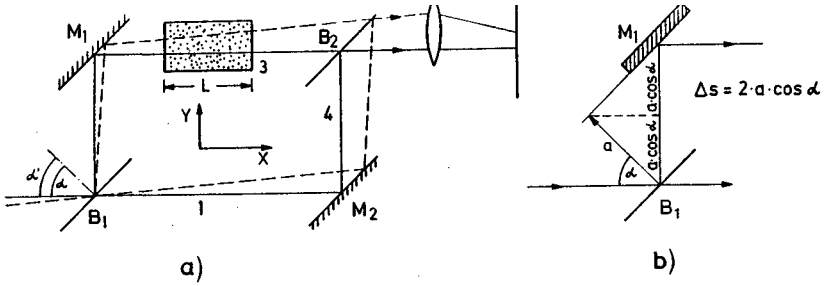

Fig.4.30. Mach-Zehnder interferometer (a) schematic arrangement (b) path difference between the two parallel beams

If the beam splitters B_1, B_2 and the mirrors M_1, M_2 are all strictly parallel, the path difference between the two split beams does not depend on the angle of incidence α because the path difference $\Delta_1 = B_1M_1 = 2a\cos\alpha$ between the beam *1* and *3* is exactly compensated by the sampe path length between M_2 and B_2 (Fig.4.30b). This means that the interfering waves in the symmetric interferometer (without sample) experience the same path difference on the solid path as on the dashed path in Fig.4.30a. Without the sample the total path difference is therefore zero, and it is $\Delta s = (n-1)L$ *with* the sample having the refractive index n in one arm of the interferometer.

Expanding the beam on path *3* gives an extended interference-fringe pattern, which reflects the local variation of the refractive index. Using a laser as a light source with a large coherence length, the path lengths in the two interferometer arms can be made different without losing the contrast of the interference pattern (Fig.4.31). With a beam expander (lenses L_1 and L_2), the laser beam can be expanded up to 10÷20 cm and large objects can be tested. The interference pattern can either be photographed or may be viewed directly with the naked eye or with a television camera [4.26]. Such a laser interferometer has the advantage that the laser-beam diameter can be kept small everywhere in the interferometer, except between the two

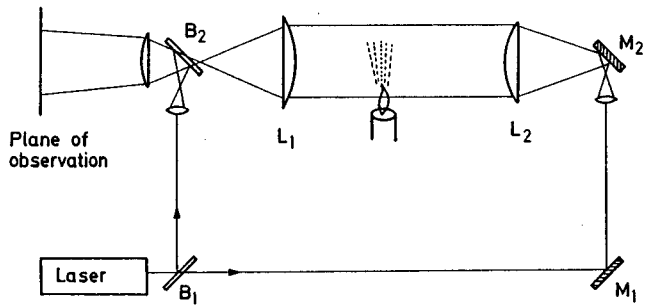

Fig.4.31. Laser interferometer for sensitive measurements of local variations of the index of refraction in extended samples

not deviate from an ideal plane by more than $\lambda/10$ in order to obtain good interferograms, smaller beam diameters are advantageous.

The Mach-Zehnder interferometer has found a wide range of applications. Density variations in laminar or turbulent gas flows can be seen with this technique and the optical quality or mirror substrates of interferometer plates can be tested with high sensitivity [4.26,27].

In order to get quantitative information of the local variation of the optical path through the sample, it is useful to generate a fringe pattern for calibration purposes by slightly tilting the plates B_1, M_1 and B_2, M_2 in Fig. 4.31, which makes the interferometer slightly asymmetric. Assume that B_1 and M_1 are tilted clockwise around the z direction by a small angle β and the pair B_2M_2 is tilted counterclockwise by the same angle β. The optical path between B_1 and M_1 is then $\Delta_1 = 2a\cos(\alpha+\beta)$, whereas $B_2M_2 = \Delta_2 = 2a\cos(\alpha-\beta)$. After being recombined, the two beams therefore have the path difference

$$\Delta = \Delta_2 - \Delta_1 = 2a[\cos(\alpha-\beta) - \cos(\alpha+\beta)] = 4a\sin\alpha\sin\beta\,, \qquad (4.44)$$

which depends on the angle of incidence α. In the plane of observation, an interference pattern of parallel fringes is observed with an angular separation $\Delta\epsilon$ between the fringes m and m+1 given by $\Delta\epsilon = (\sin\alpha_m - \sin\alpha_{m+1}) = \lambda/(4a\beta)$.

A sample in path *3* introduces an additional path difference $\Delta s(\beta) = (n-1)L/\cos\beta$ depending on the local refractive index n and the path length through the sample. The resulting phase difference shifts the interference pattern by an angle $\gamma = \Delta s/(4a\beta)$. Using a lens with a focal length f, which images the interference pattern onto the plane O, the linear shift is $\Delta y = f\Delta s/(4a\beta)$. Figure 4.32 shows for illustration the interferogram of the con-

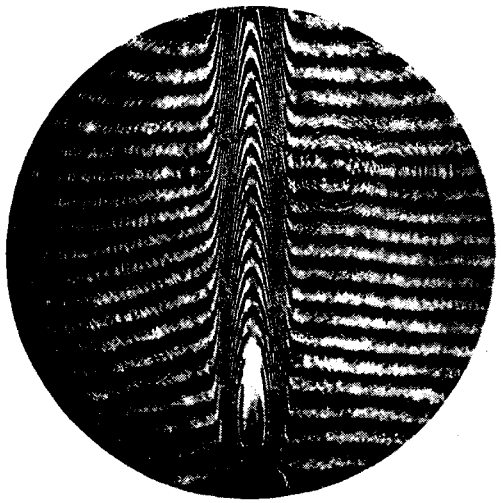

Fig.4.32. Interferogram of the density profile in the convection zone above a candle flame [4.26a]

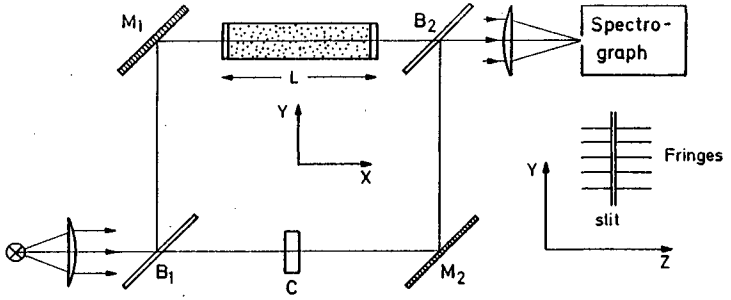

Fig.4.33. Combination of Mach-Zehnder interferometer and spectrograph used for the hook method

vection zone of hot air above a candle flame, placed below one arm of the laser interferometer in Fig.4.31. It can be seen that the optical path through this zone changes by many wavelengths.

The Mach-Zehnder interferometer has been used in spectroscopy to measure the refractive index of atomic vapors in the vicinity of spectral lines (Sect.3.1). The experimental arrangement (Fig.4.33) consists of a combination of a spectrograph and a interferometer, where the plates B_1,M_1 and B_2,M_2 are tilted in such a direction that without the sample the parallel interference fringes with the separation $\Delta y(\lambda) = \lambda f/(4a\beta)$ are perpendicular to the entrance slit. The spectrograph disperses $\Delta y(\lambda)$ in the x direction. Because of the wavelength-dependent refractive index $n(\lambda)$ of the atomic vapor (Sect.3.1.3). The fringe shift follows a disperions curve in the vicinity of the spectral line (Fig.4.34). The dispersed fringes look like hooks around an absorption line, which gave this technique the name *hook method*. To compensate for background shifts caused by the windows of the absorption cell, a compensating plate is inserted into the second arm. For more details of the Hook method, see [4.27,28].

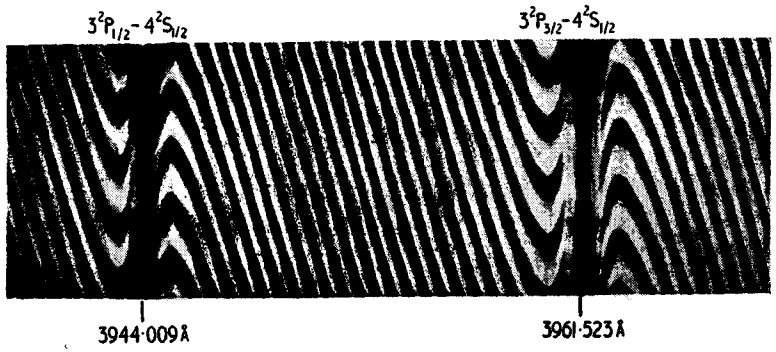

Fig.4.34. Position of fringes as a function of wavelength around the absorption line doublet of aluminum atoms, as observed behind the spectrograph [4.28]

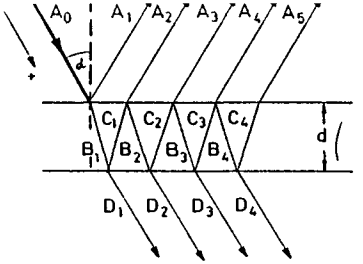

Fig.4.35. Multiple beam interference at two plane parallel partially reflecting surfaces

4.2.4 Multiple-Beam Interference

In a grating spectrometer the interfering partial waves, emitted from the different groves of the grating, have all the same amplitude. In contrast, in multiple-beam interferometers these partial waves are produced by multiple reflection at plane or curved surfaces and their amplitude decreases with increasing number of reflections. The resultant total intensity will therefore differ from (4.26).

Assume that a plane wave $E = A_0 \exp[i(\omega t - kx)]$ is incident at the angle α on a plane transparent plate with two parallel, partially reflecting surfaces (Fig.4.35). At each surface the amplitude A_i is split into a reflected component $A_R = A_i\sqrt{R}$ and a refracted component $A_T = A_i\sqrt{1-R}$, neglecting absorption. The reflectivity $R = I_R/I_i$ depends on the angle of incidence α and on the polarization of the incident wave. Provided the refractive index n is known, R can be calculated from Fresnel's formulas [4.3]. From Fig. 4.35, the following relations are obtained for the amplitudes A_i of waves reflected at the upper surface, B_i of refracted waves, C_i of waves reflected at the lower surface, and D_i of transmitted waves

$$
\begin{aligned}
&|A_1| = \sqrt{R}\,|A_0|\,; && |B_1| = \sqrt{1-R}\,|A_0|\,;\\
&|C_1| = \sqrt{R(1-R)}\,|A_0|\,; && |D_1| = (1-R)\,|A_0|\,;\\
&|A_2| = \sqrt{1-R}\,|C_1| = (1-R)\sqrt{R}\,|A_0|\,; && \\
&|C_2| = R\sqrt{R(1-R)}\,|A_0|\,; && |D_2| = R(1-R)\,|A_0|\,;\\
&|A_3| = \sqrt{1-R}\,|C_2| = R^{3/2}(1-R)\,|A_0| \ldots . &&
\end{aligned}
\tag{4.45}
$$

This scheme can be generalized to the equations

$$|A_{i+1}| = R\,|A_i| \quad i \geq 2 \tag{4.46a}$$

$$|D_{i+1}| = R\,|D_i| \quad i \geq 1\,. \tag{4.46b}$$

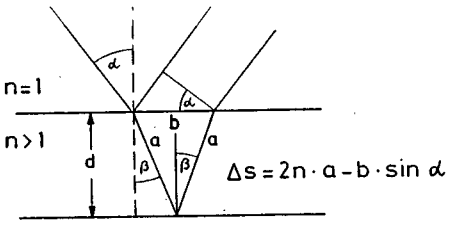

between two beams being reflected from the two surfaces of a plane parallel plate

Two successively reflected partial waves E_i and E_{i+1} have the optical path difference (Fig.4.36)

$$\Delta s = (2nd/\cos\beta) - 2d\tan\beta\sin\alpha \, .$$

Because $\sin\alpha = n\sin\beta$, this can be reduced to

$$\Delta s = 2nd\cos\beta = 2dn\sqrt{1 - \sin^2\beta} \qquad (4.47a)$$

if the refractive index within the plane-parallel plate is $n > 1$ and outside the plate $n = 1$. This path difference causes a corresponding phase difference

$$\phi = 2\pi\Delta s/\lambda + \Delta\phi \, , \qquad (4.47b)$$

where $\Delta\phi$ takes into account possible phase changes caused by the reflections. For instance, the incident wave with amplitude A_1 suffers the phase jump $\Delta\phi = \pi$ while being reflected at the medium with $n > 1$. Including this phase jump, we can write

$$A_1 = \sqrt{R}A_0\exp(i\pi) = -\sqrt{R}A_0 \, .$$

The total amplitude A of the reflected wave is obtained by summation over all partial amplitudes A_i taking into account the different phase shifts,

$$A = \sum_{m=1}^{p} A_m e^{i(m-1)\phi} = -\sqrt{R}A_0 + \sqrt{R}A_0(1-R)e^{i\phi} + \sum_{m=3}^{p} A_m e^{i(m-1)\phi}$$

$$= -\sqrt{R}A_0\left[1 - (1-R)e^{i\phi}\sum_{m=0}^{p-2} R^m e^{im\phi}\right] . \qquad (4.48)$$

For vertical incidence ($\alpha = 0$), or for an infinitely extended plate we have an infinite number of reflections. The geometrical series in (4.48) has for $p \to \infty$ the limit $(1-Re^{i\phi})^{-1}$ and we obtain for the total amplitude

$$A = -\sqrt{R}A_0\frac{1 - e^{i\phi}}{1 - Re^{i\phi}} \, . \qquad (4.49)$$

The intensity $I = 2c\epsilon_0 AA^*$ of the reflected wave is then

$$\boxed{I_R = I_0 R\,\frac{4\sin^2(\phi/2)}{(1-R)^2 + 4R\sin^2(\phi/2)} \, .} \qquad (4.50a)$$

In an analogous way, we find for the total transmitted amplitude

$$D = \sum_{m=1}^{\infty} D_m e^{i(m-1)\phi} = (1-R)A_0\sum_{0}^{\infty} R^m e^{im\phi} \, ,$$

which gives the total transmitted intensity

$$\boxed{I_T = I_0\,\frac{(1-R)^2}{(1-R)^2 + 4R\sin^2(\phi/2)} \, .} \qquad (4.51a)$$

Equations (4.50,51) are called the *Airy formulas*. Since we have neglected absorption, we should have $I_R + I_T = I_0$, as can easily be verified from (4.50, 51).

The abbreviation $F = 4R/(1-R)^2$ is often used, which allows the Airy equations to be written in the form

$$\boxed{I_R = I_0\,\frac{F\sin^2(\phi/2)}{1 + F\sin^2(\phi/2)} \, ,} \qquad (4.50b)$$

$$\boxed{I_T = I_0\,\frac{1}{1 + F\sin^2(\phi/2)} \, .} \qquad (4.51b)$$

Figure 4.37 illustrates (4.51) for different values of the reflectivity R. The maximum transmittance is $T = 1$ for $\phi = 2m\pi$. At these maxima $I_T = I_0$, and the reflected intensity I_R is zero. The frequency range $\delta\nu$ between two maxima is the *free spectral range of the interferometer*. With $\phi = 2\pi\Delta s/\lambda$ and $\lambda = c/\nu$, we obtain from (4.47a)

$$\delta\nu = \frac{c}{\Delta s} = \frac{c}{2d\sqrt{n^2 - \sin^2\alpha}} \, . \qquad (4.52a)$$

For vertical incidence ($\alpha = 0$) the free spectral range becomes

$$|\delta\nu|_{\alpha=0} = \frac{c}{2nd} \, . \qquad (4.52b)$$

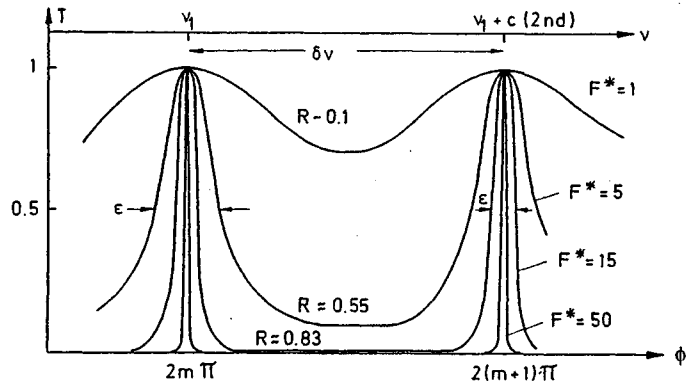

Fig.4.37. Transmittance of an absorption-free multiple beam interferometer as a function of the phase difference ϕ for different values of the finesse F^*

The full halfwidth $\epsilon = |\phi_1 - \phi_2|$ with $I(\phi_1) = I(\phi_2) = I_0/2$ of the transmission maxima in Fig.4.37 expressed in phase differences is calculated from (4.51) as

$$\epsilon = 4\arcsin\left(\frac{1 - R}{2\sqrt{R}}\right), \tag{4.53a}$$

which reduces for $(1 - R) \ll R$ to

$$\epsilon = 2(1 - R)/\sqrt{R} = 4/\sqrt{F} \quad . \tag{4.53b}$$

In frequency units the halfwidth becomes with (4.52b)

$$\Delta\nu = \frac{\epsilon}{2\pi}\delta\nu \simeq \frac{2\delta\nu}{\pi\sqrt{F}} = \frac{c}{2nd}\frac{1 - R}{\pi\sqrt{R}} \, . \tag{4.53c}$$

The ratio $\delta\nu/\Delta\nu$ of free spectral range $\delta\nu$ to the halfwidth $\Delta\nu$ is called the *finesse* F^* of the interferometer. From (4.52b and 53c) we obtain for the finesse

$$\boxed{F^* = \frac{\pi\sqrt{R}}{1 - R} = \frac{\pi}{2}\sqrt{F} \, .} \tag{4.54a}$$

The full halfwidth of the transmission peaks is then

$$\Delta\nu = \delta\nu/F^* \, . \tag{4.54b}$$

The finesse is a measure for the effective number of interfering partial waves in the interferometer. This means that the maximum path difference between interfering waves is $\Delta S_{max} = F^* 2nd$.

Since we have assumed an ideal plane, parallel plate with a perfect surface quality, the finesse (4.54a) is determined only by the reflectivity R of the surfaces. In practice, however, deviations of the surfaces from an ideal plane, and slight inclinations of the two surfaces, cause imperfect superposition of the interfering waves. This results in a decrease and a broadening of the transmission maxima which decreases the total finesse. If, for instance, a reflecting surface deviates by the amount λ/q from an ideal plane, the finesse cannot be larger than q. One can define the total finesse F^* of an interferometer by

$$\frac{1}{F^{*2}} = \sum_i \frac{1}{F_i^{*2}} \, , \tag{4.54c}$$

where the different terms F_i^* give the contributions to the decrease of the finesse caused by the different imperfections of the interferometer.

Example 4.8

A plane, nearly parallel plate may have a diameter D = 5 cm, a thickness d = 1 cm and a wedge angle of 0.2". The two reflecting surfaces have the reflectivity R = 95%. The surfaces are flat to within $\lambda/50$, which means that no point of the surface deviates from an ideal plane by more than $\lambda/50$. The different contributions to the finesse are:

Reflectivity finesse: $F_R^* = \pi\sqrt{R}/(1 - R) \simeq 60$;

Surface finesse: $F_S \simeq 50$;

Wedge finesse: With a wedge angle of 0.2" the optical path between the two reflecting surfaces changes by about 0.1λ ($\lambda = 0.5\mu m$) across the diameter of the plate. This causes for a monochromatic, incident wave imperfect interference and broadens the maxima corresponding to a finesse of about 20. The total finesse is then $F^{*2} = 1/(1/60^2 + 1/50^2 + 1/20^2) \rightarrow F^* \simeq 17.7$.

This illustrates that high-quality optical surfaces are necessary to obtain a high total finesse [4.29]. It makes no sense to increase the reflectivity without a corresponding increase of the surface finesse. In our example the imperfect parallelism was the main cause for the low finesse. Decreasing the wedge angle to 0.1" increases the wedge finesse to 40 and the total finesse to 16.

A much larger finesse can be achieved, using spherical mirrors, because the demand for parallelism is dropped. With sufficiently accurate alignment and high reflectivities, values of $F^* > 50000$ are possible (Sect. 4.2.8).

The spectral resolution $\nu/\Delta\nu$ or $\lambda/\Delta\lambda$ of an interferometer is determined by the free spectral range $\delta\nu$ and by the finesse F^*. Two incident waves with frequencies ν_1 and $\nu_2 = \nu_1 + \Delta\nu$ can still be resolved if their fre-

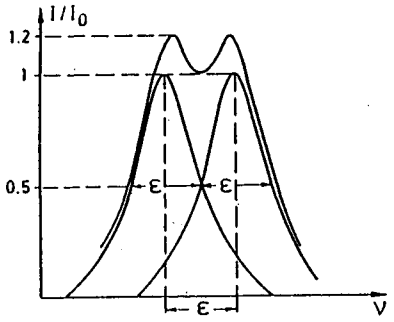

Fig.4.38. Transmitted intensity $I_T(\nu)$ for two closely spaced spectral lines at the limit of spectral resolution

quency separation $\Delta\nu$ is larger than $\delta\nu/F^*$, which means that their peak separation should be larger than their full halfwidth.

Quantitatively this can be seen as follows: Assume the incident radiation consists of two components with the intensity profiles $I_1(\nu-\nu_1)$ and $I_2(\nu-\nu_2)$ and equal peak intensities $I_1(\nu_1) = I_2(\nu_2) = I_0$. For a peak separation $\nu_2-\nu_1 = \delta\nu/F^* = 2\delta\nu/\pi\sqrt{F}$ the total transmitted intensity $I(\nu) = I_1(\nu)+I_2(\nu)$ is obtained from (4.51a) as

$$I(\nu) = I_0\left(\frac{1}{1+F\sin^2(\pi\nu/\delta\nu)} + \frac{1}{1+F\sin^2[\pi(\nu+\delta\nu/F^*)/\delta\nu]}\right), \qquad (4.55)$$

where the phase shift $\phi = 2\pi\Delta s\nu/c = 2\pi\nu/\delta\nu$ has been replaced by the free spectral range $\delta\nu$. The function $I(\nu)$ is plotted in Fig.4.38 around the frequency $\nu = (\nu_1+\nu_2)/2$. For $\nu = \nu_1 = mc/2nd$ the first term in (4.55) becomes 1 and the second term can be derived with $\sin[\pi(\nu_1+\delta\nu/F^*)/\delta\nu] = \sin\pi/F^* \simeq \pi/F^*$ and $F(\pi/F^*)^2 = 4$ to become 0.2. Inserting this into (4.55) yields: $I(\nu=\nu_1) = 1.2\ I_0$; $I(\nu=(\nu_1+\nu_2)/2) \simeq I_0$ and $I(\nu=\nu_2) = 1.2I_0$. This just corresponds to the Rayleigh criterion for the resolution of two spectral lines. The spectral resolving power of the interferometer is therefore

$$\boxed{\nu/\Delta\nu = (\nu/\delta\nu)F^* \rightarrow \Delta\nu = \delta\nu/F^*\ .} \qquad (4.56)$$

This can be also expressed by the optical path differences Δs between two successive partial waves

$$\boxed{\frac{\nu}{\Delta\nu} = \frac{\lambda}{\Delta\lambda} = F^*\frac{\Delta s}{\lambda}\ .} \qquad (4.57)$$

The resolving power of an interferometer is the product of finesse F^* and optical path difference $\Delta s/\lambda$ in units of the wavelength λ.

A comparison with the resolving power $\nu/\Delta\nu = mN = N\Delta s/\lambda$ in a grating spectrometer with N grooves show that the finesse F^* can indeed be regarded as the effective number of interfering partial waves and $F^*\Delta s$ as the maximum path difference between these waves.

Example 4.9

d = 1 cm, n = 1.5, R = 0.98, λ = 500 nm. An interferometer with negligible wedge and high-quality surfaces, where the finesse is mainly determined by the reflectivity, achieves with $F^* = \pi\sqrt{R}/(1-R) = 155$ a resolving power of $\lambda/\Delta\lambda = 10^7$. This means that the instrument's linewidth is about $\Delta\lambda \sim 5\cdot10^{-5}$ nm or, in frequency units $\Delta\nu = 60$ MHz.

Taking into account the absorption A = (1-R-T) of each reflective surface, (4.51) has to be modified to

$$I_T = I_0\frac{T^2}{(A+T)^2}\frac{1}{[1+F\sin^2(\delta/2)]}, \qquad (4.58a)$$

where $T^2 = T_1T_2$ is the product of the transmittance of the two reflecting surfaces. The absorption causes three effects:

(i) The maximum transmittance is decreased by the factor

$$\frac{I_T}{I_0} = \frac{T^2}{(A+T)^2} = \frac{T^2}{(1-R)^2} < 1\ . \qquad (4.58b)$$

Note that already a small absorption of each reflecting surface results in a drastic reduction of the total transmittance. For A = 0.05, R = 0.9 → T = 0.05 and $T^2/(1-R)^2 = 0.25$.

(ii) For a given transmission factor T the reflectivity R = 1-A-T decreases with increasing absorption. The quantity

$$F = \frac{4R}{(1-R)^2} = \frac{4(1-T-A)}{(T+A)^2} \qquad (4.58c)$$

decreases with increasing A. This makes the transmission peaks broader. The physical reasons for this is the decreasing number of interfering partial waves. The *contrast*

$$\frac{I_T^{max}}{I_T^{min}} = 1+F \qquad (4.58d)$$

of the transmitted intensity also decreases.

(iii) The absorption causes a phase shift $\Delta\phi$ at each reflection, which depends on the wavelength λ, the polarization, and the angle of incidence α [4.3]. This effect causes a wavelength-dependent *shift* of the maxima.

4.2.5 Plane Fabry-Perot Interferometer

A practical realization of the multiple beam-interference discussed in this section may use either a solid plane-parallel glass or fused quartz plate with two coated reflecting surfaces (Fabry-Perot etalon, Fig.4.39a) or two separate plates, where one surface of each plate is coated with a reflection layer. The two reflecting surfaces oppose each other and are aligned to be as parallel as achievable (Fabry-Perot Interferometer, FPI, Fig.4.39b). The outer surfaces are coated with antireflection layers in order to avoid reflections from these surfaces which might overlap the interference pattern. Furthermore, they have a slight angle against the inner surfaces (wedge).

Both devices can be used for parallel as well as for divergent incident light. We now discuss them in some more detail where, at first, considering their illumination with *parallel* light.

a) The Plane FPI as a Transmission Filter

In laser spectroscopy etalons are mainly used as wavelength-selective transmission filters within the laser resonator to narrow the laser bandwidth (Sect. 5.4). The wavelength λ_m or frequency ν_m for the transmission maximum of m^{th} order, where the optical path between successive beams is $\Delta s = m\lambda$, can be deduced from (4.47a) and Fig.4.36 to be

$$\lambda_m = \frac{2d}{m}\sqrt{n^2 - \sin^2\alpha} = \frac{2nd}{m}\cos\beta \qquad (4.59a)$$

$$\nu_m = \frac{mc}{2nd\cos\beta} \; . \qquad (4.59b)$$

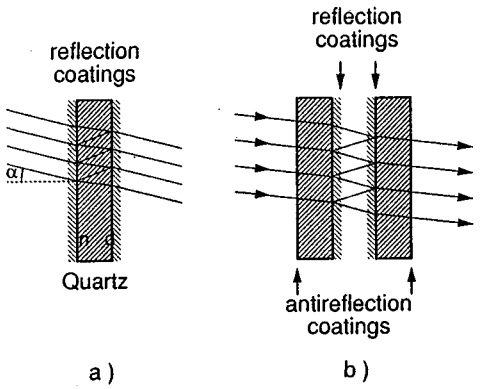

Fig.4.39. Two realizations of a Fabry-Perot interferometer (a) solid etalon (b) air-spaced plane parallel reflecting surfaces

For all wavelengths $\lambda = \lambda_m$ (m = 0,1,2 ...) in the incident light, the phase difference between the transmitted partial waves becomes $\delta = 2m\pi$ and the transmitted intensity is according to (4.58)

$$I_T = \frac{T^2}{(1-R)^2} I_0 = \frac{T^2}{(A+T)^2} I_0 \; , \qquad (4.60)$$

where A = 1-T-R is the absorption of the etalon (substrate absorption plus absorption of one reflecting surface). The reflected waves interfere destructively for $\lambda = \lambda_m$ and the reflected intensity becomes zero.

Note, however, that this is only true for A << 1 and infinitely extended plane waves where the different reflected partial waves completely overlap. If the incident wave is a laser beam with the finite diameter D, the different reflected partial beams do *not* completely overlap because they are laterally shifted by $b = 2d\tan\beta\cos\alpha$ (Fig.4.40). For a rectangular intensity profile of the laser beam the fraction b/D of the reflected partial amplitudes does not overlap and cannot interfere destructively. This means that even for maximum transmission the reflected intensity is not zero but a background reflection remains, which is missing in the transmitted light. For small angles α one obtains for the intensity loss per transit due to reflection [4.30a] for a rectangular beam profile

$$\frac{I_R}{I_0} = \frac{4R}{(1-R)^2}\left(\frac{2\alpha d}{nD}\right)^2 \; . \qquad (4.61a)$$

For a Gaussian beam profile the calculation is more difficult, and the solution can only be obtained numerically. The result for a Gaussian beam with the radius w (Sect.5.3) is [4.30b]

$$\frac{I_R}{I_0} \simeq \frac{8R}{(1-R)^2}\left(\frac{2d\alpha}{nw}\right)^2 \; . \qquad (4.61b)$$

A parallel light beam with the diameter D passing a plane parallel plate with the angle of incidence α therefore suffers, besides eventual absorption losses, reflection losses which increase with α^2 and which are proportional to the ratio $(d/D)^2$ of the etalon thickness d and the beam diameter D (walk-off losses).

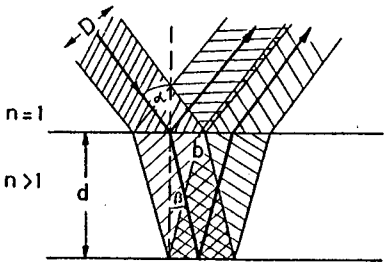

Fig.4.40. Incomplete interference of two reflected beams with finite diameter D, causing a decrease of the maximum transmitted intensity

Example 4.10

d = 1 cm, D = 0.2 cm, n = 1.5, R = 0.3, $\alpha = 1° \hat{=} 0.017$ rad $\rightarrow I_R/I_0 = 0.05$, which means 5% walk-off losses.

The transmission peak λ_m of the etalon can be shifted by tilting the etalon. According to (4.59) the wavelength λ_m *decreases* with increasing angle of incidence α. The walk-off losses limit the tuning range of tilted etalons within a laser resonator. With increasing angle α the losses may become intolerably large.

b) Illumination with Divergent Light

Illuminating the FPI with divergent monochromatic light (e.g., from an extended source or from a laser beam, behind a diverging lens), a continuous range of incident angles α is offered to the FPI, which transmits those directions α_m that obey (4.59a). In the transmitted light we then observe an interference pattern of bright rings (Fig.4.41). Since the reflected intensity $I_R = I_0 - I_T$ is complementary to the transmitted one, a corresponding system of dark rings appears in the reflected light at the same angles of incidence α_m.

When β is the angle of inclination to the interferometer axis inside the FPI, the transmitted intensity is maximum, according to (4.59), for

$$m\lambda = 2nd\cos\beta\,, \tag{4.62a}$$

where n is the refractive index between the reflecting planes. Let us number the rings by the integer p, beginning with p = 0 for the central ring. With $m = m_0 - p$ we can rewrite (4.63) for small angles β_P as

$$(m_0 - p)\lambda = 2nd\cos\beta_P \sim 2nd(1 - \beta_p^2/2) = 2nd\left[1 - \frac{1}{2}\left(\frac{n_0}{n}\alpha_p\right)^2\right] \tag{4.63}$$

where n_0 is the refractive index of air, and Snell's law $\sin\alpha \simeq \alpha = n\beta$ has been used (Fig.4.42).

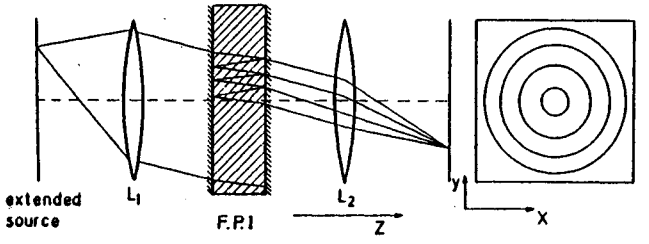

Fig.4.41. The interference ring system of the transmitted intensity may be regarded as wavelength selective imaging of corresponding ring areas of an extended light source

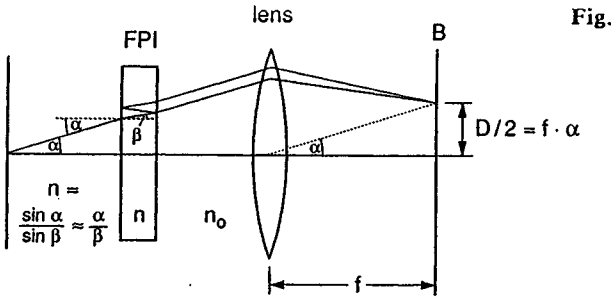

Fig.4.42. Illustration of (4.64)

When the interference pattern is imaged by a lens with the focal length f into the plane of the photoplate, we obtain for the ring diameters $D_p = 2f\alpha_p$ the relations

$$\begin{aligned}(m_0 - p)\lambda &= 2nd[1 - (n_0/n)^2 D_p^2/(8f^2)]\,,\\ (m_0 - p - 1)\lambda &= 2nd[1 - (n_0/n)^2 D_{p+1}^2/(8f^2)]\,.\end{aligned} \tag{4.64}$$

Subtracting the second equation from the first one yields

$$D_{p+1}^2 - D_p^2 = \frac{4nf^2}{n_0^2 d}\lambda\,. \tag{4.65a}$$

For the smallest ring with p = 0 (4.63) becomes

$$m_0\lambda = 2nd(1 - \beta_0^2/2)$$

which can be written as

$$(m_0 + \epsilon)\lambda = 2nd\,. \tag{4.62b}$$

The "excess" $\epsilon < 1$, also called *fractional interference order*, can be obtained from a comparison of (4.62a and b) as

$$\epsilon = nd\beta_0^2/\lambda\,.$$

Inserting ϵ into (4.65) yields the relation

$$D_p^2 = \frac{4nf^2}{n_0^2 d}\lambda\,(p + \epsilon) = \frac{8n^2f^2}{n_0^2(m_0 + \epsilon)}(p + \epsilon)\,. \tag{4.65b}$$

A linear fit of the squares D_p^2 of the measured ring diameters versus the ring number P yields the excess ϵ and therefore from (4.63b) the wavelength λ, provided the refractive index n and the value of d is known from a previous calibration of the interferometer. However, the wavelength is

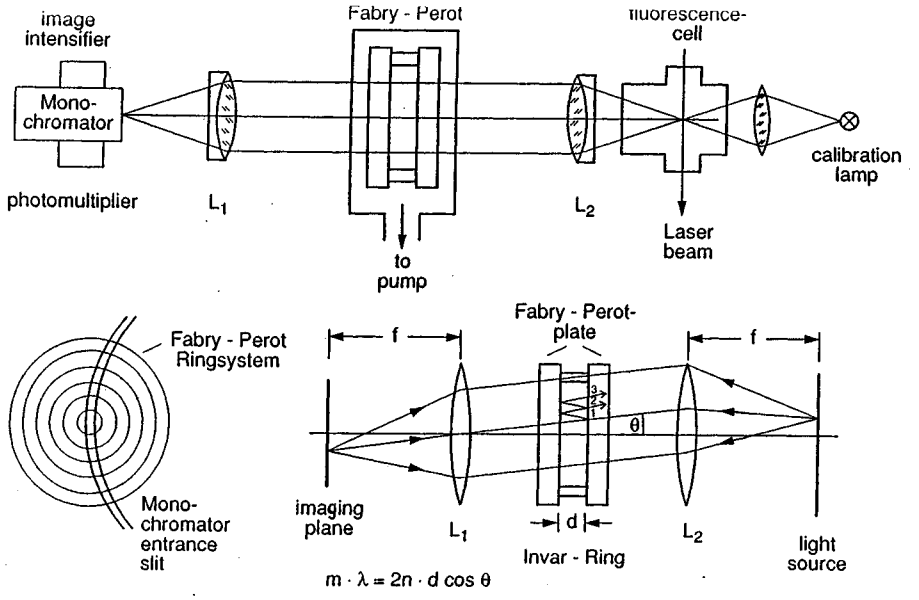

Fig.4.43. Combination of FPI and spectrograph for the unambiguous determination of the integral order m_0

determined by (4.65) only modulo a free spectral range 2nd. This means that all wavelengths λ_m differing by m free spectral ranges produce the same ring systems. For an absolute determination of λ the integer order m_0 has to be known.

The experimental scheme for the determination of λ utilizes a combination of FPI and spectrograph in a so-called *crossed arrangement* (Fig. 4.43) where the ring system of the FPI is imaged onto the entrance slit of a spectrograph. The spectrograph disperses the slit images $S(\lambda)$ with a medium dispersion in the x direction (Sect.4.1) and the FPI provides high dispersion in the y direction. The resolution of the spectrograph must only be sufficiently high to separate the images of two wavelengths differing by one free spectral range of the FPI. Figure 4.44 shows, for illustration, a section of the Na_2 fluorescence spectrum excited by an argon-laser line. The ordinate corresponds to the FPI dispersion and the abscissa to the spectrograph dispersion [4.31].

The angular dispersion of the FPI can be deduced from (4.63)

$$\frac{d\beta}{d\lambda} = \left(\frac{d\lambda}{d\beta}\right)^{-1} = \frac{m}{2nd\sin\beta} = \frac{1}{\lambda_m \sin\beta} \quad \text{with} \quad \lambda_m = 2nd/m \,. \tag{4.66}$$

Equation (4.66) shows that the angular dispersion becomes infinite for $\beta \to 0$.

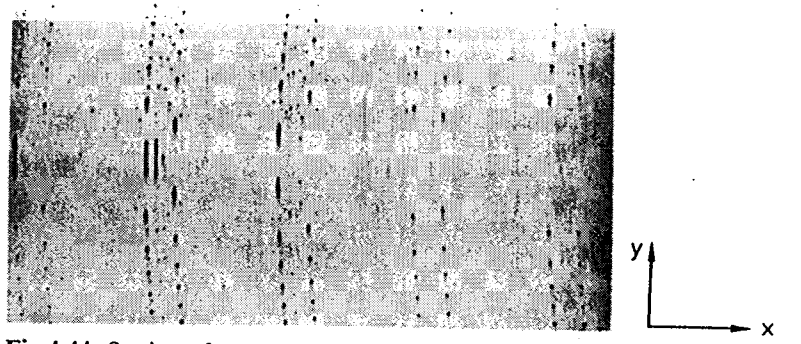

Fig.4.44. Section of the argon laser-excited fluorescence spectrum of Na_2 obtained with the arrangement of crossed FPI and spectrograph, shown in Fig.4.43

The linear dispersion of the ring system on the photoplate is

$$\frac{dd}{d\lambda} = f\frac{d\beta}{d\lambda} = \frac{f}{\lambda_m \sin\beta} \,. \tag{4.67}$$

Example 4.11

f = 50 cm, λ = 0.5 μm. At a distance of 1 mm from the ring center is β = 0.1/50 and we obtain a linear dispersion of $dd/d\lambda$ = 50 mm/Å. This is at least one order of magnitude larger than the disperison of a large spectrograph.

---

c) The Air-Spaced FPI

Different from the solid etalon, which is a plane-parallel plate coated on both sides with reflecting layers, the plane FPI consists of two wedged plates, each having one high-reflection and one antireflection coating (Fig.4.39b). The finesse of the FPI critically depends, apart from the reflectivity R and the optical surface quality, on the parallel alignment of the two reflecting surfaces. The advantage of the FPI, that any desired free spectral range can be realized by choosing the corresponding plate separation d, must be paid for by the inconvenience of careful alignment. Instead of changing the angle of incidence α, wavelength tuning can be achieved for α = 0 by variation of the optical path difference Δs = 2nd either by changing d with piezoelectric tuning of the plate separation or by altering the refractive index by a pressure change in the container enclosing the FPI.

The pressure-tunable FPI is used for high-resolution spectroscopy of line profiles. The transmitted intensity $I_T(p)$ as a function of pressure is given by the convolution

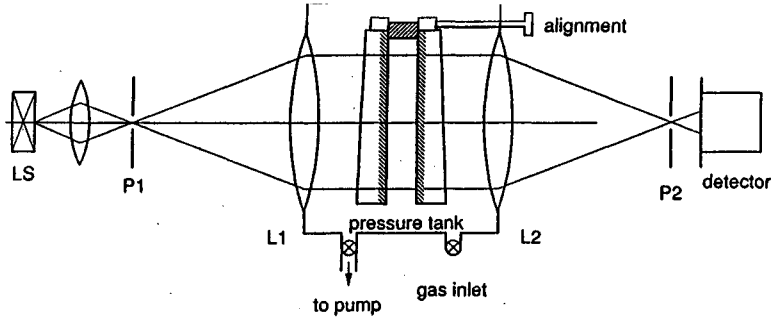

Fig.4.45. Use of a plane FPI for photoelectric recording of the spectrally resolved transmitted intensity $I_T(n \cdot d,\lambda)$ emitted from a point source

$$I_T(\nu) = I_0(\nu)\,T(nd,\lambda)$$

where $T(nd,\lambda) = T(\phi)$ can be obtained from (4.51).

With photoelectric recording (Fig.4.45) the large dispersion at the ring center can be utilized. The light source is imaged onto a small pinhole P1 which serves as a point source in the focal plane of L1. The parallel light beam passes the FPI, and the transmitted intensity is imaged b< L2 onto another pinhole P2 in front of the detector. All light rays around $\beta = 0$, where β is the angle against the interferometer axis (4.59) contribute to the central fringe. If the optical path length nd is tuned, the different transmission orders with $m = m_0, m_0+1, m_0+2$ ... are successively transmitted for a wavelength λ according to $m\lambda = 2nd$. Light sources which come close to a point source, can be realized when a focussed laser beam crosses a sample cell and the laser-induced fluorescence emitted from a small section of the beam length is imaged through the FPI onto the entrance slit of a monochromator, which is tuned to the desired wavelength interval $\Delta\lambda$ around λ_m

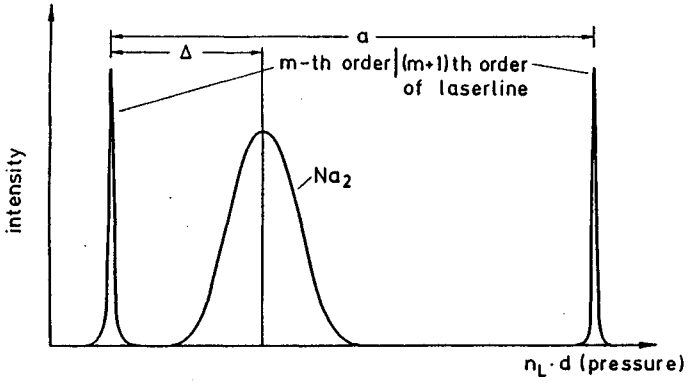

Fig.4.46. Photoelectric recording of a Doppler broadened laser-excited fluorescence line of Na_2 molecules in a vapor cell and the Doppler-free scattered laser line. The pressure scan Δp = a corresponds to one free spectral range of the FPI

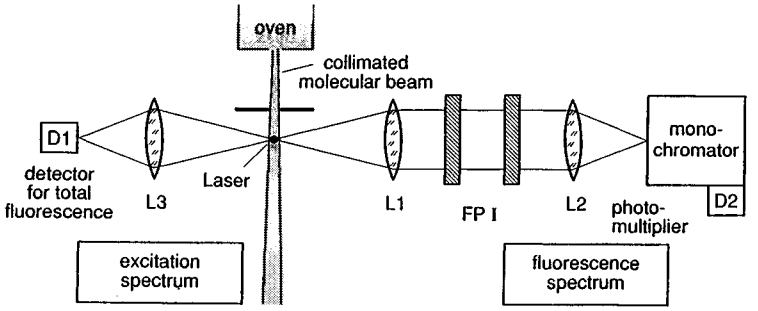

Fig.4.47. Experimental arrangement for photoelectric recording of high resolution fluorescence lines excited by a single mode laser in a collimated molecular beam and observed through FPI plus monochromator

(Fig.4.43). If the spectral interval $\Delta\lambda$ resolved by the monochromator is smaller then the free spectral range $\delta\lambda$ of the FPI, an unambigious determination of λ is possible. For illustration Fig.4.46 shows a Doppler-broadened fluorescence line of Na_2 molecules excited by a single-mode argon laser at λ = 488 nm, together with the narrow line profile of the scattered laser light. The pressure change $\Delta p \hat{=} 2d\Delta n_L$ = a corresponds to one free spectral range of the FPI, i.e., $2d\Delta n_L = \lambda$.

For Doppler-free resolution of fluorescence lines (Chap.9) the laser-induced fluorescence of molecules in a collimated molecular beam can be imaged through a FPI onto the entrance slit of the monochromator (Fig. 4.47). In this case the crossing point the laser and molecular beams, indded, represents a point source.

4.2.6 Confocal Fabry-Perot Interferometer

A confocal interferometer, sometimes called incorrectly a *spherical FPI*, consists of two spherical mirrors M_1, M_2 with equal curvatures (radius r) which oppose each other at a distance d = r (Fig.4.48a) [4.32-36]. These interferometers have gained great importance in laser physics: firstly, as high-resolution spectrum analyzers for detecting the mode structure and the linewidth of lasers [4.34-36]; and secondly, in the nearly confocal form, as laser resonators (Sect.5.2).

Neglecting spherical aberration, all light rays entering the interferometer parallel to its axis would pass through the focal point F and would reach the entrance point P1 again after having passed the confocal FPI four times. Figure 4.48b,c illustrate the general case of a ray which enters the confocal FPI at a small inclination θ and passes the successive points P1, A, B, C, P1 shown in Fig.4.48d in a projection. θ is the skew angle of the entering ray.

Because of spherical aberration rays with different distances ρ_1 from the axis will not all go through F but will intersect the axis at different positions F′ depending on ρ_1 and θ. Also each ray will not exactly reach the

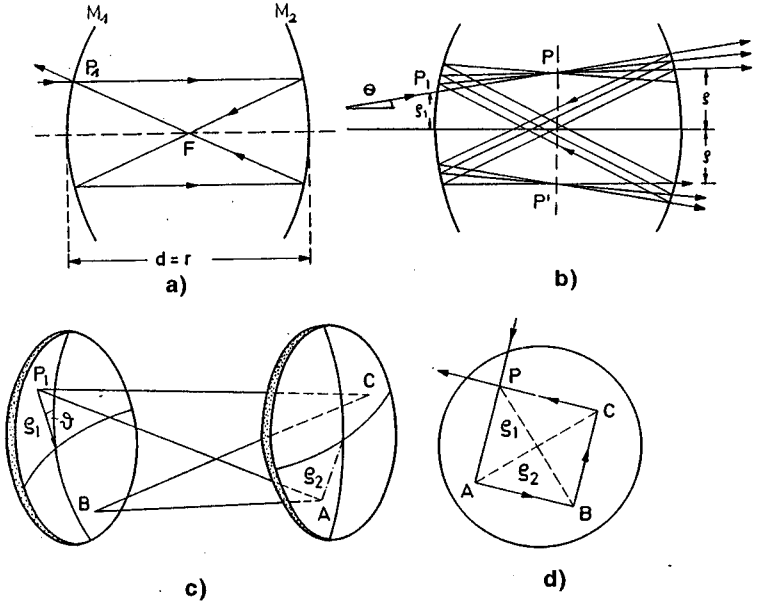

Fig.4.48. Trajectories of rays in a confocal FPI (a) incident beam parallel to the FPI axis (b) inclined incident beam (c) perspective view for illustrating the skew angle (d) projection of the skewed rays onto the mirror surfaces

entrance point P_1 after four passages through the confocal FPI since it is slightly shifted at successive passages. However, it can be shown [4.32,35] that for sufficiently small angles θ, all rays intersect in the vicinity of the two points P and P', located in the central plane of the confocal FPI at a distance $\rho(\rho_1,\theta)$ from the axis (Fig.4.48b).

The optical path difference Δs between two successive rays passing through P can be calculated from geometrical optics. For $\rho_1 \ll r$ and $\theta \ll 1$ one obtains for the near confocal case $d \approx r$ [4.35]

$$\Delta s = 4d + \rho_1^2\rho_2^2\cos 2\theta/r^3 + \text{higher-order terms} . \tag{4.68}$$

An incident light beam with diameter $D = 2\rho_1$ therefore produces, in the central plane of a confocal FPI, an interference pattern of concentric rings. Analogous of the treatment in Sect.4.2.5, the intensity $I(\rho,\lambda)$ is obtained by adding all amplitudes with their correct phases $\delta = \delta_0 + (2\pi/\lambda)\Delta s$. According to (4.51) we get

$$I(\rho,\lambda) = \frac{I_0 T^2}{(1-R)^2 + 4R\sin^2[(\pi/\lambda)\Delta s]} , \tag{4.69}$$

where $T = 1-R-A$ is the transmission of M_1. The intensity has maxima for $\delta = 2m\pi$, which is equivalent to

$$4d + \rho^4/r^3 = m\lambda \tag{4.70}$$

when we neglect the higher-order terms in (4.68) and set $\theta = 0$, and $\rho^2 = \rho_1\rho_2$.

The free spectral range $\delta\nu$, i.e., the frequency separation between successive interference maxima, is for the near-confocal FPI with $\rho \ll d$

$$\delta\nu = \frac{c}{4d + \rho^4/r^3} , \tag{4.71}$$

which is *different* from the expression $\delta\nu = c/2d$ for the plane FPI.

The radius ρ_m of the m^{th} order interference ring is obtained from (4.70),

$$\rho_m = [(m\lambda - 4d)r^3]^{1/4} \tag{4.72}$$

which reveals that ρ_m depends critically on the separation d of the spherical mirrors. Changing d by a small amount ϵ from $d = r$ to $d = r+\epsilon$ changes the path difference to

$$\Delta s = 4(r+\epsilon) + \rho^4/(r+\epsilon)^3 \sim 4(r+\epsilon) + \rho^4/r^3 . \tag{4.73}$$

For a given wavelength λ the value of ϵ can be chosen such that $4(r+\epsilon) = m_0\lambda$. In this case the radius of the central ring becomes zero. We can number the outer rings by the integer p and obtain with $m = m_0+p$ for the radius of the p^{th} ring the expression

$$\rho_p = (p\lambda r^3)^{1/4} . \tag{4.74}$$

The radial dispersion deduced from (4.72),

$$\frac{d\rho}{d\lambda} = \frac{mr^3/4}{[(m\lambda - 4d)r^3]^{3/4}} , \tag{4.75}$$

becomes infinite for $m\lambda = 4d$, which occurs according to (4.72) at the center with $\rho = 0$.

This large disperison can be used for high-resolution spectroscopy of narrow line profiles with a scanning confocal FPI and photoelectric recording (Fig.4.49).

If the central plane of the near-confocal FPI is imaged by a lens onto a circular aperture with sufficiently small radius $b < (\lambda r^3)^{1/4}$ only the central interference order is transmitted to the detector while all other orders are stopped. Because of the large radial dispersion for small ρ one obtains a high spectral resolving power. With this arrangement not only spectral line profiles but also the instrumental bandwidth can be measured, when an incident monochromatic wave (from a stabilized single-mode laser) is used.

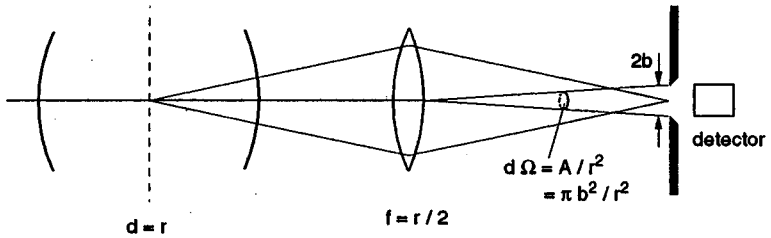

Fig.4.49. Photoelectric recording of the transmitted power of a scanning confocal FPI

The mirror separation $d = r+\epsilon$ is varied by the small amount ϵ and the power

$$P(\lambda, b, \epsilon) = 2\pi \int_{\rho=0}^{b} \rho I(\rho, \lambda, \epsilon)\, d\rho \tag{4.76}$$

transmitted through the aperture, is measured as a function of ϵ, at fixed values of λ and b.

The integrand $I(\rho,\lambda,\epsilon)$ can be obtained from (4.69), where the phase difference $\delta(\epsilon) = 2\pi\Delta s/\lambda$ is deduced from (4.73).

The optimum choice for the radius of the aperture is based on a compromise between spectral resolution and transmitted intensity. When the interferometer has the finesse F^*, the spectral halfwidth of the transmission peak is $\delta\nu/F^*$, see (4.54b), and the maximum spectral resolving power becomes $F^*\Delta s/\lambda$ (4.57). For the radius $b = (r^3\lambda/F^*)^{1/4}$ of the aperture, which is just $(F^*)^{1/4}$ times the radius ρ_1 of a fringe with $p = 1$ in (4.74), the spectral resolving power is reduced to about 70% of its maximum value. This can be verified by inserting this value of b into (4.76) and calculating the halfwidth of the transmission peak $P(\lambda_1, F^*, \epsilon)$.

The total finesse of the confocal FPI is, in general, higher than that of a plane FPI for the following reasons:

- The alignment of spherical mirrors is by far less critical than that of plane mirrors, because tilting of the spherical mirrors does not change (to a first approximation) the optical path length 4r through the confocal FPI, which remains approximately the same for all incident rays (Fig.4.50). For the plane FPI, however, the path length increases for rays below the interferometer axis, but decreases for rays above the axis.
- Spherical mirrors can be polished to a higher precision than plane mirrors. This means that the deviations from an ideal sphere are less for spherical mirrors than those from an ideal plane for plane mirrors.

Furthermore, such deviations do not wash out the interference structure but cause only a distortion of the ring system because a change of r allows the same path difference Δs for another value of ρ according to (4.68).

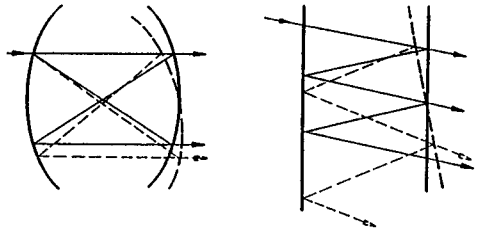

Fig.4.50. Illustration of the larger sensitivity against misalignment for the plane FPI compared with the spherical FPI

The total finesse of a confocal FPI is therefore mainly determined by the reflectivity R of the mirrors. For $R = 0.99$ a finesse $F^* = \pi\sqrt{R/(1-R)} \approx 300$ can be achieved, which is much higher than that obtainable with a plane FPI. With the mirror separation $r = d = 3$ cm, the free spectral range is $\delta = 2.5$ GHz, and the spectral resolution would be $\Delta\nu = 7.5$ MHz at the finesse $F^* = 300$. This is already sufficient to measure the natural linewidth of many optical transitions. With modern high-reflection coatings values of $R = 0.9995$ can be bobtained and confocal FPI with a finesse $F^* \geq 10^4$ have been realized [4.37].

From Fig.4.49 we see that the solid angle accepted by the detector behind the aperture with radius $b = (r^3\lambda/F^*)^{1/4}$ is $\Omega = \pi b^2/r^2$. The light power transmitted to the detector is proportional to the product (often called the *étendue*)

$$U = A\Omega = \pi^2 b^4/r^2 = \pi^2 r\lambda/F^* \tag{4.77}$$

of the solid angle Ω and area A in the central plane, which is imaged by the lens onto the aperture. For a given finesse F^*, the étendue increases with the mirror separation $d = r$. Since the free spectral range $\delta\nu = c/4r$ decreases with increasing r, the spectral resolving power

$$\frac{\nu}{\Delta\nu} = 4\,F^*\,\frac{r}{\lambda} \tag{4.78}$$

of the confocal FPI is proportional to the product of finesse F^* and the ratio of mirror separation $r = d$ to the wavelength λ. With a given étendue $U = \pi^2 r\lambda/F^*$ the spectral resolving power is

$$(\nu/\Delta\nu) = [2F^*/(\pi\lambda)]^2 U \quad \text{(confocal FPI)}\,. \tag{4.79}$$

Let us compare this with the situation in case of a plane FPI with the plate diameter D and the separation d, which is illuminated with nearly parallel light (Fig.4.45). According to (4.63) the path difference between a ray parallel to the axis and a ray with an inclination β is for small β given by $\Delta s = nd\beta^2$. To achieve a finesse F^* with photoelectric recording, this variation of

the path length should not exceed λ/F^*, which restricts the solid angle $\Omega = \beta^2$ acceptable by the detector to $\Omega \leq \lambda/(dF^*)$. The étendue is therefore

$$U = A\Omega = \pi \frac{D^2}{4} \frac{\lambda}{dF^*} . \tag{4.80}$$

Inserting the value of d given by this equation into the spectral resolving power, $\nu/\Delta\nu = 2dF^*/\lambda$, we obtain

$$\frac{\nu}{\Delta\nu} = \frac{\pi D^2}{2U} \quad \text{(plane FPI)} . \tag{4.81}$$

While the spectral resolving power is proportional to U for the confocal FPI it is *inversely proportional to U for the plane FPI.* The reason for this is that the étendue increases with the mirror separation d for the confocal FPI but decreases proportional to 1/d for the plane FPI. For a mirror radius $r > D^2/4d$ the étendue of the confocal FPI is larger than that of a plane FPI with equal spectral resolution.

Example 4.12

A confocal FPI with r = d = 5 cm has for λ = 500 nm the same étendue as a plane FPI with d = 5 cm and D = 10 cm. However, the diameter of the spherical mirrors can be much smaller (less than 5mm). With a finesse F^* = 100 the spectral resolving power is $\nu/\Delta\nu = 4 \cdot 10^7$ and the étendue U = $8 \cdot 10^{-6}$ [cm^2·sterad]. With this étendue the resolving power of the plane FPI is $2 \cdot 10^7$, provided the whole plane mirror surface has a surface quality to allow a surface finesse of $F^* \geq 100$. In practice, it is difficult to achieve this surface quality for a flat plane with D = 10 cm diameter while for the small spherical mirrors $F^* > 10^3$ is feasible.

More detailed information on the history, theory, practice and application of plane and spherical Fabry-Perot-interferometers may be found in [4.38-40].

4.2.7 Multilayer Dielectric Coatings

The constructive interference found for the reflection of light from plane, parallel interfaces between two regions with different refractive indices can be utilized to produce highly reflecting, essentially absorption-free mirrors. The improved technology of such dielectric mirrors has greatly supported the development of visible and ultraviolet laser systems.

The reflectivity R of a plane interface between two regions with complex refractive indices $n_1 = n_1' - i\kappa_1$ and $n_2 = n_2' - i\kappa_2$ can be calculated from

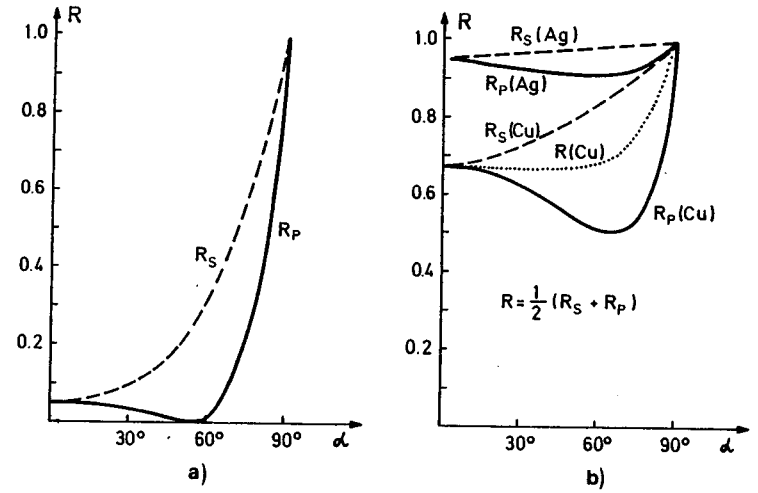

Fig.4.51. Reflectivities R_p and R_s for the two polarization components parallel and perpendicular to the plane of incidence as a function of the angle of incidence α (a) Boundary air-glass (n = 1,5) (b) Boundary air-metal for Cu(n' = 0.76, κ = 3.32) and Ag(n' = 0.055, κ = 3.32)

Fresnel's formulas [4.13]. It depends on the angle of incidence α and on the direction of polarization. $R(\alpha)$ is illustrated in Fig.4.51 for three different materials for incident light polarized parallel (R_p) and perpendicular (R_s) to the plane of incidence.

For vertical incidence (α = 0) one obtains from Fresnel's formulas for both polarizations

$$R|_{\alpha=0} = \left(\frac{n_1 - n_2}{n_1 + n_2}\right)^2 . \tag{4.82}$$

Since this case represents the most common situation for laser mirrors, we shall restrict the following discussion to vertical incidence.

To achieve maximum reflectivities, the numerator $(n_1 - n_2)^2$ should be maximized and the denominator minimized. Since n_1 is always larger than one, this implies that n_2 should be as large as possible. Unfortunately, the dispersion relations (3.36,37) imply that a large value of n also causes large absorption. For instance, highly polished metal surfaces have a maximum reflectivity of R = 0.95 in the visible spectral range. The residual 5% of the incident intensity is absorbed and is therefore lost.

The situation can be improved by selecting reflecting materials with low absorption (which then necessarily have also low reflectivity) but using many layers with alternating high and low refractive index n. Choosing the proper optical thickness nd of each layer, allows constructive interference between the different reflected amplitudes to be achieved. Reflectivities of up to R = 0.9995 have been reached [4.41-44].

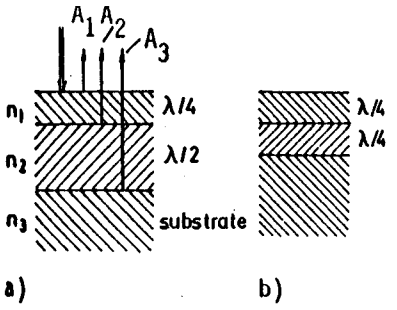

Fig.4.52a,b. Maximum reflection of light with wavelength λ by a two-layer dielectric coating. (a) $n_1 > n_2 > n_3$ (b) $n_1 > n_2 < n_3$

Figure 4.52 illustrates such constructive interference for the example of a two-layer coating. The layers with refractive indices n_1, n_2 and thicknesses d_1, d_2 are evaporated onto an optically smooth substrate with the refractive index n_3. The phase differences between all reflected components have to be $\delta_m = 2m\pi$ (m = 1,2,3,...) for constructive interference. Taking into account the phase shift $\delta = \pi$ at reflection from an interface with a larger refractive index, we obtain the conditions

$$n_1 d_1 = \lambda/4 \quad \text{and} \quad n_2 d_2 = \lambda/2 \quad \text{for} \quad n_1 > n_2 > n_3 \tag{4.83a}$$

and

$$n_1 d_1 = n_2 d_2 = \lambda/4 \quad \text{for} \quad n_1 > n_2;\ n_3 > n_2\ . \tag{4.83b}$$

The reflected amplitudes can be calculated from Fresnel's formulas. The total reflected intensity is obtained by summation over all reflected amplitudes taking into account the correct phase. The refractive indices are now selected such that ΣA_i becomes a maximum. The calculation is still feasible for our example of a two-layer coating, and yields for the three reflected amplitudes (double reflections are neglected)

$$A_1 = \sqrt{R_1}\, A_0\ ; \quad A_2 = \sqrt{R_2}\,(1 - \sqrt{R_1})\, A_0\ ;$$

$$A_3 = \sqrt{R_3}\,(1 - \sqrt{R_2})(1 - \sqrt{R_1})\, A_0\ .$$

Example 4.13

$|n_1| = 1.6$; $|n_2| = 1.2$; $|n_3| = 1.45$. $A_1 = 0.231A_0$; $A_2 = 0.143A_0$; $A_3 = 0.094A_0$. $A_R = \Sigma A_i = 0.468A_0 \rightarrow I_R = 0.22I_0 \rightarrow R = 0.20$, provided the path differences have been choosen correctly.

This examples illustrates that for materials with low absorption, many layers are necessary to achieve a high reflectivity. Figure 4.53a depicts schematically the composition of a dielectric multilayer mirror. The calculation and optimization of mulitlayer coatings with up to 20 layers becomes very tedious and time consuming, it is therefore performed using computer

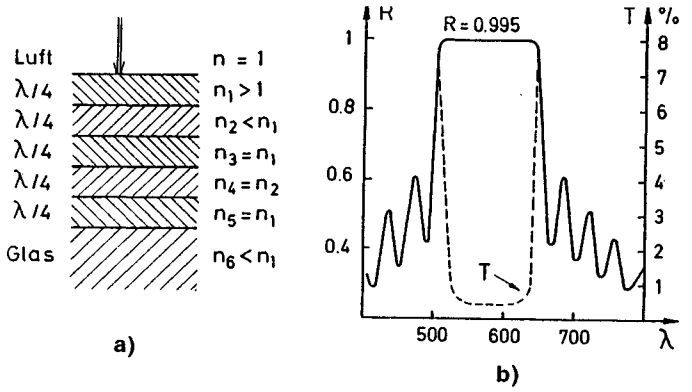

Fig.4.53a,b. The dielectric multilayer mirror. (a) Composition of multilayers. (b) Reflectivity of a high-reflectance multilayer mirror as a function of the incident wavelength λ

programs [4.42,44]. Figure 4.53b illustrates the reflectivity $R(\lambda)$ of a high-reflectance mirror with 17 layers.

By proper selection of different layers with slightly different optical path lengths, one can achieve a high reflectivity over an extended spectral range. Nowadays, such "broad-band" reflectors are available which have a reflectivity of $R \geq 0.99$ within the spectral range $(\lambda_0 \pm 0.2\lambda_0)$ while the absorption losses are less than 0.2% [4.41-43]. At such low absorption losses the scattering of light from imperfect mirror surfaces may become the major loss contribution. When total losses of less than 0.5% are demanded, the mirror substrate has to be of high optical quality (better than $\lambda/20$), the dielectric layers have to be evaporated very uniformly, and the mirror surface must be clean and free of dust or dirty films [4.44].

Instead of maximizing the reflectivity of a dielectric multilayer coating through *constructive* interference, it is, of course, also possible to minimize it by destructive interference. Such *antireflection coatings* are commonly used to minimize unwanted reflections from the many surfaces of multiple-lens camera objectives, which would otherwise produce an annoying background illumination of the photomaterial. In laser spectroscopy such coatings are important for minimizing reflection losses of optical components inside the laser resonator and for avoiding reflections from the back-surface of output mirrors which would introduce undesirable couplings, causing frequency instabilities of single-mode lasers.

Using a single layer (Fig.4.54a) the reflectivity reaches a minimum only for a selected wavelength λ (Fig.4.55). We obtain $I_R = 0$ for $\delta = (2m+1)\pi$, if the two amplitudes A_1 and A_2 reflected by the interfaces (n_1, n_2) and (n_2, n_3) are equal. For vertical incidence this gives the condition

$$R_1 = \left(\frac{n_1 - n_2}{n_1 + n_2}\right)^2 = R_2 = \left(\frac{n_2 - n_3}{n_2 + n_3}\right)^2\ , \tag{4.84}$$

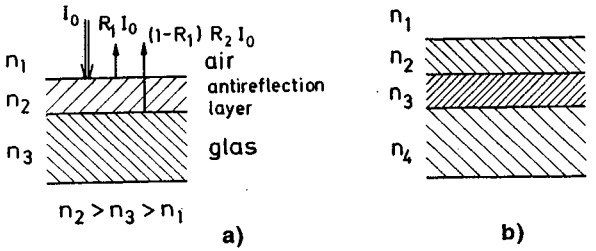

Fig.4.54. Antireflection coating (a) single layer, (b) multilayer coating

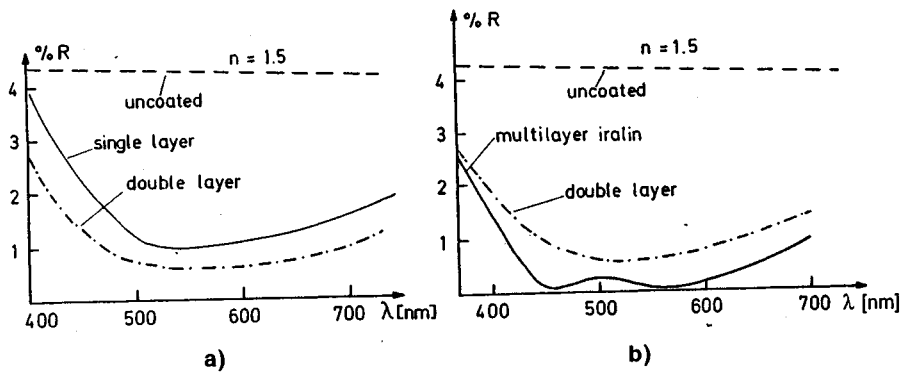

Fig.4.55. Wavelength dependence of the reflectivity ($R(\lambda)$ at normal incidence on a substrate with n = 1.5 at λ = 550 nm, for uncoated substrate, single, double and multilayer antireflection coatings

which can be reduced to

$$n_2 = \sqrt{n_1 n_3}\,. \tag{4.85}$$

For a single layer on a glass substrate the values are $n_1 = 1$ and $n_3 = 1.5$. According to (4.85) n_2 should be $n_2 = \sqrt{1.5} = 1.23$. Durable coatings with such low refractive indices are not available. One often uses MgF_2 with $n_2 = 1.38$, giving a reduction of reflection from 4% to 1.2% (Fig.4.55).

With multilayer antireflection coatings the reflectivity can be decreased below 0.2 for an extended spectral range [4.45]. For instance, with three $\lambda/4$ layers (MgF_2, SiO, and CeF_3) the reflection drops to below 1% for the whole range between 4200 and 8400 Å [4.41,46,47]

4.2.8 Interference Filters

Interference filters are used for a selective transmission in a narrow spectral range. Incident radiation of wavelength outside this transmission range is

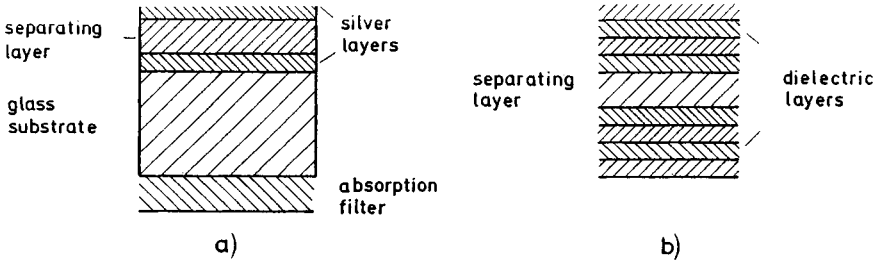

Fig.4.56a,b. Interference filters of the Fabry-Perot type. (a) with two single layers of silver (b) with dielectric multilayer coatings

either reflected or absorbed. One distinguishes between line filters and band-pass filters.

A line filter is essentially a Fabry-Perot etalon with a very small optical path nd between the two reflecting surfaces. The technical realization uses two highly reflecting coatings (either silver coatings or dielectric multilayer coatings) which are separated by a nonabsorbing layer with a low refractive index (Fig.4.56). For nd = 0.5 μm for instance, the transmission maxima for vertical incidence are obtained from (4.59a) at $\lambda_1 = 1$ μm, $\lambda_2 = 0.5$ μm, $\lambda_3 = 0.33$ μm, etc. In the visible range this filter has therefore only one transmission peak at $\lambda = 500$ nm, with a halfwidth which depends on the finesse $F^* = \pi\sqrt{R}/(1-R)$ (Fig.4.37).

The interference filter is characterized by the following quantities:

- The wavelength λ_m at peak transmission.
- The maximum transmission.
- The contrast factor, which gives the ratio of maximum to minimum transmission.
- The bandwidth at half transmitted peak intensity.

The maximum transmission is according to (4.58) $T^*_{max} = T^2/(1-R)^2$. Using thin silver or aluminum coatings with R = 0.8, T = 0.1, and A = 0.1 the transmission of the filter is only $T^* = 0.25$ and the finesse $F^* = 15$. For our example this means a halfwidth of 660 cm^{-1} at a free spectral range of 10^4 cm^{-1}. At $\lambda = 500$ nm this corresponds to a halfwidth of about 16 nm. For many applications in laser spectroscopy the low peak transmission of interference filters with absorbing metal coatings is not tolerable. One has to use absorption-free dielectric multilayer coatings (Fig.4.56b) with high reflectivity, which allows a large finesse and therefore a smaller bandwidth and a larger peak transmission (Fig.4.57).

Example 4.14

With R = 0.95, A = 0.01 and T = 0.04 we obtain according to (4.58) a peak transmission of 64%, which increases with A = 0.005, T = 0.045 already to 81%. For a free spectral range $\delta\nu = 3 \cdot 10^{12}$ Hz $\hat{=}$ 4 μm the contrast becomes $\gamma = (1+F) = 1520$.

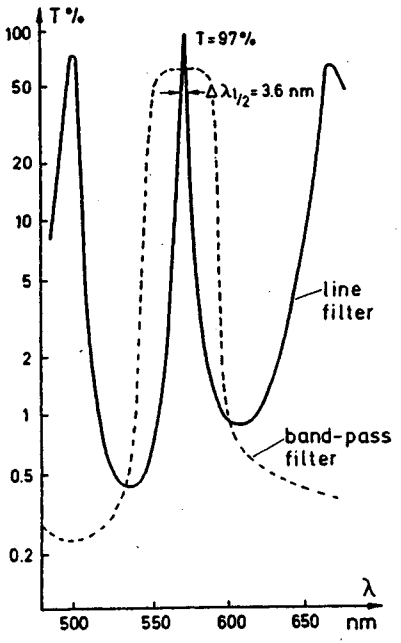

Fig.4.57. Spectral transmission of interference filters. Solid curve: line filter. Dashed curve: band-pass filter

A higher finesse F^*, due to larger reflectivities of the reflecting films, not only decreases the bandwidth but also increases the contrast factor which is according to (4.58c) equal to $(1+F) = 1+4F^{*2}/\pi^2$. With $R = 0.95 \rightarrow F = 4R/(1-R)^2 = 1.7 \cdot 10^3$, which means that the intensity at the transmission minimum is less than 0.1% of the peak transmission.

The bandwidth can be further decreased by using two interference filters in series. However, it is preferable to construct a double filter which consists of three highly-reflecting surfaces, separated by two nonabsorbing layers of the same optical thickness. If the thickness of these two layers is made slightly different, a band-pass filter results which has a flat transmission curve but step slopes to both sides. Nowadays commercial interference filters are available with a peak transmission of at least 90% and a bandwidth of less than 2 nm [4.48]. Special narrow-band filters even reach 0.3 nm, however, with reduced peak transmission.

The wavelength λ_m of the transmission peak can be shifted to lower values by tilting the interference filter, which increases the angle of incidence α, see (4.74a). The tuning range is, however, restricted, because the reflectivity of the multilayer coatings also depends on the angle α and is in general optimized for $\alpha = 0$. The transmission bandwidth increases for divergent incident light with the divergence angle.

In the ultraviolet region where the absorption of most materials, used for interference filters, becomes large, the selective *reflectance* of interfer-

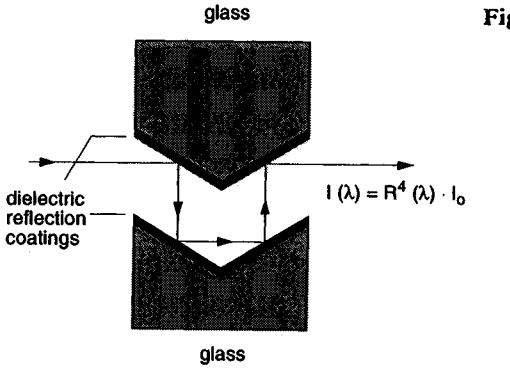

Fig.4.58. Reflection interference filter

ence filters can be utilized to achieve narrow-band filters with low losses (Fig.4.58). For more detailed treatment, see [4.41-48].

4.2.9 Birefringent Interferometer

The basic principle of the birefringent interferometer or *Lyot filter* [4.20, 49] is founded on the interference of polarized light after having passed a birefringent crystal. Assume that a linearly polarized plane wave $E = A_0 \times\cos(\omega t - kx)$ with

$$A = (0, A_y, A_z)\,; \quad A_y = |A|\sin\alpha\,; \quad A_z = |A|\cos\alpha$$

is incident on the birefringent crystal (Fig.4.59). The electric vector E makes an angle α with the optical axis, pointing into the z direction. Within the crystal, the wave is split into an ordinary beam with the wave number $k_o = n_o k$ and the phase velocity $v_o = c/n_o$, and an extraordinary beam with $k_e = n_e k$ and $v_e = c/n_e$. The partial waves have mutually orthogonal polarization in directions parallel to the y and z axis, respectively. Let the crystal with length L be placed between x = 0 and x = L. Because of the different

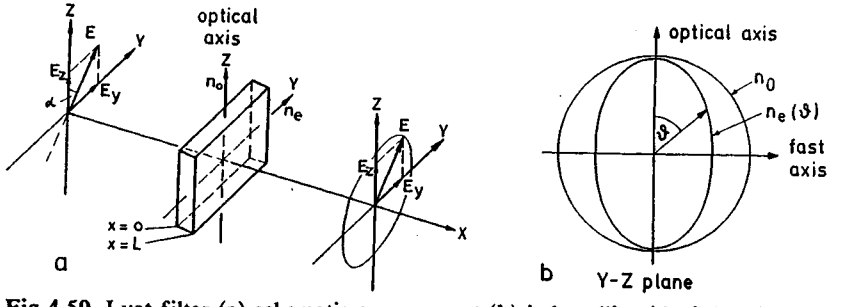

Fig.4.59. Lyot filter (a) schematic arrangement (b) index ellipsoid of the birefringent crystal

refractive indices n_o and n_e for the ordinary and the extraordinary beams, the two partial waves at x = L,

$$E_y(L) = A_y \cos(\omega t - k_e L)$$

and

$$E_z(L) = A_z \cos(\omega t - k_0 L) ,$$

show a phase difference of

$$\phi = k(n_0 - n_e)L = (2\pi/\lambda)\Delta nL \quad \text{with} \quad \Delta n = n_0 - n_e . \tag{4.86}$$

The superposition of these two waves results, in general, in elliptically polarized light, where the axis of the ellipse is turned by an angle $\beta = \phi/2$ against the direction of A_0.

For phase differences $\phi = 2m\pi$ linearly polarized light with E(L) || E(0) is obtained, while for $\phi = (2m+1)\pi$ and $\alpha = 45°$, the transmitted wave is also linearly polarized but now E(L) ⊥ E(0).

The elementary Lyot filter consists of a birefringent crystal placed between two linear polarizers (Fig.4.59a). Assume that the two polarizers are both parallel to the electric vector E(0) of the incoming wave. The second polarizer parallel to E(0) transmits only the projection

$$E = E_y \sin\alpha + E_z \cos\alpha = A[\sin^2\alpha \cos(\omega t - k_e L) + \cos^2\alpha \cos(\omega t - k_0 L)]$$

of the amplitudes which yields the transmitted time averaged intensity

$$\bar{I} = \frac{1}{2} c\epsilon_0 \overline{E^2} = \bar{I}_0(\sin^4\alpha + \cos^4\alpha + 2\sin^2\alpha\cos^2\alpha\cos\phi) . \tag{4.87}$$

Using the relations $\cos\phi = 1 - 2\sin^2\frac{1}{2}\phi$, and $2\sin\alpha\cos\alpha = \sin 2\alpha$, this reduces to

$$I = I_0[1 - \sin^2\tfrac{1}{2}\phi \sin^2(2\alpha)] ; \tag{4.88}$$

which gives for $\alpha = 45°$

$$I = I_0[1 - \sin^2\tfrac{1}{2}\phi] = \bar{I}_0 \cos^2\tfrac{1}{2}\phi . \tag{4.88a}$$

The transmission of the Lyot filter is therefore a function of the phase retardation, i.e.,

$$T(\lambda) = \frac{I_T}{I_0} = T_0 \cos^2\left(\frac{\pi\Delta nL}{\lambda}\right). \tag{4.89}$$

Taking into account absorption and reflection losses, the maximum transmission $I_T/I_0 = T_0 < 1$ becomes less than 100%. Within a small wavelength interval, the difference $\Delta n = n_0 - n_e$ can be regarded as constant, and

(4.89) gives the wavelength-dependent transmission function $\cos^2\phi$ typical of a two-beam interferometer (Fig.4.26). For extended spectral ranges the different dispersion of $n_o(\lambda)$ and $n_e(\lambda)$ has to be considered, which causes a wavelength dependence, $\Delta n(\lambda)$.

The free spectral range $\delta\nu$ is obtained from (4.89) with $\nu = c/\lambda$ as

$$\delta\nu = \frac{c}{(n_o - n_e)L} . \tag{4.90}$$

Note that according to (4.88) the maximum modulation of the transmittance with $T_{max} = T_0$ and $T_{min} = 0$ is only achieved for $\alpha = 45°$!

Example 4.15

For a crystal of potassium dihydrogen phosphate (KDP), $n_e = 1.51$, $n_0 = 1.47 \rightarrow \Delta n = 0.04$ at $\lambda = 600$ nm. A crystal with L = 2 cm has then a free spectral range $\delta\nu = 3.75 \cdot 10^{11}$ Hz $= \delta\bar{\nu} = 12.5$ cm$^{-1} \rightarrow \Delta\lambda = 0.3$ nm at $\lambda = 500$ nm.

If N elementary Lyot filters with different lengths L_m are placed in series, the total transmission T is the product of the different transmissions T_m, i.e.,

$$T(\lambda) = \prod_{m=1}^{N} T_{0m} \cos^2\left(\frac{\pi\Delta nL_m}{\lambda}\right) . \tag{4.91}$$

Figure 4.60 illustrates a possible experimental arrangement and the corresponding transmission for a Lyot filter composed of three components with the lengths $L_1 = L$, $L_2 = 2L$, and $L_3 = 4L$. The free spectral range $\delta\nu$ of this filter equals that of the shortest component; the halfwidth $\Delta\nu$ of the transmission peaks is, however, mainly determined by the longest component. When we define, analogous to the Fabry-Perot interferometer, the finesse F of the Lyot filter as the ratio of the free spectral range $\delta\nu$ to the halfwidth $\Delta\nu$, we obtain, for a composite Lyot filter with N elements of lengths $L_m = 2^{m-1}L_1$, a finesse which is approximately $F^* = 2^N$.

The wavelength of the transmission peak can be tuned by changing the difference $\Delta n = n_o - n_e$. This can be realized in two different ways:

- By changing the angle θ between the optical axis and the wave vector **k**, which alters the index n_e. This can be illustrated with the index ellipsoid (Fig.4.59b), which gives both refractive indices for a given wavelength as a function of θ. The difference $\Delta n = n_o - n_e$ therefore depends on θ. The two axes of the ellipsoid with minimum n_e and maximum n_o are often called the *fast* and the *slow* axes. Turning the crystal around the x axis in Fig. 4.59a, which is perpendicular to the yz

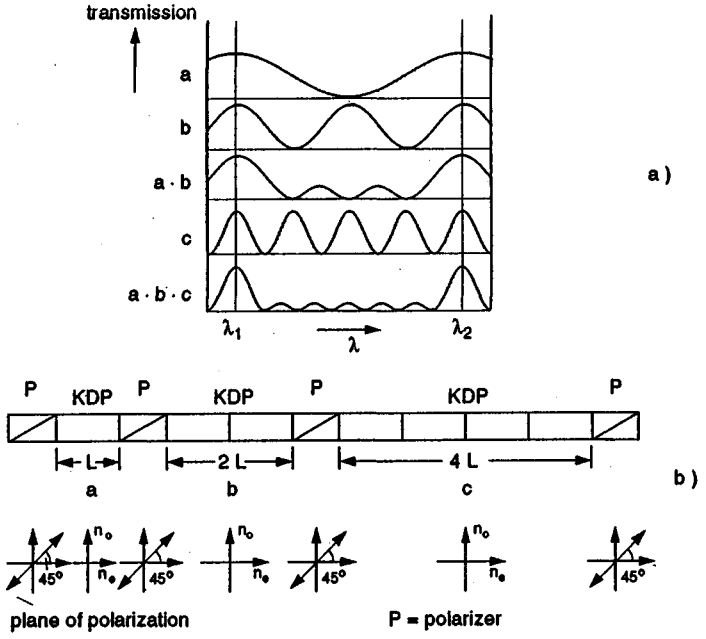

Fig.4.60. (a) Transmitted intensity $I_T(\lambda)$ of a Lyot filter composed of three birefringent crystals with lengths L, 2L and 4L between polarizers. (b) Arrangement of the crystals and the state of polarization of the transmitted wave

plane of Fig.4.59b, results in a continuous change of Δn and a corresponding tuning of the peak transmission wavelength λ (Sect. 5.7.5).

- By using the different dependence of the refractive indices n_o and n_e on an applied electric field [4.51]. This "induced birefringence" depends on the orientation of the crystal axis in the electric field. A common arrangement employs a KDP (Kalium-Dihydrogen Phosphat) crystal with an orientation where the electric field is parallel to the optical axis (z axis) and the wave vector **k** of the incident wave is perpendicular to the z direction (transverse electro-optic effect) (Fig.4.61). Two opposite sides of the rectangular crystal with the side length d are coated with gold electrodes and the electric field $E = U/d$ is controlled by the applied voltage.

In the external electric field the uniaxial crystal becomes biaxial. In addition to the natural birefringence of the uniaxial crystal, a field-induced birefringence is generated, which is approximately proportional to the field strength E [4.52]. The changes of n_o or n_e by the electric field depend on the symmetry of the crystal, the direction of the applied field and on the magnitude of the electro-optic coefficients. For the KDP crystal only one electro-optic coefficient $d_{36} = -10.7 \cdot 10^{-12}$ [m/V] is effective if the field is applied parallel to the optical axis.

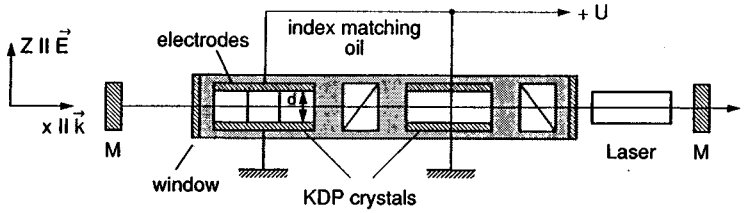

Fig.4.61. Electro-optic tuning of Lyot filter [4.50]

The difference $\Delta n = n_o - n_e$ then becomes

$$\Delta n(E_z) = \Delta n_o(E=0) + \frac{1}{2} n_1^3 d_{36} E_z \,. \tag{4.92}$$

Maximum transmittance is obtained for

$$(\Delta n_o + \Delta n_{el})L = m\lambda \quad (m = 0, 1, 2 \ldots)$$

which gives the wavelength λ at the maximum transmittance

$$\lambda = (\Delta n + 0.5 n_1^3 d_{36} E_z)L/m \tag{4.93}$$

as a function of the applied field.

While this electro-optic tuning of the Lyot filter allows rapid switching of the peak transmission, for many applications, where a high tuning speed is not demanded, mechanical tuning is more convenient, and easier to realize.

4.2.10 Tunable Interferometers

For many applications in laser spectroscopy it is advantageous to have a high-resolution interferometer which is able to scan, in a given time interval Δt, through a limited spectral range $\Delta\nu$. The scanning speed $\Delta\nu/\Delta t$ depends on the method used for tuning, and the spectral range $\Delta\nu$ is limited by the free spectral range $\delta\nu$ of the instrument. All techniques for tuning the wavelength $\lambda_m = 2nd/m$ at the transmission peak of an interferometer are based on a continuous change of the optical path difference between successive interferring beams. This can be achieved in different ways:

(a) Change of the refractive index n by altering the pressure between the reflecting plates of a FPI (pressure-scanned FPI).
(b) Change of the distance d with piezoelectric or magnetostrictive elements.
(c) Tilting of solid etalons with a given thickeness d against the direction of the incoming plane wave.

(d) Change of the optical path difference $\Delta s = \Delta n L$ in birefringent crystals by electro-optic tuning or by turning the optical axis of the crystal (Lyot filter)

While method (a) is often used for high-resolution fluorescence spectroscopy with slow scan rates or for tuning pulsed dye lasers, method (b) is realized in a scanning confocal FPI (used as optical spectrum analyzer) for monitoring the mode structure of lasers.

With a commercial "spectrum analyzer", the transmitted wavelength λ can be repetitively scanned over more than one free spectral range with a saw-tooth voltage applied to the piezoelectric distance holder [4.34, 53]. Scanning rates up to several kilohertz are possible. Although the finesse of such devices may exceed 10^3, the hysteresis of piezoelectric crystals limits the accuracy of absolute wavelength calibration. Here a pressure-tuned FPI may be advantageous. The pressure change has to be sufficiently slow to avoid turbulence and temperature drifts. With a digitally pressure-scanned FPI, where the pressure of the gas in the interferometer chamber is changed by small, discrete steps, repetitive scans are reproduced within about 10^{-3} of the free spectral range [4.54].

For fast wavelength tuning of dye lasers, Lyot filters with electro-optic tuning are employed within the laser resonator. A tuning range of a few nm can be repetitively scanned with rates up to 10^5 per second [4.55].

4.3 Comparison Between Spectrometers and Interferometers

When comparing the advantages and disadvantages of different dispersing devices for spectroscopic analysis, the characteristic properties of the instruments discussed in the foregoing sections, such as *spectral resolving power, étendue, spectral transmission*, and *free spectral* range, are important for the optimum choice. Of equal significance is the question of how accurately the wavelengths of spectral lines can be measured. To answer this question, further specifications are necessary, such as the backlash of monochromator drives, imaging errors in spectrographs, hysteresis in piezo-tuned interferometers, etc. In this section we shall treat these points in a comparison for different devices in order to give the reader an impression of the capabilities and limitations of these instruments.

4.3.1 Spectral Resolving Power

The spectral resolving power discussed for the different instruments in the previous sections can be expressed in a more general way which applies to all devices with spectral dispersion based on interference effects. Let Δs_m be the maximum path difference between interfering waves in the instrument, e.g., between the rays from the first and the last groove of a grating (Fig.4.62a) or between the direct beam and a beam reflected m times in a Fabry-Perot interferometer (Fig.4.62b). Two wavelengths λ_1 and $\lambda_2 = \lambda_1 + \Delta\lambda$ can still be resolved if the number of wavelengths over this maximum path difference

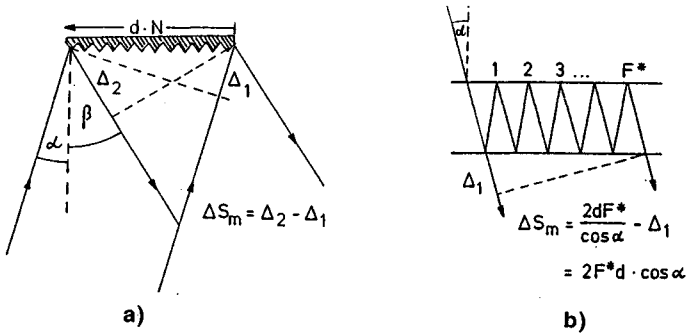

Fig.4.62. Maximum optical path difference and spectral resolving power (a) in a grating spectrometer (b) in a Fabry-Perot interferometer

$$\Delta s_m = m\lambda_2 = (m + 1)\lambda_1$$

differs for the two wavelengths at least by one unit. In this case an interference maximum for λ_1 coincides with the first minimum for λ_2. From the above equation we obtain the theoretical upper limit for the resolving power

$$\boxed{\frac{\lambda}{\Delta\lambda} = \frac{\Delta s_m}{\lambda}} \tag{4.94}$$

which is equal to the maximum path difference measured in units of the wavelength λ.

With the maximum time difference $\Delta T_m = \Delta s_m / c$ for traversing the two paths with the path difference Δs_m, we obtain with $\nu = c/\lambda$ from (4.94) for the minimum resolvable interval $\Delta\nu = -(c/\lambda^2)\Delta\lambda$,

$$\Delta\nu = 1/\Delta T_m \Rightarrow \Delta\nu \cdot \Delta T_m = 1 \,. \tag{4.95}$$

The product of the minimum resolvable frequency interval $\Delta\nu$ *and the maximum difference in transit times through the spectral apparatus is equal to* 1.

Example 4.16

a) Grating Spectrometer. The maximum path difference is, according to (4.31) and Fig.4.62,

$$\Delta s = Nd(\sin\alpha - \sin\beta) = mN\lambda \ .$$

The upper limit for the resolving power is therefore according to (4.94)

$$R = \lambda/\Delta\lambda = mN \quad \text{(m: diffraction order, N: number of grooves)} \ .$$

For $m = 2$ and $N = 10^5$ this gives $R = 2\cdot10^5$, or $\Delta\lambda = 5\cdot10^{-6}\lambda$. Because of diffraction (Sect.4.1.2), the realizable resolving power is 3÷4 times lower. This means that at $\lambda = 500$ nm two lines with $\Delta\lambda \geq 0.1$ Å can still be resolved.

b) Michelson Interferometer. The path difference Δs between the two interfering beams is changed from $\Delta s = 0$ to $\Delta s = \Delta s_m$, and the numbers of interference maxima are counted for the two components λ_1 and λ_2 (Sect. 4.2.3). A distinction between λ_1 and λ_2 is possible if the number $m_1 = \Delta s/\lambda_1$ differs at least by 1 from $m_2 = \Delta s/\lambda_2$; this immediately gives (4.94). With a modern design, maximum path differences Δs up to several meters have been realized for wavelength measurements of stabilized lasers (Sect.4.5.3). For $\lambda = 500$ nm and $\Delta s = 1$ m, we obtain $\lambda/\Delta\lambda = 2\cdot10^6$, which is one order of magnitude better than for the grating spectrometer.

c) Fabry-Perot Interferometer. The path difference is determined by the optical path difference 2nd between successive partial beams times the effective number of reflections which can be expressed by the reflectivity finesse $F^* = \pi\sqrt{R}/(1-R)$. With ideal reflecting planes and perfect alignment, the maximum path difference would be $\Delta s_m = 2ndF^*$ and the spectral resolving power according to (4.94)

$$\lambda/\Delta\lambda = F^* 2nd/\lambda \ .$$

Because of imperfections of the alignment and deviations from ideal planes, the effective finesse is lower than the reflectivity finesse. With a value of $F^*_{eff} = 50$, which can be achieved, we obtain for nd = 1 cm

$$\lambda/\Delta\lambda = 2\cdot10^6 \ ,$$

which is comparable with the Michelson interferometer having $\Delta s_m = 100$ cm. However, with a confocal FPI, a finesse of $F^*_{eff} = 1000$ can be achieved. With r = d = 4 cm we then obtain

$$\lambda/\Delta\lambda = F^* 4d/\lambda \approx 5\cdot10^8$$

which means that for $\lambda = 500$ nm, two lines with $\Delta\lambda = 1\cdot10^{-5}$ Å ($\Delta\nu = 1$MHz at $\nu = 5\cdot10^{14}s^{-1}$) are still resolvable, provided that their linewidth is sufficiently small.

4.3.2 Light-Gathering Power

The *light-gathering power*, or *étendue*, has been defined in Sect.4.1.1 as the product $U = A\Omega$ of entrance area A and solid angle of acceptance, Ω, of the spectral apparatus. For most spectroscopic applications it is desirable to have an étendue U as large as possible to gain intensity. An equally important goal is to reach a maximum resolving power R. However, the two quantitites U and R are not independent of each other but are related, as can be seen from the following examples.

Example 4.17

a) Spectrometer. The area of the entrance slit with width b and heights h is $A = b\cdot h$. The acceptance angle $\Omega = (a/f)^2$ is determined by the focal length of the collimating lens or mirror and the diameter a of the limiting aperture in the spectrometer (Fig.4.63a). We can write the étendue,

$$U = bha^2/f^2 = (bh/f^2)a^2 = \Omega^* a^2 \ ,$$

as the product of the area $S = a^2$ of the limiting aperture and the solid angle $\Omega^* = bh/f^2$ under which the entrance slit is seen from the center of the collimating mirror. This illustrates that the entrance slit forms the effective source area which is imaged onto the plane of observation.

Using typical figures for a medium-sized spectrometer ($b = 10\mu$m, h = 0.5cm, a = 10cm, f = 100cm) we obtain $\Omega = 0.01$, $A = 5\cdot10^{-4}$ cm^2 → $U = 5\cdot10^{-6}$ cm$^2\cdot$ster. According to (4.11,30) the spectral resolving power for a grating with size $a = N\cdot d$ used in the mth order and a slitwidth b large compared to the minimum width $b_{min} = 2f\lambda/a$ is given by

$$R = \frac{\lambda}{\Delta\lambda} \approx \left(f\frac{\lambda}{b}\right)\frac{d\beta}{d\lambda} = mf\lambda \ .$$

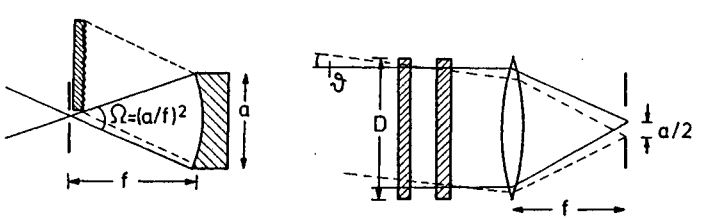

Fig.4.63. Acceptance angle of a spectrometer **(a)** and a Fabry-Perot interferometer **(b)**

The product

$$RU = mNA\Omega \approx mN\frac{bha^2}{f^2} \tag{4.96a}$$

increases with the diffraction order m, the size a of the grating, the number of illuminated grooves N, and the slit area bh (as long as imaging errors can be neglected). For m = 1, N = 10^5, λ = 500 nm and the above figures for h, b, a, f we obtain RU = 0.25 $cm^2 \cdot$sterad.

b) Interferometer. For the Michelson and Fabry-Perot interferometers, the allowable acceptance angle for photoelectric recording is limited by the aperture in front of the detector, which selects the central circular fringe. From Figs.4.54 and 63b we see that the fringe images at the center and at the edge of the limiting aperture with diameter a are produced by incoming beams which are inclined by an angle θ against each other. With $a/2 = f\theta$ the solid angle accepted by the FPI is $\Omega = \pi a^2/(4f^2)$. For a plate diameter D the étendue is $U = \pi(D^2/4)\theta^2$. According to (4.98) the spectral resolving power $R = \nu/\Delta\nu$ is correlated with the étendue U by $R = \pi D^2(2U)^{-1}$. The product RU is therefore

$$RU = \pi D^2/2 \, . \tag{4.96b}$$

For D = 5 cm, RU is about 40 cm^2 and therefore two orders of magnitude larger than for a grating spectrometer.

In Sect.4.2.10 we have seen that for a given resolving power the spherical FPI has a larger étendue for mirror separations $r > D^2/4d$. For Example 4.17 with D = 5 cm, d = 1 cm, the confocal FPI, therefore, gives the largest product RU of all interferometers for r > 6 cm. Because of the higher total finesse, however, the confocal FPI may be superior to all other instruments even for smaller, mirror separations.

In summary, we can say that interferometers have a larger light-gathering power than spectrometers at comparable resolving power. However, the need for high-quality optical surfaces for mirrors and beam splitters and the inconvenience of careful alignment represent a certain disadvantage.

4.4 Accurate Wavelength Measurements

One of the major tasks for spectroscopists is the measurement of wavelengths of spectral lines. This allows the determination of molecular energy levels and of molecular structure. The attainable accuracy of wavelength measurements depends not only on the spectral resolution of the measuring

device but also on the achievable signal-to-noise ratio and on the reproducibility of measured absolut wavelength values.

With the ultrahigh resolution which can, in principle, be achieved with single-mode tunable lasers (Chaps.6-10), the accuracy of absolute wavelength measurements attainable with conventional techniques may not be satisfactory. New methods have been developed which are mainly based on interferometric measurements of laser wavelengths. For applications in molecular spectroscopy, the laser can be stabilized on the center of a molecular transition. Measuring the wavelength of such a stabilized laser yields simultaneously the wavelength of the molecular transition with a comparable accuracy. We shall briefly discuss some of these devices, often called *wavemeters* which measure the unknown laser wavelength by comparison with a reference wavelength λ_R of a stabilized reference laser. Most proposals use for reference a HeNe laser, stabilized on a hyperfine component of a molecular iodine line, which has been measured by direct comparison with the primary wavelength standard to an accuracy of better than 10^{-9} [4.56].

Another method measures the absolute frequency ν_L of a stabilized laser and deduces the wavelength λ_L from the relation $\lambda_L = c/\nu_L$ using the *best* experimental values for the speed of light [4.57-59], which has been chosen to *define* the meter and thus the wavelength λ by the definition: 1 m is the distance travelled by light in vacuum during the time $\Delta t = 1/299792458\ s^{-1}$. This defines the *speed of light* as

$$c = 299792458 \text{ m/s} \, . \tag{4.97}$$

Such a scheme reduces the determination of lengths to the measurements of times or frequencies, which can be measured much more accurately than lengths [4.60]. This method will be discussed in Sect.14.7.

4.4.1 Precision and Accuracy of Wavelength Measurements

Resolving power and light-gathering power are not the only criteria by which a wavelength-dispersing instrument should be judged. A very important question is the attainable *precision* and *accuracy* of absolute wavelength measurements.

To measure a physical quantity always means to *compare* it with a reference standard. This comparison involves statistical and systematic errors. Measuring the same quantity n times will yield values X_i which scatter around the mean value

$$\overline{X} = \frac{1}{n}\sum_{i=1}^{n} X_i \, .$$

The attainable **precision** for such a set of measurements is determined by statistical errors and is mainly limited by the signal-to-noise ratio for a single measurement and by the number n of measurements (i.e., by the total measuring time). The precision can be characterized by the *standard deviation* [4.61,62],

$$\sigma = \left(\sum_{i=1}^{n} \frac{(\overline{X} - X_i)^2}{n} \right)^{1/2} . \qquad (4.98)$$

The adopted mean value $\overline{X}$, averaged over many measured values X_i, is claimed to have a certain *accuracy*, which is a measure of the reliability of this value, expressed by its probable deviation $\Delta\overline{X}$ from the unknown "true" value X. A stated accuracy of $\overline{X}/\Delta\overline{X}$ means a certain confidence that the true value X is within $\overline{X} \pm \Delta\overline{X}$. Since the accuracy is determined not only by statistical errors but, particularly, by systematic errors of the apparatus and measuring procedure, it is always lower than the precision. It is also influenced by the precision with which the reference standard can be measured and by the accuracy of its comparison with the value $\overline{X}$. Although the attainable accuracy depends on the experimental efforts and expenditures, the skillfulness, imagination, and critical judgement of the experimentalist always have a major influence on the finally achieved and stated accuracy.

We shall characterize precision and accuracy by the relative uncertainties of the measured quantity X, expressed by the ratios

$$\frac{\sigma}{\overline{X}} \quad \text{or} \quad \frac{\Delta\overline{X}}{\overline{X}} ,$$

respectively. A series of measurements with a standard deviation $\sigma = 10^{-8}\,\overline{X}$ has a relative uncertainty of 10^{-8}. Often one says that the precision is 10^{-8} although this statement has the disadvantage that a high precision is expressed by a small number.

Let us now briefly examine the attainable precision and accuracy of wavelength measurements with the different instruments discussed above. Although both quantities are correlated with the resolving power and the attainable signal-to-noise ratio, they are furthermore influenced by many other instrumental conditions, such as backlash of the monochromator drive, or asymmetric line profiles caused by imaging errors, or shrinking of the photographic film during the developing process. Without such additional error sources the precision could be much higher than the resolving power, because the center of a symmetric line profile can be measured to a small fraction ϵ of the halfwidth. The value of ϵ depends on the attainable signal-to-noise ratio, which is determined, apart from other factors, by the étendue of the spectrometer. We see that for the precision of wavelength measurements the product RU, discussed in the previous section, plays an important role.

For scanning monochromators with photoelectric recording the main limitation for the attainable accuracy is the backlash of the grating-drive and nonuniformities of the gears, which limit the reliability of linear extrapolation between two calibration lines. Carefully designed monochromators have errors due to the drive, which are less than 0.1 cm^{-1}, allowing an accuracy of about 10^{-5} in the visible range.

Also in absorption spectroscopy with a tunable laser the accuracy of line positions is limited by the nonuniform scan speed $d\lambda/dt$ of the laser (Sect.5.6). One has to record reference wavelength marks simultaneously with the spectrum in order to correct for the nonuniformities of $d\lambda/dt$.

A serious source of error with scanning spectrometers or scanning lasers is the distortion of the line profile and the shift of the line center caused by the time constant of the recording device. If the time constant τ is comparable with the time $\Delta t = \Delta\lambda/v_{sc}$ needed to scan through the halfwidth $\Delta\lambda$ of the line profile (which depends on the spectral resolution), the line becomes broadened, the maximum decreases, and the center wavelength is shifted. The line shift $\delta\lambda$ depends on the scanning speed v_{sc} [Å/min] and is approximately $\delta\lambda = v_{sc}\tau = (d\lambda/dt)\tau$ [4.7].

Example 4.18

With a scanning speed v_{sc} = 100 Å/min and a time constant of the recorder τ = 1 s the line shift is already $\delta\lambda$ = 1.5 Å!

Because of the additional line broadening the resolving power is reduced. If this reduction is to be less than 10%, the scanning speed must be below $v_{sc} < 0.24\Delta\lambda/\tau$. With $\Delta\lambda$ = 0.2 Å, τ = 1s → v_{sc} < 3 Å/min.

Photographic recording avoids these problems and allows therefore a more accurate wavelength determination at the expense of an inconvenient developing process of the photoplate and the following measuring procedure to determine the line positions. A typical figure for the standard deviation for a 3 m spectrograph is 0.01 cm^{-1}. Imaging errors causing curved lines, asymmetric line profiles due to misalignment, and backlash of the microdensitometer used for measuring the line positions on the photoplate are the main sources of errors.

Modern devices use photodiodes or CCD arrays (Sect.4.5.7) instead of photoplates. With a diode width of 25 μm the peak of a symmetric line profile extending over 3÷5 diodes can be determined by a least-squares-fit to a model profile within 1÷5 μm, depending on the S/N ratio. When the array is placed behind a spectrometer with a dispersion of 0.1 mm/Å, the center of the line can be determined within 10^{-2} Å. Since the signals are read electronically, there are no moving parts in the device and any mechanical error source (backlash) is eliminated.

The highest accuray (i.e., the lowest uncertainty) can be achieved with modern *wavemeters*, which we shall discuss now.

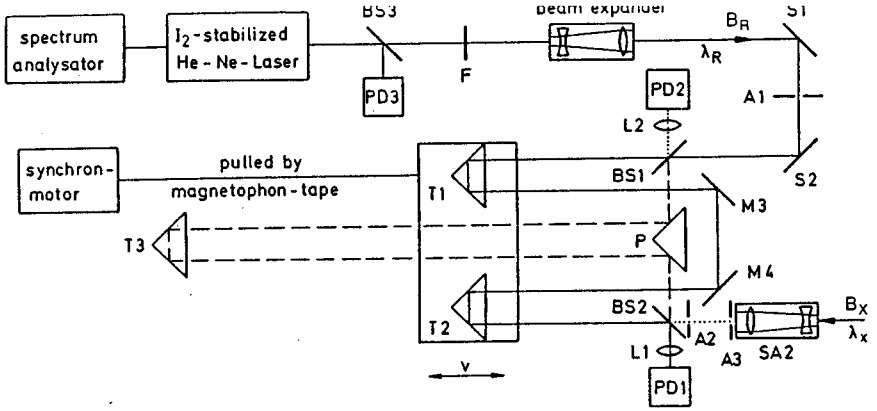

Fig.4.64. Travelling Michelson interferometer for accurate measurements of wavelengths of single-mode cw lasers

4.4.2 Today's Wavemeters

The different types of wavemeters for very accurate measurements of laser wavelengths are based on modifications of the Michelson interferometer [4.63], the Fizeau interferometer [4.64], or on a combination of several Fabry-Perot interferometers with different free spectral ranges [4.65-67]. The wavelength is measured either by monitoring the spatial distribution of the interference pattern with photodiode arrays, or by using travelling devices with electronic counting of the interference fringes.

a) The Michelson-Wavemeter

Figure 4.64 illustrates the principle of a travelling-wave Michelson-type interferometer as used in our laboratory. Such a wavemeter was first demonstrated in a slightly different version by *Hall* and *Lee* [4.63] and by *Kowalski* et al. [4.68]. The beams B_R of a reference laser and B_x of a laser with unknown wavelength λ_x traverse the interferometer on identical paths but in opposite directions. Both incoming beams are split into two partial beams by the beam splitters BS1 and BS2, respectively. One of the partial beams travels the constant path BS1-P-T3-P-BS2 for the reference beam and in the opposite direction for the beam B_X. The second partial beam travels the variable path BS1-T1-M3-M4-T2-BS2 for B_R and in the opposite direction for B_X. The moving corner-cube reflectors T1 and T2 are mounted on a carriage, which travels either with wheels on rods or slides on an airtrack.

These *corner-cube reflectors* guarantee that the incoming light beam is always reflected exactly parallel to its indicent direction, irrespective of slight misalignments or movements of the travelling reflector. The two partial beams (BS1-T1-M3-M4-T2-BS2 and BS1-P-T3-P-BS2) for the reference laser interfere at the detector PD1, and the two beams BS2-T2-M4-M3-T1-BS1 and BS2-P-T3-P-BS1 from the unknown laser interfere at the

detector PD2. When the carriage is moving at a speed $v = dx/dt$ the phase difference $\delta(t)$ between the two interfering beams changes as

$$\delta(t) = 2\pi \frac{\Delta s}{\lambda} = 2\pi \cdot 4 \frac{dx}{dt} \frac{t}{\lambda} = 8\pi \frac{vt}{\lambda}, \tag{4.99}$$

where the optical path difference Δs has been doubled by introducing two corner-cube reflectors. The rates of interference maxima, which occur for $\delta = m2\pi$, are counted by PD2 and PD1 for the unknown wavelength λ_X and the reference wavelength λ_R. From the ratio of both counting rates the unknown wavelength λ_X can be obtained if proper corrections are made for the dispersion $n(\lambda_R) - n(\lambda_X)$ of air.

The signal lines to both counters are simultaneously opened at the time t_0 when the detector PD2 just delivers a trigger signal. Both counters are simultaneously stopped at the time t_1 when PD2 has reached the preset number N_0. From

$$\Delta t = t_1 - t_0 = N_0 \lambda_X / 4v = (N_R + \epsilon)\lambda_R / 4v$$

we obtain for the vacuum wavelength λ_X^0

$$\lambda_X^0 = \frac{N_R + \epsilon}{N_0} \lambda_R^0 \frac{n(\lambda_{X,P}\, T)}{n(\lambda_{R,R}\, T)}. \tag{4.100a}$$

The unknown fractional number $\epsilon < 2$ takes into account that the trigger signals from PD1 may not exactly coincide with the start and stop times t_0 and t_1.

For a maximum optical path difference $\Delta s = 4$ m, the number of counts for $\lambda = 500$ nm is $8 \cdot 10^6$, which allows a precision of about 10^{-7}, if the counting error is not larger than 1. Provided the signal-to-noise ratio is sufficiently high, the attainable precision can, however, be enhanced by interpolations between two successive counts using a *phase-locked loop* [4.69, 70]. This is an electronic device which multiplies the frequency of the incoming signal by a factor M while always being locked to the phase of the incoming signal. Assume that the counting rate $f_R = 4v/\lambda_R$ in the reference channel is multiplied by M. Then the unknown wavelength λ_X is determined by

$$\lambda_X^0 = \frac{MN_R + \epsilon}{MN_0} \lambda_R \frac{n_X}{n_R}. \tag{4.100b}$$

For M = 100 the limitation of the accuracy by the counting error due to the unknown fractional number ϵ is reduced by a factor of 100.

Instead of the phase-locked loop a coincidence curcuit may be employed. Here the signal paths to both counters are opened at the time t_0 and closed at t_1, when both trigger signals from PD2 and PD1 coincide within a

small time intervall, say 10^{-8} s. Both techniques reduce the counting uncertainty to a value below $2 \cdot 10^{-9}$.

In general, the attainable accuracy, however, is lower because it is influenced by several sources of systematic errors. One of them is a misalignment of the interferometer, which causes both beams to travel slightly different path lengths. Another point which has to be considered is the curvature of the wavefronts in the diffraction-limited Gaussian beams (Sect.5.3). This curvature can be reduced by expanding the beams through telescopes (Fig.4.64). The uncertainty of the reference wavelength λ_R and the accuracy of measuring the refractive index $n(\lambda)$ of air are further error sources.

The maximum relative uncertainty of the absolute vacuum wavelength λ_X can be written as a sum of 5 terms:

$$\left|\frac{\Delta\lambda_X}{\lambda_X}\right| \leq \left|\frac{\Delta\lambda_R}{\lambda_R}\right| + \left|\frac{\epsilon}{MN_R}\right| + \left|\frac{\Delta r}{r}\right| + \left|\frac{\delta s}{\Delta s}\right| + \left|\frac{\delta\phi}{2\pi N_0}\right| \qquad (4.101)$$

where $r = n(\lambda_X)/n(\lambda_R)$ is the ratio of the refractive indices. Let us briefly estimate the magnitude of the different terms in (4.101):

- The wavelength λ_R of the I_2-stabilized HeNe laser is known within an uncertainty $|\Delta\lambda_R/\lambda_R| < 10^{-10}$ [4.60]. Its frequency stability is better than 100 kHz, i.e. $|\Delta\nu/\nu| < 2 \cdot 10^{-10}$. This means that the first term in (4.101) contributes at most $3 \cdot 10^{-10}$ to the uncertainty of λ_X.
- With $\epsilon = 1.5$, $M = 100$ and $N_R = 8 \cdot 10^6$ the second term is about $2 \cdot 10^{-9}$.
- The index of refraction, $n(\lambda, p, T)$, depends on the wavelength λ, on the total air pressure, on the partial pressures of H_2O and CO_2, and on the temperature. If the total pressure is measured within 0.5 mbar, the temperature T within 0.1 K and the relative humidity within 5%, the refractive index can be calculated from formulas given by *Edlen* [4.71] and *Owens* [4.72].

With the stated accuracies the 3rd term in (4.101) becomes

$$|\Delta r/r| \approx 1 \cdot 10^{-3} |n_0(\lambda_X) - n_0(\lambda_R)| \qquad (4.102)$$

where n_0 is the refractive index for dry air under standard conditions (T_0 = 15° C, p_0 = 760 torr). The contribution of the 3rd term depends on the wavelength difference $\Delta\lambda = \lambda_R - \lambda_X$. For $\Delta\lambda = 1$ nm one obtains $|\Delta r/r| < 10^{-11}$ while for $\Delta\lambda = 200$ nm this term becomes with $|\Delta r/r| \approx 5 \cdot 10^{-9}$ a serious limitation of the accuracy of $|\Delta\lambda_X/\lambda_X|$.

- The magnitude of the 4th term $|\delta s/\Delta s|$ depends on the efforts put into the alignment of the two laser beams within the interferometer. If the two beams are tilted against each other by a small angle α the two path lengths for λ_X and λ_R differ by

$$\delta s = \Delta s(\lambda_R) - \Delta s(\lambda_X) = \Delta s_R(1 - \cos\alpha) \approx (\alpha^2/2)\Delta s_R \,.$$

With $\alpha = 10^{-4}$ rad the systematic relative error becomes already

$$|\delta s/\Delta s| \approx 5 \cdot 10^{-9} \,.$$

It is, therefore, necessary to align both beams very carefully.

- With a surface quality of $\lambda/10$ for all mirrors and beam spliters the distortions of the wavefront is already visible in the interference pattern. However, plane waves are focussed onto the detector area and the phase of the detector signal is due to an average over the cross section of the enlarged beam ($\approx 1\,cm^2$). This averaging minimizes the effect of wavefront distortion on the accuracy of λ_X. If the modulation of the interference intensity (4.38) exceeds 90%, this term may be neglected.

With careful alignment, good optical quality of all optical surfaces and accurate recording of p, T, P_{H_2O} the total uncertainty of λ_X can be pushed below 10^{-8}, which means an uncertainty $\Delta\nu_x \approx 3$ MHz of the optical frequency $\nu_x = 5 \cdot 10^{14}\ s^{-1}$ for a wavelength separation of $\Delta\lambda \approx 120$ nm. This has been proved by a comparison of independently measured wavelengths $\lambda_x = 514.5$ nm (I_2-stabilized argon laser) and $\lambda_R = 632.9$ nm (I_2-stabilized HeNe laser) [4.73].

When CW dye laser wavelengths are measured, another source of error arises. Due to air bubbles in the dye jet or dust particles within the resonator beam waist the dye laser emission may be interrupted for a few microseconds. If this happens while counting the wavelength a few counts are missing. This can be avoided by using an additional phase-locked loop with a multiplication factor $M_x = 1$ in the counting channel of PD_x. If the time constant of the phase locked loop is larger than 10 μs it continues to oscillate at the counting frequency during the few μs of dye-laser beam interruptions.

There are meanwhile several different designs of Michelson wavemeters which were described in [4.74-76].

b) Sigmameter

While the travelling Michelson is restricted to CW lasers, a motionless Michelson interferometer has been designed by *Jacquinot* et.al. [4.77], which includes no moving parts and can be used for CW as well as for pulsed lasers. Figure 4.65 illustrates its operation.The basic element is a Michelson with a *fixed* path difference Δs. The laser beam enters the interferometer polarized at 45° with respect to the plane of Fig.4.65. When inserting a prism into one arm of the interferometer, where the beam is totally reflected at the prism base, a phase difference $\Delta\varphi$ is introduced between the two components polarized parallel and perpendicular to the totally reflecting surface. The value of $\Delta\varphi$ depends, according to Fresnel's formulas [4.13], on the incidence angle α and can be made $\pi/2$ for $\alpha = 55°\,19'$ and $n = 1.52$. The interference signal at the exit of the interferometer is recorded separately for the two polarizations and one obtains, because of the phase shifts $\pi/2$, $I_{\parallel} = I_0(1+\cos 2\pi\Delta s/\lambda)$ and $I_{\perp} = I_0(1+\sin 2\pi\Delta s/\lambda)$. From these sig-

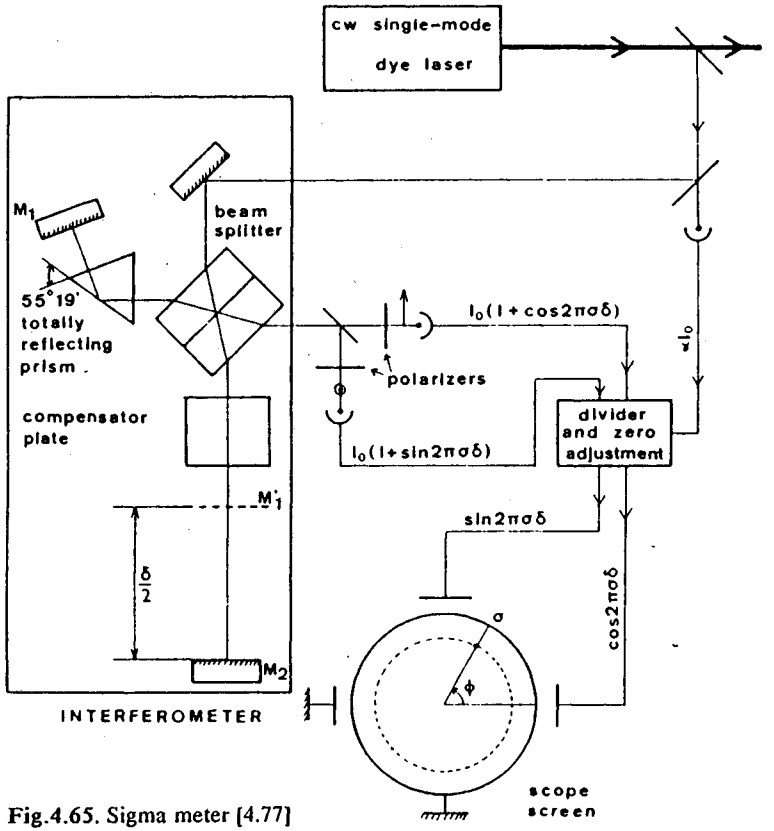

Fig.4.65. Sigma meter [4.77]

nals it is possible to deduce the wave number $\sigma = 1/\lambda$ modulo $1/\Delta s$, since all wave numbers $\sigma_m = \sigma_0 + m/\Delta s$ (m = 1,2,3...) give the same interference signals. Using several interferometers of the same type, with a common mirror M1 but different positions of M2, which have path differences in geometric ratios, such as 50 cm, 5 cm, 0.5cm, and 0.05 cm, the wave number σ can be deduced unambiguously with an accuracy determined by the interferometer with the highest path difference. The actual path differences Δs_i are calibrated with a reference line and are servo-locked to this line. The precision obtained with this instrument is about 5 MHz, which is comparable with that of the travelling Michelson interferometer. The measuring time, however, is much smaller since the different Δs_i can be determined simultaneously. It is more difficult to build but easier to handle. Since this instrument measures wave numbers, $\sigma = 1/\lambda$, the inventors called it a *sigmameter*.

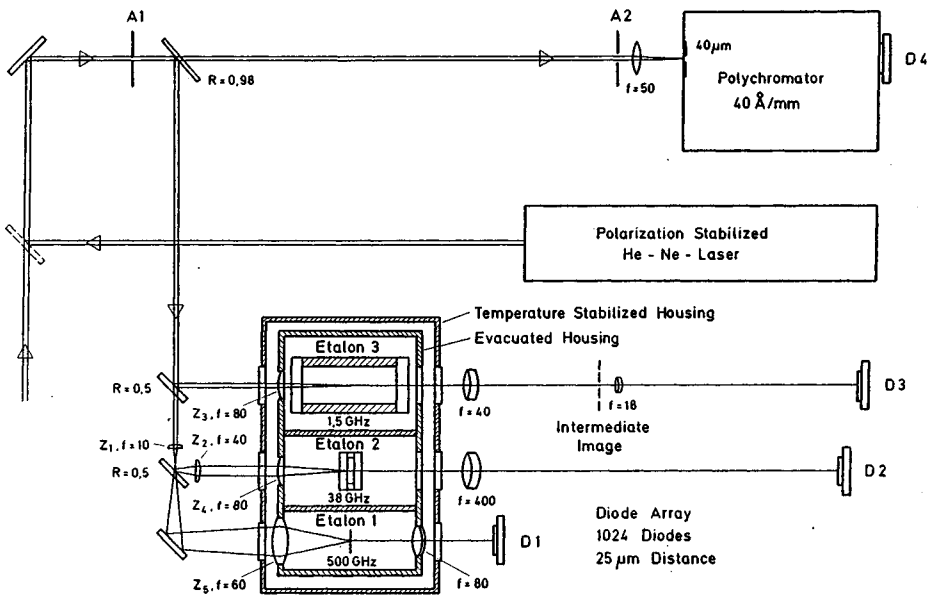

Fig.4.66. Wavemeter for pulsed and cw lasers, based on a combination of a small polychromator and three FPI with widely differing free spectral ranges [4.73]

c) Computer-Controlled Fabry-Perot Wavemeter

Another approach to accurate wavelength measurements of pulsed and CW lasers, which can be also applied to incoherent sources, relies on a combination of grating monochromator and three Fabry-Perot etalons [4.65-67]. The incoming laser beam is sent simultaneously through a small monochromator and three temperature-stabilized Fabry-Perot interferometers with different free spectral ranges $\delta\nu_i$ (Fig.4.66). In order to match the laser-beam profile to the sensitive area of the linear diode arrays (25mm×50μm), focussing with cylindrical lenses Z_i is utilized. The divergence of the beams in the plane of Fig.4.66 is optimized by the spherical lenses L_i in such a way, that the diode arrays detect 4÷6 FPI fringes (Fig.4.67). The linear arrays have to be properly aligned that they coincide with a diameter through the center of the ring system. According to (4.65b), the wavelength

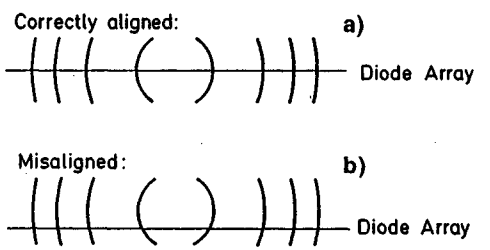

Fig.4.67a,b. Measuring interference ring diameters with a linear diode array. (a) correct alignment (b) misaligned diode array

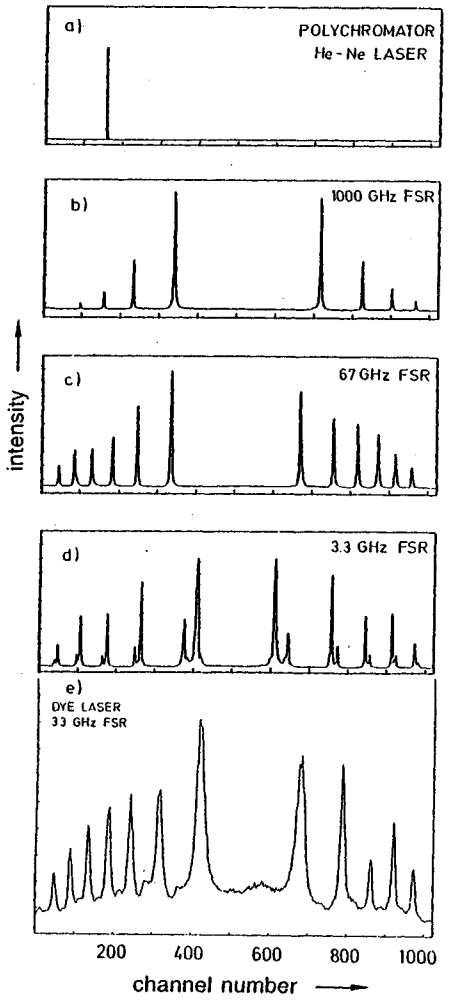

Fig.4.68. Output signals at the 4 diode arrays of the FPI wave meter, which had been illuminated by a cw He-Ne laser oscillating on two axial modes (a-d). The lowest figure shows the ring intensity pattern of an excimer pumped single mode dye laser measured behind a FPI with 3.3 GHz free spectral range

λ can be determined from the ring diameters D_p and the excess ϵ, provided the integer order m_0 is known, which means that λ must already be known, at least within one half of a free spectral range (Sect.4.3).

The device is calibrated with different lines from a CW dye laser which are simultaneously measured with the travelling Michelson wavemeter (see above). This calibration allows:

- The unambiguous attachment between wavelength λ and the position of the illuminated diode of array #1 behind the monochromator with an accuracy of ±0.1 nm.
- The accurate determination of nd for all three FPI.

If the free spectral range $\delta\nu_1$ of the thin FPI is at least twice as large as the uncertainty $\Delta\nu$ of the monochromator measurement, the integer order m_0 of FPI1 can be unambiguously determined and the measurement of the ring diameters improves the accuracy by a factor of about 20. This is sufficient to determine the larger integer order m_0 of FPI2 and from its ring diameters λ can be measured with an accuracy 20 times higher than that from FPI1. The final wavelength determination uses the ring diameters of the large FPI3. Its accuracy reaches about 1% of the free spectral range of FPI3.

The whole measuring cycle is controlled by a computer and for pulsed lasers one pulse (with an energy of $\geq 5\mu J$) is sufficient to initiate the device while for CW lasers a few μW input power are sufficient. The arrays are read out by the computer and the signals can be displayed on a screen. Such signals for the arrays D1-D4 are shown in Fig.4.68.

Since the optical distances $n_i d_i$ of the FPI depend critically on temperature and pressure all FPI must be kept in a temperature-stabilized pressure-tight box. Furthermore, a stabilized HeNe laser can be used to control long-term drift of the FPI [4.73].

Example 4.19

With a free spectral range of $\delta\nu$ = 1 GHz the uncertainty of calibration and the determination of an unknown wavelength are both about 10 MHz. This gives an absolute uncertainty of less than 20 MHz. For the optical frequency $\nu = 6 \cdot 10^{14}$ Hz the relatice accuracy is then $\Delta\nu/\nu \leq 3 \cdot 10^{-8}$.

---

d) Fizeau Wavemeter

The Fizeau wavemeter, constructed by *Snyder* [4.78] can be used for pulsed and CW lasers. While its optical design is simpler than that of the sigmameter and the FPI wavemeter, its accuracy is slightly lower. Its basic principle is shown in Fig.4.69. The incident laser beam is focussed by an achromatic microscope lens system onto a small pinhole which represents a nearly pointlike light source. The divergent light is transformed by a parabolic mirror into an enlarged parallel beam which hits the Fizeau interferometer under an incident angle α. The FI consists of two fused quartz plates with a slightly wedged air gap ($\phi \approx 1/20°$). For small wedge angles ϕ the optical path difference Δs between the interfering beams 1 and 1′ is approximately equal to that of a plane-parallel plate according to (4.47a), namely

$$\Delta s_1 = 2nd(z_1)\cos\beta = m\lambda \, .$$

The path difference between the beams 2 and 2′ is $\Delta s_2 = (m+1)\lambda$. The interference of the reflected light produces a pattern of parallel fringes with the separation

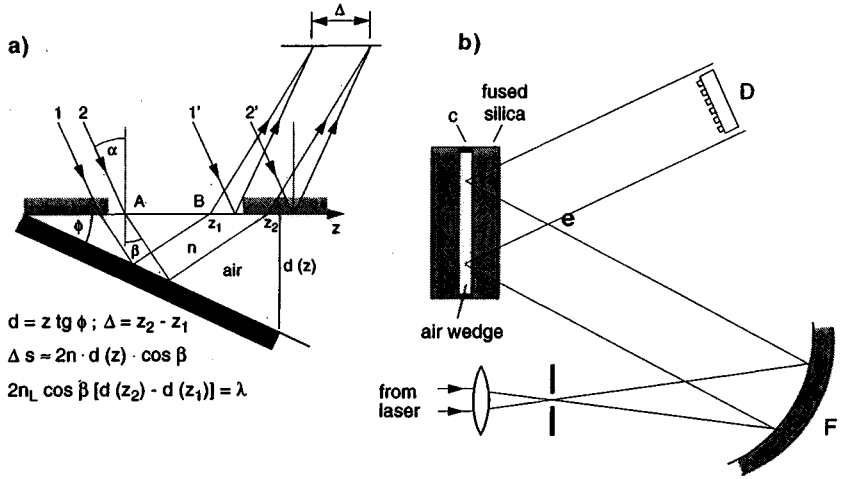

Fig.4.69a,b. Fizeau wavemeter. (a) Interference at a wedge (b) schematic design (A: aperture as spatial filter, P: parabolic mirror, C: distance holder of cerodur, D: diode array)

$$\Delta = z_2 - z_1 = \frac{d(z_2) - d(z_1)}{\tan\phi} = \frac{\lambda}{2n\tan\phi\cos\beta} \qquad (4.103)$$

which depends on the wavelength λ, the slope angle ϕ, the angle of incidence, α, and the refractive index n of air.

Changing the wavelength λ causes a shift Δz of the fringe pattern and a slight change of the fringe separation Δ. For a change of λ by one free spectral range

$$\delta\lambda = \frac{\lambda^2}{2nd\cos\beta} . \qquad (4.104)$$

Δz is equal to the fringe separation Δ, and the two fringe patterns for λ and $\lambda+\delta\lambda$ look identical, apart from the slight change of Δ. It is, therefore, essential to know λ at least within $\pm\delta\lambda/2$. This is possible from a measurement of Δ. With a diode array of 1024 diodes the fringe separation Δ can be obtained from a least-squares fit to the measured intensity distribution I(z) with a relative accuracy of 10^{-4}, which yields an absolute value of λ within $\pm 10^{-4}\lambda$ [4.79].

With a value d = 1 mm of the air gap the order of interference, m, is about 3000 at λ = 500 nm. An accuracy of 10^{-4} is therefore sufficient for the unambiguous determination of m. Since the *position* of the interference fringes can be measured within 0.3% of the fringe separation, the wavelength λ can be obtained within 0.3% of a free spectral range, which gives the accuracy $\lambda/\Delta\lambda \approx 10^7$. The preliminary value of λ, deduced from the

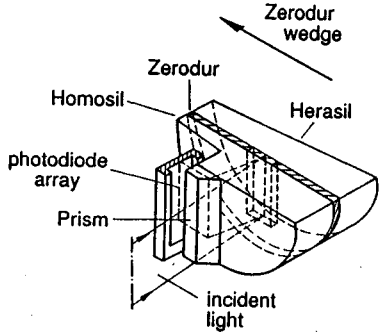

Fig.4.70. Compact design of a Fizeau wave meter [4.80]

fringe separation Δ and the final value, determined from the *fringe position*, are both obtained from the same FI, after having calibrated the system with lines of known wavelengths.

The advantage of the Fizeau Lambdameter is its compact design and its low price. A very elegant construction by *Gardner* [4.80,81] is sketched in Fig.4.70. The air gap is fixed by a Cerodur-spacer between the two interferometer plates, and forms a pressure tight volume. Variations of air pressure therefore do not cause changes of n within the air gap. The reflected light is sent to the diode array by a totally reflecting prism. The data are processed by a small computer.

4.5 Detection of Light

For many applications in spectroscopy the sensitive detection of light and the accurate measurement of its intensity are of crucial importance for the successful performance of an experiment. The selection of the proper detector for optimum *sensitivity* and *accuracy* for the detection of radiation must take into account the following characteristic properties which may differ for the various detector types:

- The spectral relative response $R(\lambda)$ of the detector, which determines the wavelength range, in which the detector can be used. The knowledge of $R(\lambda)$ is essential for the comparison of the relative intensities $I(\lambda_1)$ and $I(\lambda_2)$ at different wavelengths.
- The absolute sensitivity $S(\lambda) = V_s/P$, which is defined as the ratio of output signal V_s to incident radiation power P. If the output is a voltage, as in photovoltaic devices or in thermocouples, the sensitivity is expressed in units of volts per watt. In case of photocurrent devices, such as photomultipliers, $S(\lambda)$ is given in amperes per watt. With the detector area A the sensitivity S can be expressed in terms of the irradiance I:

$$S(\lambda) = V_s/(AI) . \qquad (4.105)$$